Leopold-Franzens-Universität Innsbruck
Fakultät für Mathematik, Informatik und Physik

Self-organization in Multi-mode Cavities

and

Dipole-dipole Interaction in Large Spin Systems

Dissertation
zur Erlangung des akademischen Grades
Doctor of Philosophy

von

Sebastian Krämer, M.Sc.

Betreut durch

Univ.-Prof. Dr. Helmut Ritsch,
Institut für Theoretische Physik

Innsbruck, Dezember 2016

Zusammenfassung

Bei der Suche nach besseren optischen Laserkühlverfahren für Vielteilchensystemen mit Hilfe einer Cavity wurde der Effekt der Selbstorganisation eher zufällig entdeckt. Die einzige Änderung zur ursprünglichen Methode war, dass die Cavity nicht direkt durch die Spiegel bestrahlt wurde, sondern indirekt über die sich in der Cavity befindenden Atome. Theoretische Simulationen im semiklassischem Limit zeigten, dass ab einer bestimmten Intensität des eingestrahlten Lichtes sich die Teilchen in einem von zwei Mustern anordnen. Entweder positionierten sie sich an jedem geradzahligen Intensitätsmaximum der Cavity-Mode oder an jedem ungeradzahligen.

Anschaulich lässt sich dies folgendermaßen erklären. Nachdem die Teilchen in diesem Modell von Licht angezogen werden, ist es zu erwarten, dass sie sich vor allem in der Nähe der Intensitätsmaxima aufhalten werden. Zusätzlich muss man berücksichtigen, dass Atome, die sich in angrenzenden Maxima befinden, Licht mit einem Phasenunterschied von π, also destruktiv, in die Cavity strahlen und somit in Summe keine Photonen in die Cavity gelangen.

Unvermeidbar werden von Zeit zu Zeit mehr Teilchen in entweder den geradzahligen oder in den ungeradzahligen Maxima sein. Durch die damit verbundenen korrelierten Fluktuationen im Cavity Lichtfeld entsteht ein optisches Potenzial, das dieses Ungleichgewicht weiter verstärkt. Bei genügend starker Einstrahlung entsteht eine positive Rückkopplung, welche dazu führt, dass alle Teilchen sich für eine der beiden Möglichkeiten entscheiden.

Durch Hinzufügen weiterer Laser mit unterschiedlichen Frequenzen kann dieses Modell von transversal gepumpten Atomen leicht verallgemeinert werden. Die Frequenz jedes Lasers ist dabei auf eine unterschiedliche Mode der Cavity gestimmt. Jeder einzelne dieser Laser würde für sich alleine zwei verschiedene Anordnungen erlauben, die aber im Allgemeinen nicht kompatibel mit den Mustern der anderen Laser sind. Es stellt sich daher die Frage, wie sich die Atome in diesem Fall organisieren und ob es mehrere unterschiedliche Möglichkeiten gibt. Im ersten Teil dieser Arbeit beschäftige ich mich genau mit dieser Fragestellung. Zuerst erarbeite ich eine Mastergleichung, die dieses System beschreibt, und untersuche numerisch seine Zeitentwicklung. Abschließend präsentiere ich noch zwei Methoden um solche Steady-State Muster näherungsweise zu bestimmen.

Der zweiten Teil dieser Arbeit untersucht den Einfluss der Dipol-Dipol Wechselwirkung und des kollektiven Zerfalls auf Systeme bestehend aus räumlich verteilten Spins. Das anschauliche Bild dazu ist, dass Photonen, die von einem Atom emittiert werden, andere, sich in der Nähe befindliche Atome, beeinflussen und somit ihre Energieniveaus verschiebt und die Zerfallsraten ändert. Eine Kumulantenentwicklung liefert die nötige Basis um Systeme mit größeren Teilchenzahlen numerisch zu untersuchen.

Als erstes Beispiel untersuchen wir einen superradianten Laser. Als Modell kann das übliche Lasermodell verwendet werden, bei dem N Teilchen an eine Mode einer Cavity gekoppelt werden. Der einzige Unterschied ist, dass diese Atome räumlich getrennt sind und wechselwirken. Es zeigt sich, dass abhängig von der genauen Anordnung, die Linienbreite und weitere Laserparameter signifikant verändert werden.

Ein ähnlicher Effekt tritt bei den derzeitig besten Atomuhren, den optical-lattice-clocks, auf. Der Grundstein dieser Uhren ist ein optisches Gitter, in dem ultrakalte Atome gefangen sind. Die Struktur des optischen Gitters wird durch die Anordnung der Laser bestimmt. Es zeigt sich, dass dies die Uhrenfrequenz und auch die Zerfallsrate der Atome wesentlich verändern kann. Überraschenderweise kann dies auch zu einer Verbesserung der Genauigkeit führen. Aus diesem Grund habe ich verschiedenste Geometrien auf ihr Verhalten untersucht.

Eine weiterer, schon länger bekannter Ansatz die Uhrengenaugkeit zu verbessern ist die Atome durch squeezing untereinander zu verschränken. Daher habe ich die Kumulantenentwicklung noch erweitert, um squeezing zu ermöglichen. Damit kann in Zukunft analysiert werden, ob die Verwendung beider Verfahren gemeinsam zu weiteren Verbesserungen führt.

Der letzte Teil dieser Arbeit beschäftigt sich mit den numerischen Programmen die im Rahmen dieser Dissertation erstellt wurden.

Abstract

The effect of self-organization was originally encountered while trying to improve the effectiveness of optical cooling schemes for many-particle systems by illuminating the atoms transversally instead of pumping the cavity directly. Studying the system in a semi-classical limit showed the existence of a finite critical pump strength above which the atoms start to organize in regular patterns at every second anti-node of the pumped cavity mode.

Intuitively, this can be explained by the following observations. First of all, the particles in this model are assumed to be high-field seekers and we therefore expect them to be focused around the anti-nodes of the cavity mode. The second observation is that particles that are positioned at neighboring anti-nodes scatter light from the pump laser into the cavity with a phase shift of π, which means that the light interferes destructively, leaving the cavity mode unoccupied. Fluctuations of the particle distribution between even and odd anti-nodes leads to correlated fluctuations in the electric field of the cavity, which in turn creates an optical potential that favors either the even or the odd anti-nodes – whichever are accidentally more occupied at the moment. If the pumping is strong enough, this effect leads to a positive feedback and results in a complete ordering at the even or the odd anti-nodes.

A straight-forward extension of this model of transversally pumped atoms in a cavity is to add additional pump lasers tuned to distinct cavity modes. Each laser alone gives rise to two different possible orderings, which in general are incompatible with the patterns generated by the other lasers. The question arises what are the possible steady state patterns that the system can reach. In the first part of this theses, I derive the master equation of this system and numerically study its time evolution. Further on I present two methods to find its steady state solutions.

The second part of this thesis focuses on the influence of the dipole-dipole interaction and collective decay onto the spin dynamics in spatially well arranged many-particle systems. Intuitively, this can be pictured as photons emitted from one atom affecting other nearby atoms, thereby shifting their energy levels and changing their decay behavior. Performing a cumulant expansion provides a theoretical framework well suited to perform numerically simulations of such models by neglecting higher order correlations.

One example, suitable for this approach, is the superradiant laser. It can be modeled similarly to the traditional laser as N-particles inside of a cavity, but where the particles are spatially distributed. Depending on the specific arrangement, the line-width and other laser parameters can be significantly altered. Similar effects occur in the latest generation of atomic clocks, i.e. optical lattice clocks. The choice of lattice, generated by the trapping beams, modifies the clock frequency and also the decay rate of the trapped atoms. Although one would probably expect that this generally reduces the clocks accuracy, it turns out that for certain setups it can actually lead to improvements. Therefore, I investigated optimized geometries for future generation optical lattice clocks.

An alternative approach to improve the accuracy of atomic lattice clocks is to use squeezing. I expanded the cumulant expansion formalism to include squeezing which in the future can be used to study setups where both approaches are combined.

In the last part I present the numerical frameworks that were developed in the scope of this thesis.

Danksagung

Dieses Werk, das Resultat jahrelanger Arbeit, ist natürlich nicht ohne jeglicher Hilfe entstanden. Bei jedem einzelnen Schritt wurde ich unterstützt und ermutigt. Der größte Dank gehört meinem Betreuer Prof. Helmut Ritsch, welcher nicht nur für die wissenschaftliche Fahrtrichtung verantwortlich war. Durch sein Vorbild schuf er ein freundliches und positives Umfeld, welches zu enger Zusammenarbeit zwischen aller Mitglieder führte und in dem ich mich gleich dazugehörig fühlte.

An dieser Stelle möchte ich mich bei allen Kollegen bedanken. Sie standen immer für wertvolle Diskussionen zu Verfügung und wurden darüber hinaus zu Freunden. In meinen Anfangszeiten wurde ich warmherzig von meinen ersten Bürokollegen Wolfgang Niedenzu, Matthias Sonnleitner und Tobias Grießer aufgenommen und in alle notwendigen Fertigkeiten, vor allem die richtige Zubereitung von Kaffee, eingeführt. Im Laufe der Zeit wandelte sich die Gruppe und sie wurden würdevoll ersetzt durch Stefan Ostermann, Thomas Maier, Dominik Winterauer, Valentin Torggler und Daniela Holzmann, welche alte Traditionen am Leben erhielten und neue erschufen. Auch wenn die meiste Zeit mit den direkten Bürokollegen verbracht wurde, so standen die weiteren Kollegen um nichts nach. Raimar Sandner war immer bereit programmiertechnischen Fragestellungen zu diskutieren, David Plankensteiner wurde ein kritischer Benutzer meiner Libraries und Laurin Ostermann war ein treuer Begleiter bei Konferenzen und eine große Hilfe bei vieler meiner Publikationen.

Die Eckpfeiler, nicht nur während meines Studiums, sondern meines ganzen Lebens, sind unbestreitbar die Mitglieder meiner Familie. Ich möchte ich mich bei meinen Eltern und meinen beiden Schwestern bedanken, welche mich ununterbrochen anfeuern und vorantreiben und bei meinen Großeltern, die immer stolz auf mich sind.

Contents

Part I.

Transversally pumped multi-mode cavities

1. Introduction

Incredible advances in cooling techniques not only lead to the successful creation of Bose-Einstein condensates but opened the path to many new, exciting applications. Among others, systems consisting of atoms inside of a high finesse cavity gained new interest. The ultra-low temperatures of the particles facilitated long interaction times and even made real time observation of single atom effects possible. In one such experiment, cold atoms were dropped slowly through a cavity [1]. Using the transmission spectrum allowed precise measurement of the atomic motion. Although the cavity was only used as tool to probe the atoms, it was shown that the back-action of the cavity field onto the atoms lead to significant acceleration of the atoms along the cavity axis [2]. Interestingly, it turned out that with the correct choice of parameters, i.e. red detuning of the probing laser with regard to the atomic transition, a similar setup can also be used to cool the atoms far below the Doppler limit [3]. The motional energy of the atoms is in this case first transfered into the cavity field and then dissipates through the cavity mirrors. Like most ensemble based cooling schemes also this one, where all atoms couple together to a single light mode, scales unfavorably with the number of particles. However, slightly modifying the system by directly illuminating the atoms transversally to the cavity axis instead of longitudinally through the cavity leads to different behavior. For a single atom this alteration results only in quantitative adjustments [4]. By contrast, for atomic ensembles it introduces a completely new phenomenon, named self-organization, which leads to a radically changed scaling behavior [5]. Self-organization itself became an interesting research topic exhibiting interesting effects like e.g. phase transitions [6].

In the following, a short summary of this transversally pumped cavity model is given. Afterwards, the effect of self-organization is schematically explained. Then the extension of this system to include multiple cavity modes of distinct frequencies, as was developed in the publication [7], is presented. Finally, different approximations are used with varying success to search for interesting steady state solutions of this system.

References

1. Mabuchi, H., Turchette, Q. A., Chapman, M. S. & Kimble, H. J. Real-time detection of individual atoms falling through a high-finesse optical cavity. *Optics Letters* **21,** 1393. ISSN: 0146-9592 (1996).

2. Doherty, A. C., Parkins, A. S., Tan, S. M. & Walls, D. F. Motion of a two-level atom in an optical cavity. *Physical Review A* **56,** 833–844. ISSN: 1050-2947 (1997).
3. Horak, P., Hechenblaikner, G., Gheri, K. M., Stecher, H. & Ritsch, H. Cavity-Induced Atom Cooling in the Strong Coupling Regime. *Physical Review Letters* **79,** 4974–4977. ISSN: 0031-9007 (1997).
4. Domokos, P., Salzburger, T. & Ritsch, H. Dissipative motion of an atom with transverse coherent driving in a cavity with many degenerate modes. *Physical Review A* **66,** 043406. ISSN: 1050-2947 (2002).
5. Domokos, P. & Ritsch, H. Collective Cooling and Self-Organization of Atoms in a Cavity. *Physical Review Letters* **89,** 253003. ISSN: 0031-9007 (2002).
6. Baumann, K., Guerlin, C., Brennecke, F. & Esslinger, T. Dicke quantum phase transition with a superfluid gas in an optical cavity. *Nature* **464,** 1301–6. ISSN: 1476-4687 (2010).
7. Krämer, S. & Ritsch, H. Self-ordering dynamics of ultracold atoms in multicolored cavity fields. *Physical Review A* **90,** 033833. ISSN: 1050-2947 (2014).

1.1. Single-mode cavity

As depicted in Fig. 1.1, N polarizable particles of mass m are positioned inside a planar cavity, which is essentially reduced to one single relevant mode of frequency ω_c. They are pumped coherently with a laser and interact with the light field generated by the laser as well as by the cavity only via dipole interaction. This model can be treated in different formalisms ranging from mostly classical to fully quantum mechanical.

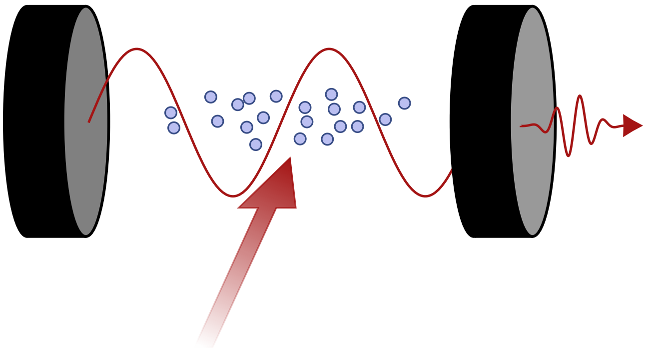

Figure 1.1.: Particles trapped inside of a planar cavity are illuminated transversally and scatter light into the cavity.

1.1.1. Quantum mechanical model

Quantum mechanically this system is, due to the photon losses through the cavity mirrors, an open system and therefore can be described by a master equation

$$\dot{\rho} = -\frac{i}{\hbar}\left[H, \rho\right] + \kappa\left(2a\rho a^\dagger - \rho a^\dagger a - a^\dagger a \rho\right) \tag{1.1.1}$$

with the photon loss rate κ [1]. The Hamiltonian consists of the usual particle and cavity parts,

$$H_{\text{particles}} = \sum_i \frac{\hat{p}_i^2}{2m} \tag{1.1.2}$$

$$H_{\text{cavity}} = \omega_c \hat{a}^\dagger \hat{a}, \tag{1.1.3}$$

as well as the interaction Hamiltonian

$$H_{\text{int}} = -\sum_i \hat{\vec{d}}_i . \hat{\vec{E}}(\hat{x}_i). \tag{1.1.4}$$

Switching into the interaction picture and using the rotating wave approximation results in

$$H = -\Delta_c \hat{a}^\dagger \hat{a} + \sum_i \frac{p_i^2}{2m} + \sum_i U_0 \sin^2(k\hat{x}_i)\hat{a}^\dagger \hat{a} + \sum_i \eta \sin(k\hat{x}_i)(\hat{a}^\dagger + \hat{a}). \tag{1.1.5}$$

1.1.2. Semi-classical equations

Starting from the complete quantum description one can derive a much more intuitive semi-classical model [2]. First the master equation is transformed into a partial differential equation for the Wigner function. Taking the semi-classical limit, i.e. truncating terms containing derivatives higher than second order leads to a Fokker-Planck equation. This equation can then be solved using the stochastic differential equations

$$\dot{x}_j = v_j \tag{1.1.6a}$$

$$\dot{v}_j = -\frac{1}{m}\frac{\partial U(x_j, \alpha)}{\partial x_j} \tag{1.1.6b}$$

$$\dot{\alpha} = (i\Delta_c - iU_0 \sum_j \sin^2(kx_j) - \kappa)\alpha - i\eta \sum_j \sin(kx_j) + \sqrt{\frac{\kappa}{2}}\xi \tag{1.1.6c}$$

with optical potential

$$U(x, \alpha) = \hbar U_0 |\alpha|^2 \sin^2(kx) + \hbar\eta(\alpha + \alpha^*)\sin(kx). \tag{1.1.6d}$$

1.1.3. Self-organization

The mechanism of self-organization [3] is explained schematically in Fig. 1.2. Two

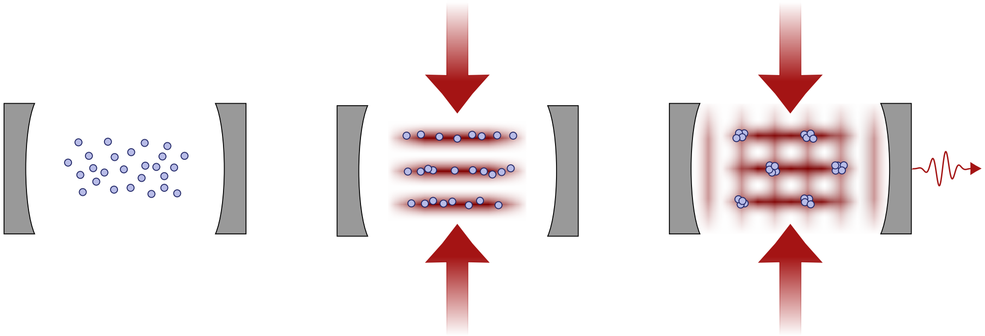

Figure 1.2.: (1) Atoms are trapped inside of a high finesse cavity. (2) Two opposed laser beams generate a standing wave orthogonal to the cavity axis. (3) Atoms self-organize in a checkerboard pattern so that scattering of photons into the cavity is maximized.

opposed laser beams generate a standing wave orthogonal to the cavity axis. Since they are red detuned compared to the relevant atomic transition, they pull the atoms towards the points of high intensity, effectively trapping them in circular disks separated by half the wave length. Assuming the atoms are distributed equally along the cavity axis, scattering of laser light into the cavity is strongly suppressed. The reason is that atoms separated by half a wavelength scatter light with a relative phase shift π, effectively canceling each other out. However, if the laser intensity is adequately high, even small fluctuations in the particle distribution disturb this equilibrium, leading to scattering of photons into the cavity after all. These photons create an additional optical potential for the atoms along the cavity axis, thereby driving the particles further away from their initial equal distribution. Again they are trapped in points of high light intensity, but in this case only every second such point is occupied. This results in the typical checker board pattern where the scattered light interferes constructively. In principle, there are two possible, equally likely configurations where either all particles are on the even sites or on the odd sites. Which one of them is adopted by the system depends on the initial disturbance of the particle distribution.

References

1. Domokos, P., Salzburger, T. & Ritsch, H. Dissipative motion of an atom with transverse coherent driving in a cavity with many degenerate modes. *Physical Review A* **66,** 043406. ISSN: 1050-2947 (2002).
2. Niedenzu, W., Grießer, T. & Ritsch, H. Kinetic theory of cavity cooling and self-organisation of a cold gas. *EPL (Europhysics Letters)* **96,** 43001. ISSN: 0295-5075 (2011).
3. Domokos, P. & Ritsch, H. Collective Cooling and Self-Organization of Atoms in a Cavity. *Physical Review Letters* **89,** 253003. ISSN: 0031-9007 (2002).

1.2. Multi-mode cavity

A straight forward extension of the model introduced in the last section is to use several pumping lasers of different frequency instead of just one as is shown in Fig. 1.2. This greatly increases the complexity of the system but also makes it much more interesting since it can be used to simulate a wider variety of Hamiltonians and possibly obtain much richer dynamics. First, we will derive a full quantum description of the system which, however, is numerically tractable only for one or two cavity modes and one or two particles. Afterwards, the corresponding semi-classical equations are stated.

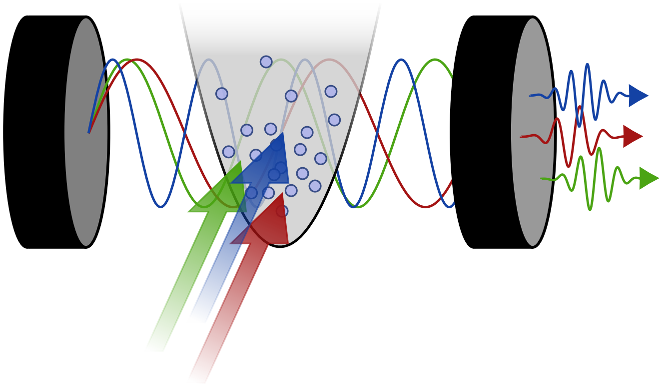

Figure 1.3.: Particles trapped inside of a planar cavity illuminated transversally by several differently colored lasers.

1.2.1. Quantum mechanical model

N ultra-cold particles are trapped in a potential $V(x)$ and placed inside of a planar cavity. The particles are polarizable but besides that have no further specified internal structure. Illuminating these particles from the side by standing waves generated by lasers of different frequencies ω_p^k and pump strength η^k scatters photons into the cavity. Each of these lasers is closely tuned to a distinct cavity mode ω_c^n. Compactly written, the system is fully determined by the following parameters:

- Modes: ω_c^n, $\hat{a}_n$, κ_n
- Particles: m, $\hat{x}_i$
- Trapping potential: $V(x)$
- Pump Laser: ω_p^k, η_k

Since due to the loss of photons through the cavity mirrors the system is an open system, the time evolution is governed by a master equation

$$\dot{\rho} = -\frac{i}{\hbar}\big[H, \rho\big] + \sum_n \kappa_n \big(2a_n \rho a_n^\dagger - \rho a_n^\dagger a_n - a_n^\dagger a_n \rho\big). \tag{1.2.1}$$

Similar to the single mode case the Hamiltonian can be split into a particle part, a cavity part and a particle-cavity interaction part,

$$H = H_{\text{cavity}} + H_{\text{particles}} + H_{\text{int}}. \tag{1.2.2}$$

Particles

The ultra-cold particles are assumed to be non-interacting and identical and are trapped in an at this point unspecified potential $V(\hat{x}_i)$ described by the Hamiltonian

$$H_{\text{particles}} = \sum_i h^i_{\text{particle}} \tag{1.2.3}$$

with the single particle Hamiltonian

$$h^i_{\text{particle}} = \frac{\hat{p}_i^2}{2m} + V(\hat{x}_i). \tag{1.2.4}$$

Cavity

As usual in quantum optics [1, 2] the cavity, where the mirrors are positioned at $-L$ and L, is described by quantized field modes with mode functions

$$\vec{u}_n(x) = \vec{e}_z \sin(k_n(x + L)), \tag{1.2.5}$$

and wave numbers

$$k_n = \frac{\pi}{2L} n \equiv kn, \tag{1.2.6}$$

which results in the Hamiltonian

$$H_{\text{cavity}} = \sum_n \omega_c^n \hat{a}_n^\dagger \hat{a}_n. \tag{1.2.7}$$

The photon losses through the cavity mirrors are taken into account by the jump operators

$$J_n = \sqrt{\kappa_n} \hat{a}_n. \tag{1.2.8}$$

Pumping lasers

The particle pump is modeled as standing wave orthogonal to the cavity axis which can, for example, be generated by shining in a laser from one side and reflecting it from a mirror positioned on the opposite side. Assuming the laser intensity is constant for the extension of the trapped particles, which can be achieved by confining the particles tightly in respect to the laser direction and using an appropriate focus, the laser light only has a time dependency left. Usually only a small part of the light is scattered into the cavity and the pump strength has to be chosen comparatively strong, it is natural to describe the laser field as classical light that itself is not influenced by the presence of the particles, i.e. the electric field at the position of the particles is

$$E_{\text{pump}} = E_0 \cos(\omega_p t). \tag{1.2.9}$$

Each laser is tuned closely to a distinct cavity mode with detuning

$$\Delta_c^n = \omega_p^n - \omega_c^n \tag{1.2.10}$$

which is assumed to be much smaller than the frequency spacing between the cavity modes.

Particle-Field Interaction

The particles are coupled separately to the light field via dipole interaction. This is described with the interaction Hamiltonian

$$H_{\text{int}} = \sum_i h_{\text{int}}^i \tag{1.2.11}$$

where the single particle-field interaction Hamiltonian is

$$h_{\text{int}}^i = -\hat{\vec{d}}.\hat{\vec{E}}(\hat{x}_i). \tag{1.2.12}$$

Since the dipole moment of the particles is induced by the electric field, where here only a linear dependency $d = \alpha E$ is assumed, this Hamiltonian,

$$h_{\text{int}}^i = -\alpha\hat{\vec{E}}(\hat{x}_i).\hat{\vec{E}}(\hat{x}_i), \tag{1.2.13}$$

is non-linear. Combining the electric field originating from the light trapped in the cavity modes,

$$\hat{\vec{E}}_{\text{cavity}}(\hat{x}_i) = \vec{e}_z \sum_n \sqrt{\frac{\hbar\omega_n}{2L\epsilon_0}} u_n(\hat{x}_i)\hat{a}_n + h.c., \tag{1.2.14}$$

and the standing waves generated by the pumping lasers,

$$\vec{E}_{\text{pump}} = \vec{e}_z \sum_n E_0^n \cos(\omega_p^n t), \tag{1.2.15}$$

results in a total electric field

$$\hat{\vec{E}} = \hat{\vec{E}}_{\text{cavity}}(\hat{x}_i) + \vec{E}_{\text{pump}}. \tag{1.2.16}$$

In principle, it seems necessary to take all different possible polarizations into account. However, in the end only one case leads to non-trivial behavior. The polarization of the cavity modes, the pumping lasers, as well as the particle dipoles have to be oriented orthogonal to both the cavity axis and the pump direction. Squaring this expression which is necessary to obtain the interaction Hamiltonian leads to three terms,

$$\hat{\vec{E}}^2 = \hat{\vec{E}}_{\text{cavity}}(\hat{x}_i).\hat{\vec{E}}_{\text{cavity}}(\hat{x}_i) + \hat{\vec{E}}_{\text{cavity}}(\hat{x}_i).\vec{E}_{\text{pump}} + \vec{E}_{\text{pump}}.\vec{E}_{\text{pump}}. \tag{1.2.17}$$

in which the last one is completely classical and therefore can be ignored for the time-evolution of the system. Remaining are the linear term,

$$\hat{\vec{E}}_{\text{cavity}}(\hat{x}_i).\vec{E}_{\text{pump}} \approx \sum_n \sin(k_n(x_i + L)) \cos(\omega_p^n t) \hat{a}_n, \tag{1.2.18}$$

and the quadratic term

$$\begin{aligned} \hat{\vec{E}}_{\text{cavity}}(\hat{x}_i).\vec{E}_{\text{pump}} \approx \sum_{nm} & \sin(k_n(x_i + L)) \sin(k_m(x_i + L)) \cos(\omega_p^m t) \cos(\omega_p^n t) \\ & \Big(\hat{a}_n \hat{a}_m + \hat{a}_n^\dagger \hat{a}_m + \hat{a}_n \hat{a}_m^\dagger + \hat{a}_n^\dagger \hat{a}_m^\dagger\Big), \end{aligned} \tag{1.2.19}$$

Total Hamiltonian

Finally, bringing it all together the total Hamiltonian reads

$$\begin{aligned} H &= H_{\text{cavity}} + H_{\text{particles}} + H_{\text{int}} \\ &= \sum_n \omega_c^n \hat{a}_n^\dagger \hat{a}_n + \sum_i \Big(\frac{\hat{p}_i^2}{2m} + V(\hat{x}_i)\Big) - \sum_i \alpha \hat{\vec{E}}(\hat{x}_i).\hat{\vec{E}}(\hat{x}_i) \end{aligned} \tag{1.2.20}$$

In order to eliminate the explicit time dependence in the electric field term we change into the interaction picture with respect to the operator $\sum_n \omega_p^n \hat{a}_n^\dagger \hat{a}$. Extensive use of the rotating wave approximation allows us to neglect all terms containing frequencies of different cavity modes as well as the usual fast rotating 2ω terms resulting in

$$\begin{aligned} H = &- \sum_n \Delta_c^n \hat{a}_n^\dagger \hat{a}_n + \sum_i (\frac{p_i^2}{2m} + V(\hat{x}_i)) \\ &+ \sum_{ni} U_0^n \sin^2(k_n(\hat{x}_i - L)) \hat{a}_n^\dagger \hat{a}_n + \sum_{ni} \eta_n \sin(k_n(\hat{x}_i - L))(\hat{a}_n^\dagger + \hat{a}_n) \end{aligned} \tag{1.2.21}$$

Hamiltonian in second quantization

For higher particle numbers it is advantageous to analyze the system in second quantization formalism. Using the eigenfunctions of a single particle plus trap,

$$h_{\text{particle}}\Psi_k(x) = E_k\Psi_k(x), \tag{1.2.22}$$

to define the field operators

$$\hat{\Psi}(x) = \sum_k \Psi_k(x)\hat{c}_k \tag{1.2.23}$$

with particle annihilation operators $\hat{c}_k$ results in

$$\begin{aligned} H = &-\sum_n \Delta_c^n \hat{a}_n^\dagger \hat{a}_n + \int dx \hat{\Psi}^\dagger(x)(\frac{-\Delta}{2m} + V(x))\hat{\Psi}(x) \\ &+ \int dx \hat{\Psi}^\dagger(x) \sum_n U_0^n \sin^2(k_n(x+L))\hat{a}_n^\dagger \hat{a}_n \hat{\Psi}(x) \\ &+ \int dx \hat{\Psi}^\dagger(x) \sum_n \eta_n \sin(k_n(x+L))(\hat{a}_n^\dagger + \hat{a}_n)\hat{\Psi}(x) \end{aligned} \tag{1.2.24}$$

which simplifies to

$$H = -\sum_n \Delta_c^n \hat{a}_n^\dagger \hat{a}_n + \sum_k E_k \hat{c}_k^\dagger \hat{c}_k + \sum_{nij} U_0^n A_{nij} \hat{c}_i^\dagger \hat{c}_j \hat{a}_n^\dagger \hat{a}_n + \sum_{nij} \eta_n B_{nij} \hat{c}_i^\dagger \hat{c}_j (\hat{a}_n^\dagger + \hat{a}_n). \tag{1.2.25}$$

The coupling strength between the various particle modes via the cavity is captured in the constants A_{nij} and B_{nij} which only depend on the geometry of the cavity as well as the geometry of the trapping potential. Mathematically, they can be calculated by evaluating the overlap integrals

$$A_{nij} = \int_{-\infty}^{\infty} \Psi_i^*(x)\Psi_j(x)\sin^2(k_n(x+L))dx \tag{1.2.26a}$$

$$B_{nij} = \int_{-\infty}^{\infty} \Psi_i^*(x)\Psi_j(x)\sin(k_n(x+L))dx. \tag{1.2.26b}$$

Changing the selection of used mode functions as well as varying the trapping potential allows to implement a wide variety of interactions that might lead to completely different dynamics. As simplest example, we apply this formalism to the case where the particles are trapped in a box potential,

$$V(x) = \begin{cases} 0 & x \in [-a,a] \\ \infty & else. \end{cases} \tag{1.2.27}$$

Therefore, the eigenfunctions of the particle-plus-trap Hamiltonian are

$$\Psi_i(x) = \begin{cases} \frac{1}{\sqrt{a}}\sin(K_i(x+a)) & x \in [-a,a] \\ 0 & else \end{cases} \tag{1.2.28}$$

with wave numbers $K_i = \frac{\pi}{2a} i \equiv Ki$ and energies $E_i = \frac{\hbar^2}{2m}\left(\frac{\pi i}{2a}\right)^2 = \frac{\hbar^2}{2m} K_i^2$. The overlap integrals

$$A_{nij} = \frac{1}{a}\int_{-a}^{a} \sin(Ki(x+a))\sin(Kj(x+a))\sin^2(kn(x+L))dx \tag{1.2.29a}$$

$$B_{nij} = \frac{1}{a}\int_{-a}^{a} \sin(Ki(x+a))\sin(Kj(x+a))\sin(kn(x+L))dx \tag{1.2.29b}$$

simplify to

$$\begin{aligned} A_{nij} = \frac{1}{2}\delta_{ij} + \frac{(-1)^n}{4}\{ &- \mathrm{sinc}(\frac{\pi}{2}(i-j+2\frac{a}{L}n))\cos(\frac{\pi}{2}(i-j)) \\ &- \mathrm{sinc}(\frac{\pi}{2}(i-j-2\frac{a}{L}n))\cos(\frac{\pi}{2}(i-j)) \\ &+ \mathrm{sinc}(\frac{\pi}{2}(i+j+2\frac{a}{L}n))\cos(\frac{\pi}{2}(i+j)) \\ &+ \mathrm{sinc}(\frac{\pi}{2}(i+j-2\frac{a}{L}n))\cos(\frac{\pi}{2}(i+j))\} \end{aligned} \tag{1.2.30a}$$

and

$$\begin{aligned} B_{nij} = \frac{1}{2}\{ &- \mathrm{sinc}(\frac{\pi}{2}(i+j+\frac{a}{L}n))\sin(\frac{\pi}{2}(i+j+n)) \\ &+ \mathrm{sinc}(\frac{\pi}{2}(-i+j+\frac{a}{L}n))\sin(\frac{\pi}{2}(-i+j+n)) \\ &+ \mathrm{sinc}(\frac{\pi}{2}(i-j+\frac{a}{L}n))\sin(\frac{\pi}{2}(i-j+n)) \\ &+ \mathrm{sinc}(\frac{\pi}{2}(i+j-\frac{a}{L}n))\sin(\frac{\pi}{2}(i+j-n))\} \end{aligned} \tag{1.2.30b}$$

Heisenberg equations

Another often useful description, especially as starting point to obtain simplified approximative expressions is the Heisenberg formalism. As important examples the equations of motion for the cavity mode annihilation operator $\hat{a}_n$ and the particle mode operator $\hat{c}_k$ are

$$\dot{a}_n(t) = \mathrm{i}(\Delta_c^n - \sum_{ij} U_0^n A_{nij} c_i^\dagger c_j) a_n(t) - \mathrm{i}\sum_{i,j} B_{nij} c_i^\dagger c_j \eta_n - \frac{\gamma_n}{2} a_n(t) - \sqrt{\gamma_n}(b_{\mathrm{in}})_n(t) \tag{1.2.31a}$$

and

$$\dot{c}_k(t) = -\mathrm{i}(E_k c_k(t) + \sum_{nj} U_0^n A_{nkj} c_j(t) a_n^\dagger a_n + \sum_{nj} B_{nkj} c_j(t)(\eta_n a_n^\dagger + \eta_n^* a_n)), \tag{1.2.31b}$$

respectively.

1.2.2. Semi-classical equations

To get a grasp of this fully quantum mechanical system it makes sense to first analyze the easier understandable classical case. The semi-classical equations from the single-mode case can easily be extended to the multi-mode case, i.e.

$$\dot{x}_j = v_j \tag{1.2.32a}$$

$$\dot{v}_j = -\frac{1}{m}\sum_n \frac{\partial U_n(x_j, \alpha_n)}{\partial x_j} \tag{1.2.32b}$$

$$\dot{\alpha}_n = (i\Delta_c^n - iU_0^n \sum_j \sin^2(k_n x_j) - \kappa_n)\alpha_n - i\eta_n \sum_j \sin(k_n x_j) + \sqrt{\frac{\kappa}{2}}\xi \tag{1.2.32c}$$

with optical potential

$$U_n(x, \alpha) = \hbar U_0^n |\alpha|^2 \sin^2(k_n x) + \hbar\eta_n(\alpha + \alpha^*)\sin(k_n x). \tag{1.2.32d}$$

References

1. Walls, D. F. & Milburn, G. J. *Quantum optics* en, 376. ISBN: 9783-5405-88313 (Springer, 1995).
2. Gerry, C. C. & Knight, P. L. *Introductory quantum optics* 317. ISBN: 9780-5215-27354 (Cambridge University Press, 2005).

2. Publication: Self-ordering dynamics of ultracold atoms in multicolored cavity fields

Self-ordering dynamics of ultracold atoms in multicolored cavity fields

S. Krämer and H. Ritsch
Institute for Theoretical Physics, Universität Innsbruck, Technikerstrasse 25, 6020 Innsbruck, Austria

We study light induced spatial crystallization of ultracold quantum particles confined along the axis of a high-Q linear cavity via a transverse multicolor pump. Whenever a pump frequency is tuned close to resonance with a longitudinal cavity mode, the dynamics favors bistable spatial particle ordering into a Bragg grating at a wavelength distance. Simultaneous pumping at several resonant frequencies fosters competition between the different spatial lattice orders, exhibiting complex nonlinear field dynamics involving several metastable atom-field states. For few particles even superpositions of different spatial orders entangled with different light mode amplitudes appear. By a proper choice of trap geometry and pump frequencies a broad variety of many particle Hamiltonians with a nontrivial long range coupling can be emulated in such a setup. When applying quantum Monte Carlo wave function simulations to study time evolution we find simultaneous super radiant scattering into several light modes and the buildup of strong non-classical atom field correlations.

I. INTRODUCTION

When ultracold polarizable particles in an optical resonator are coherently illuminated from the side at sufficient intensity, the system undergoes a transition from homogeneous to crystalline order accompanied by superradiant light scattering into the cavity mode [1–3]. This self ordering process occurs as a quantum phase transition for an ultracold Bose as well as Fermi gas close to zero temperature in the pure quantum regime [4, 5]. To surprising accuracy it can be reinterpreted and understood as implementation of the Dicke superradiant phase transition, where a cavity mode is very strongly coupled to two motional modes of the trapped particles [6–8]. As one of the early and seminal examples of a quantum phase transition [9, 10], the Dicke superradiant phase transition has been studied extensively in theory since its proposition 50 years ago [9]. With the recent successful experimental implementation based on a BEC of cold atoms in a cavity, a large number of more detailed theoretical and numerical studies on the particular properties of this realization, its limitations and new related phenomena like super-solidity have followed [11–15].

The first simple but still surprisingly successful generation of theoretical models was based on a single atomic and a single cavity mode [7]. A particular interesting generalization was introduced by considering this ordering phenomenon in degenerate multi-mode cavity fields and restricting the degrees of freedom of the particle motion to a 2D plane [16]. This opened a new possible route to study a wealth of important quantum solid state phenomena like emergent crystallinity, liquid crystalline phases [16, 17] or quantum neural network models [18] in a well controllable atom-optical configuration. Due to the inherent complexity and technical difficulty of degenerate multi-mode setups, which require at least a 2D geometry, theoretical modeling as well as experimental implementations of such setups are very challenging and have, to our knowledge, not been implemented to date. Recent theoretical generalizations to fermions reveal even more new physical phenomena, e.g. Umklapp lasing or surprisingly reduced ordering thresholds [5, 19, 20].

In this work we investigate an alternative multi-mode extension employing several light frequencies simultaneously, each of them tuned closely to a separate longitudinal cavity mode. As the cavity modes form an equidistant comb of sufficiently distinct frequencies, which is readily available experimentally with modern comb technology, the technical complexity of an implementation seems much less challenging. Moreover, as coherent light scattering between different modes can be neglected and the motion of the particles is confined along the cavity axis, the computational complexity of the model is substantially reduced. This allows explicit numerical treatments, at least for small implementations, where still many of the intriguing phenomena mentioned above should appear. As amplitude, phase and detuning of each mode can be controlled independently, this setup should allow for much more precise control and variability of the dynamics.

While virtually all the existing treatments have ignored the effect of the finite size of the particle trap inside the resonator, here, we explicitly consider particles confined to a finite volume along the cavity axis. Hence, the ground state is not translation invariant and neither are the higher trap eigenmodes which form the ordered pattern. This implies a breakdown of the single mode model for a monochromatic pump. In the multicolor pump case, this induces important extra couplings between many different trap modes, which can be tailored largely by the choice of the pump and trap geometry. In any case, the relevant particle Hilbert space is substantially enlarged.

We will first present the theoretical model assuming the particles to be trapped in a 1D external trap along the cavity axis. For a few generic trap configurations, the scattering and coupling integrals between the light field modes and trapped particle modes can even be calculated analytically, a numerical evaluation for more realistic trap geometries is straightforward. Ultimately, we obtain a well defined effective Hamiltonian consisting of many modes with widely tunable coupling elements. Within this framework at first, we shortly review the single frequency phase transition but account for the full trap dynamics beyond a single excited trap mode. In the last section we increase the number of pump fields and simulate the phase transition and steady states for a multicolor setup.

II. MODEL

We consider a linear cavity of length $2L$ with N_a particles trapped by an external potential $V(x)$ in a finite region along the cavity as depicted in fig. 1. For simplicity we assume the particles to be tightly confined in the radial direction, making their movement effectively one dimensional. The particles with an internal excitation energy $\hbar\omega_a$ and spontaneous decay rate γ are upon adiabatic elimination of the excited state are characterized solely by their center of mass motion and their electric dipole moment, which is strongly coupled to the cavity modes. The atoms are pumped transversely (in y-direction) by N_p different standing wave lasers of frequency

ω_p^k with pump strength E_p^k and polarization orthogonal to the cavity. Different pump frequency components are spaced by multiples of the cavity free spectral range close to the cavity eigenmodes but far from the atomic resonance (fig. 1). Including spontaneous emission of the atoms as well as of the cavity modes, the time evolution of the coupled atom field system can be described by a master equation of the form [8, 21]

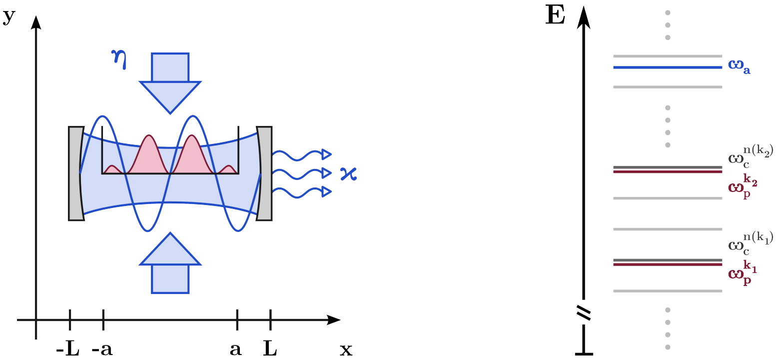

FIG. 1: System setup consisting of N_a quantum particles confined in a box trap $V(x)$ along the cavity axis and illuminated by N_p lasers along the y-direction (left). Frequency diagram showing the pump lasers ω_p^k tuned closely to distinct longitudinal cavity modes $\omega_c^{n_k}$ well below the atomic frequency ω_a (right).

$$\dot{\rho} = -\frac{i}{\hbar}[H,\rho] + \sum_i \gamma_i (2\hat{\sigma}_-^i \rho \hat{\sigma}_+^i - \rho \hat{\sigma}_+^i \hat{\sigma}_-^i - \hat{\sigma}_+^i \hat{\sigma}_-^i \rho) + \sum_n \kappa_n (2\hat{a}_n \rho \hat{a}_n^\dagger - \rho \hat{a}_n^\dagger \hat{a}_n - \hat{a}_n^\dagger \hat{a}_n \rho), \tag{1}$$

where the Hamiltonian is given by

$$H = H_{cavity} + H_{particles} + H_{int} = \sum_{n=1}^{\infty} \hbar \omega_c^n \hat{a}_n^\dagger \hat{a}_n + \sum_{i=1}^{N_{part}} \hbar(\omega_a \hat{\sigma}_+^i \hat{\sigma}_-^i + \frac{\hat{p}_i^2}{2m} + V(\hat{x}_i)) - \sum_{i=1}^{N_{part}} \hat{\vec{d}}_i \hat{\vec{E}}(\hat{x}_i). \tag{2}$$

Here ω_c^n denote the cavity eigenfrequencies. The electric field in the particle-field interaction term, $\hat{\vec{E}}(\hat{x}_i) = \hat{\vec{E}}_c(\hat{x}_i) + \vec{E}_p$, consists of the pump lasers $\vec{E}_p$ modeled as classical standing wave fields of the form $\vec{E}_p = \vec{e}_z \sum_k E_0^k \cos(\omega_p^k t)$ and the cavity field $\hat{\vec{E}}_c(\hat{x}_i) = \vec{e}_z \sum_{n=1}^{\infty} \sqrt{\frac{\hbar \omega_c^n}{2L\epsilon_0}} u_n(\hat{x}_i) a_n +$ h.c.. For a planar cavity the effective mode functions on the axis are simple trigonometric functions $u_n = \sin(k_n(x+L))$, with wave numbers k_n. After adiabatic elimination of the atoms' inner degrees of freedom, elimination of fast rotating terms and change into an interaction picture, the Hamiltonian (appendix A) reduces to

$$\begin{aligned} H = &-\sum_n \Delta_n \hat{a}_n^\dagger \hat{a}_n + \sum_i (\frac{p_i^2}{2\mu} + V(\hat{x}_i)) \\ &+ \sum_{ni} U_0 \omega_c^n \sin^2(k_n(\hat{x}_i - L)) \hat{a}_n^\dagger \hat{a}_n + \sum_{ni} \eta_n \sin(k_n(\hat{x}_i - L))(\hat{a}_n^\dagger + \hat{a}_n) \end{aligned} \tag{3}$$

with

$$U_0 = \frac{\hbar}{2L\epsilon_0} \frac{\omega_a}{\omega_a^2 + \gamma^2} |d_{eg}|^2 \text{ and } \eta_n = \frac{1}{2}\sqrt{\frac{\hbar \omega_c^n}{2L\epsilon_0}} E_0^n \frac{\omega_a}{\omega_a^2 + \gamma^2} |d_{eg}|^2 \tag{4}$$

For a many particle description it is convenient to rewrite the Hamiltonian in second quantized form. With Ψ_i denoting the eigenfunctions of the single particle Hamiltonian $H_{particle}\Psi_i(x) = E_i \Psi_i(x)$ we use $\hat{\Psi}(x) = \sum_i \Psi_i(x) \hat{c}_i$ the Hamiltonian can be compactly written as

$$H = -\sum_n \Delta_n \hat{a}_n^\dagger \hat{a}_n + \sum_i E_i \hat{c}_i^\dagger \hat{c}_i + \sum_{nij} U_0 \omega_n A_{nij} \hat{c}_i^\dagger \hat{c}_j \hat{a}_n^\dagger \hat{a}_n + \sum_{nij} \eta_n B_{nij} \hat{c}_i^\dagger \hat{c}_j (\hat{a}_n^\dagger + \hat{a}_n). \tag{5}$$

Note that we get a variety of opto-mechanical and as well as long range interactions mediated by the cavity photons. The specific physical parameters of any concrete implementation are now contained in the detuning of the pump lasers from their respective cavity mode, the spectrum of trap eigenenergies E_i and the coupling matrices,

$$A_{nij} = \int_{-\infty}^{\infty} \Psi_i^*(x)\Psi_j(x)\sin^2(k_n(x+L))dx \tag{6}$$

$$B_{nij} = \int_{-\infty}^{\infty} \Psi_i^*(x)\Psi_j(x)\sin(k_n(x+L))dx, \tag{7}$$

which determine the various coupling strengths. The variation of the trap and pump geometry results in a very wide range of achievable couplings, possibly usable as a very flexible resource for a quantum simulator. Note that extra restrictions introduced by replacing the particles by fermions will further expand the available options. The B matrices mediate the driving of the system by collective scattering photons into the cavity modes, whereas the A matrices describe the diffractive scattering of the particles between different motional trap modes by the cavity photons. Via tailoring these matrices the number and properties of combined atom field eigenstates can be widely tuned and could provide a unique realization of a quantum spin glass with long-range interaction [11] or generalized forms of Hopfield networks. For several generic cases these matrices can be evaluated explicitly and we will discuss typical examples in the next paragraph.

A. Coupling matrices for particles in a square box potential

We now study basic properties of the above Hamiltonian by means of the generic example of a particle trapped in a box potential of length $2a$, i.e. $V(x) = 0$ when $x \in [-a, a]$ and ∞ otherwise. The eigenfunctions are then $\Psi_i(x) = \frac{1}{\sqrt{a}} c_i \sin(K_i(x+a))$ inside the box and 0 outside of it. Here, $K_i = \frac{\pi}{2a}(i+1)$, $E_i = \frac{\hbar^2}{2\mu}\left(\frac{\pi(i+1)}{2a}\right)^2 = \frac{\hbar^2}{2\mu}K_i^2$ while the coupling matrices A_{nij} and B_{nij} are simple integrals of products of harmonic functions and read (appendix B)

$$A_{nij} = \frac{1}{2}\delta_{ij} + \frac{(-1)^n}{4}\left(f^{\cos}_{i,j,n} + f^{\cos}_{i,j,-n} - f^{\cos}_{i,-j,n} - f^{\cos}_{i,-j,-n}\right) \tag{8}$$

$$B_{nij} = \frac{1}{2}\left(-f^{\sin}_{i,j,n} + f^{\sin}_{-i,j,n} + f^{\sin}_{i,-j,n} + f^{\sin}_{i,j,-n}\right) \tag{9}$$

with $f^{\cos}_{i,j,n} = \operatorname{sinc}\left(\frac{\pi}{2}(i+j+2\frac{a}{L}n)\right)\cos\left(\frac{\pi}{2}(i+j)\right)$ and $f^{\sin}_{i,j,n} = \operatorname{sinc}\left(\frac{\pi}{2}(i+j+\frac{a}{L}n)\right)\sin\left(\frac{\pi}{2}(i+j+n)\right)$. For a careful choice of trap length a and selection of cavity modes (e.g. $a = L/4$, $n \in \{11, 19, 27\}$) there are only few nonzero elements, while in general virtually all trap modes can be coupled. As a typical example we will choose to pump at the two cavity eigenmodes 11 and 19 with $a = L/4$. Pumping at the 11th cavity mode frequency only couples the 2nd and 4th atom mode to the atomic ground state in a significant way, while it is the 3rd and 5th motional mode for the 19th cavity mode. Similarly, the 2nd and 4th mode are connected to the 5th and 7th mode. The cavity mode functions, atomic trap eigenfunctions and matrix elements for the second case are

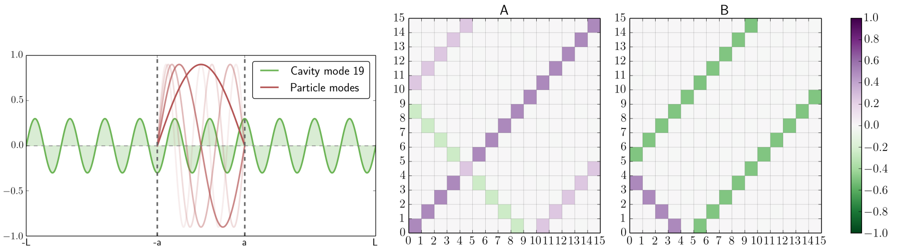

FIG. 2: First few particle trap eigenmodes and 19th cavity mode (left); coupling matrices A (middle) and B (right) between light fields and atomic modes

shown in fig. 2. In addition we see that by internal scattering via the A matrix the 5^{th} and 7^{th} mode are also populated from the 11^{th} field mode. Note that in addition to a finite coupling strength energy conservation has to be fulfilled for efficient population transfer. This can be controlled via the detuning between the pumping laser and the cavity mode, Δ_n, at least to some extent. Nevertheless, even in this simple generic case a two mode picture per excitation frequency as it appears in an infinite trap size limit cannot be expected.

B. Coupling matrices for a harmonic atom trap

Note that for a square-well potential of tailored length as above, we find rather sparsely populated coupling matrices with nonzero entries determined by the specific choice of the cavity length, trap size and pump mode. In the more realistic case of e.g. a Gaussian trap, the matrices are, as shown in fig. 3, much more densely populated. This considerably enlarges the necessary computational basis for quantitatively correct numerical modeling on the one hand, but allows the study of a wider class of Hamiltonians on the other hand. While this is certainly interesting and worthwhile to pursue, we will study the simple, more easily calculable box potential model.

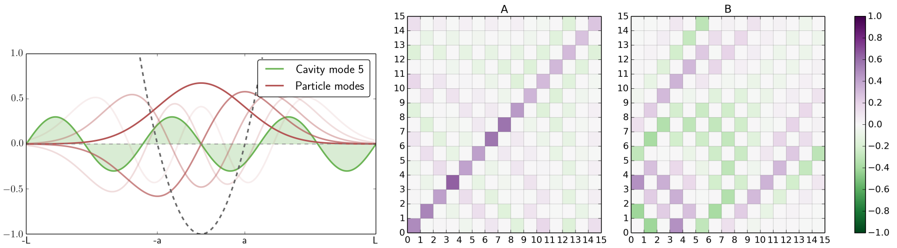

FIG. 3: First few particle eigenmodes of an harmonic trap potential and 5-th cavity mode (left). Coupling matrices A (middle) and B (right) between light fields and atomic modes for a harmonic particle trap positioned at the cavity center

III. SELF-ORDERING DYNAMICS WITH A MONOCHROMATIC PUMP

The B coupling matrices calculated above show that photon scattering into the cavity mode couples several motional modes already. Actually, for trapped particles, where the translation symmetry of the ground state is lost, there are always at least two motional modes that exhibit a considerable coupling. These motional modes are in turn coupled further to other eigenstates via the B as well as the A matrix. Of course, only if the corresponding motional transition is also energy resonant within the width of the cavity mode, one can expect a significant excitation of a particular mode. Based on this line of argumentation, higher order motional modes have been widely neglected in many theoretical models so far [22], even in the bad cavity case. In the present work, we treat the more realistic but computationally more complex case of a finite particle trap placed along the cavity axis, so that we need to include a suitable range of contributing trap eigenstates. As the nonlinear equations cannot be easily solved analytically, we resort to numerical solutions of the corresponding master equation using the *zvode* wrapper of the numerical library*scipy* [23]. For higher dimensional problems, as it is mostly the case if more than one cavity mode is pumped, we have to settle for QMCWF methods which makes it harder to obtain accurate values for entanglement and correlations but in return allows us to study the dynamics of single trajectories which experimentally corresponds to continuous measurement of leaking photons. These trajectories are often easier to comprehend intuitively, mostly due to the fact that they work in terms of wave functions instead of density matrices, and therefore allow for a better qualitative insight into the underlying processes. To examine intrinsic resonances in the response of the coupled system to find the physically most interesting operating frequencies, we first probe the system by tuning the pump laser across the empty cavity resonance at low intensity. As shown in the left graph in fig. 4, we clearly see a red shift compared to the empty cavity resonance. Its maximum as well as its position changes nonlinearly with the pump strength (blue to green to red curve) which indicates a more efficient coupling by tighter particle localization at the anti nodes of the

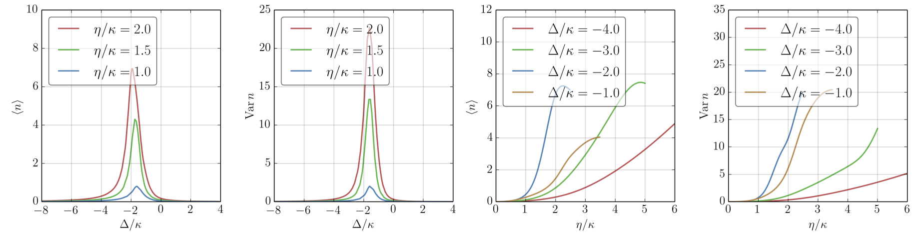

FIG. 4: Stationary average number and variance of photons scattered into the cavity mode by a single atom initially prepared in the trap ground state as function of detuning between pump laser and cavity mode (two pictures on the left). Photon number and variance as a function of the pump strength for different negative detunings showing the appearance of a threshold pump strength (two pictures on the right). Here we have chosen the case of mode 11 as discussed above.

field. As expected, we get motional heating on the blue side of the effective resonance leading to less effective particle field coupling and line broadening. In the next subfigure to the right we show the large enhancement of the variance of the photon number for stronger pumping, yielding a first indication of the presence of critical fluctuations at a certain pump strength. In any case, we see a strong deviation from a classical coherent intracavity field state (note the changed axis scale). The origin of these fluctuations will become much more obvious by looking at the field Q-function which we will study in more detail in the next section on the dynamics of the ordering transition. In the rightmost figure we show the stationary photon number dependence of the intra cavity field as a function of the pump amplitude for fixed detuning. Operating closely to cavity resonance on the red detuned side the transition from zero to finite field occurs at lower pump strength and much steeper (blue line) until we end up at the blue side of the effective resonance (orange line), where ordering is connected to heating and counteracts coherent scattering. Therefore, in the following we will always consider sufficient red detuning of the pump fields to ensure combined ordering and cooling.

A. Single particle ordering dynamics

As indicated by the frequency scans above and also found in classical models [24], the instability of the trap ground state against light scattering is connected to a transition to an ordered phase only if we operate well on the cooling red side of the effective cavity resonance. Otherwise the particles are soon heated out of the ordered state. A sufficiently large red detuning was thus also used in the Zürich experiments [6]. For a numerical analysis of the transition amplitude from the weakly scattering trap ground state to an ordered radiating state, we will first start with a single particle and a single frequency model, which can be solved directly for a wide parameter range without too much numerical effort. In this case spatial order is represented by a quantum superposition of the single particle wave function with regularly spaced periodic maxima. Such a state could of course not occur in any classical single particle model.

In the following we present some typical results. Clearly, as shown in fig. 4, for suitably chosen detuning, i.e. $\Delta = -3\kappa$, we see a pronounced threshold for the pump amplitude, above which the number of scattered photons and also the corresponding fluctuations strongly increase. Even more detailed insight in the field properties can be gained from the corresponding Q-functions shown in fig. 5 for three typical pump strengths. We observe how the distribution changes significantly from a vacuum like distribution via a squeezed vacuum type shape to a clear bimodal phase space distribution, where the field is concentrated around two regions of opposite phase. At the same time we find a concurrent fast grow of the population of the third and fifth excited trap states. For the strongest pump even higher trap modes, in this case the 8^{th} and 10^{th}, get substantially occupied (fig. 6). Thus, even for a single pump frequency a Dicke-type two mode approximation will fail even for a moderate pumping power. As expected, these modes are phase locked by the excitation dynamics so that the field state is directly connected to a characteristic change in the position distribution of particles towards a regular quasi periodic order as shown in fig. 7. It is particularly interesting to note, that looking at the particle density, which exhibits a half wavelength modulation and the mode function depicted in fig. 2, one might at first expect zero light scattering, as the overlap of the density with positive and negative sections of the mode amplitude are equal and thus the scattering should cancel. Again, this is of course a classical argument, which is not

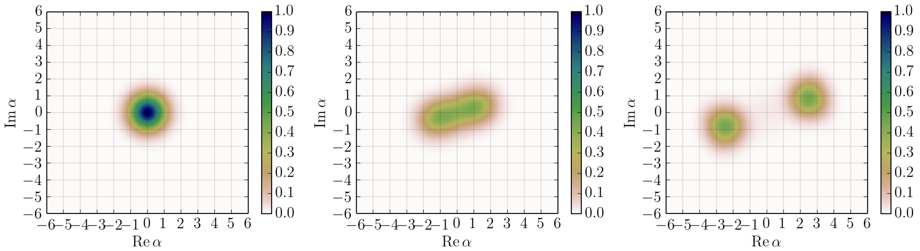

FIG. 5: Stationary density plot of the field Q-function below ($\eta = 0\kappa$) (a), at ($\eta = 1.5\kappa$) (b) and above $\eta = 4\kappa$ threshold (c) for a pump close to cavity mode 19 as above. The detuning is set to $\Delta = -3\kappa$ and $U_0 = -2\kappa$.

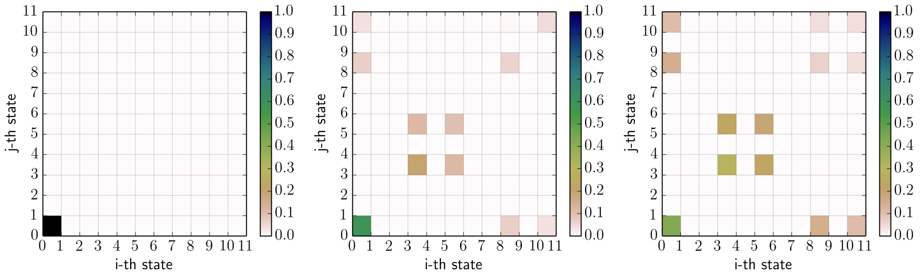

FIG. 6: Stationary particle eigenstate occupation probabilities for the same parameters as above. Below (a), at (b) and above threshold (c) for a single mode.

relevant in our full quantum system. The leftmost and middle right density peak is quantum correlated to light scattered with positive field amplitude, while the other two peaks generate a negative pump amplitude. As the corresponding wave functions parts hardly overlap the two contributions will not cancel by interference. Analysis of the numerical results reveals that single MCWF trajectories starting in the ground state of the trap evolve in the long time limit to a state that can be extremely well described by

$$|\psi_{t\to\infty}\rangle = \frac{1}{\sqrt{2}}(|c\rangle|\alpha\rangle + |d\rangle|-\alpha\rangle), \tag{10}$$

where the particle states $|c\rangle$ and $|d\rangle$ are orthogonal. The particle states as well as the value of α will vary moderately among different trajectories. Hence, the steady state of the master equation is in general a mixed state that can only be approximated roughly by $\rho_{t\to\infty} = |\psi_{t\to\infty}\rangle\langle\psi_{t\to\infty}|$. However, the reduced density operators for the field as well as for the particles,

$$\rho^{field}_{t\to\infty} = \frac{1}{2}(|\alpha\rangle\langle\alpha| + |-\alpha\rangle\langle-\alpha|) \tag{11}$$

$$\rho^{particles}_{t\to\infty} = \frac{1-v}{2}\frac{(|c\rangle - |d\rangle)(\langle c| - \langle d|)}{2} + \frac{1+v}{2}\frac{(|c\rangle + |d\rangle)(\langle c| + \langle d|)}{2}, \tag{12}$$

where $v = \langle\alpha|\alpha\rangle = e^{-2|\alpha|^2}$, closely match the results of the numerical simulations of the master equation. Overall, we can reproduce several of the results obtained for the microscopic self-ordering of a single particle in two prescribed wells along the pump axis [25].

B. Two particle self-ordering

When more than one particle is trapped within the cavity, they will of course collectively scatter light and thus become correlated. Their accessible Hilbert space grows very fast since both can occupy a wide range

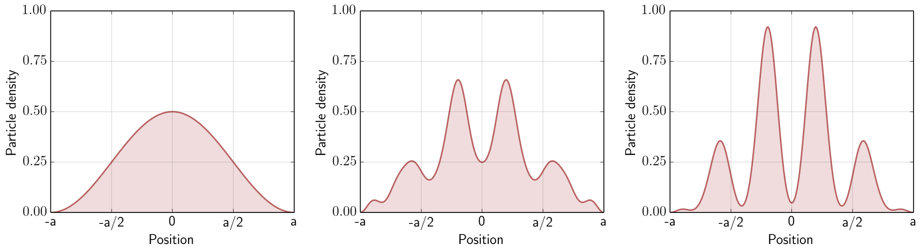

FIG. 7: Stationary particle position density below (a), at (b) and above threshold (c) for a single mode showing increased ordering. Same parameters as above.

of trap states. Even without collisional interaction, the time evolution becomes much more complex in the two particle case. Nevertheless, the average particle density, which is of central importance to light scattering, still generally looks similar. Thus, the two-particle threshold and photon number fluctuations qualitatively do not differ by much apart from a common shift and scaling. As indicated by fig. 8, the essence of the phase transition properties prevails. Extra peaks in the transmission indicate different pair correlations of the atoms as discussed in some detail in ref. [26]. These can now be visualized easily by showing the spatial density correlations. Interestingly, the system now possesses several wave functions of almost equal density distribution, which differ only in quantum statistical properties. Let us demonstrate this in some more detail by explicitly plotting the spatial particle-particle correlations in fig. 9. We see that in the joint spatial probability density above threshold, as depicted on the right, the diagonal elements are very pronounced. This shows that we do not get a simple product state of the two particles but a strong correlation between their positions. This pairing again goes beyond a simple Dicke two mode model, which offers the same single motional mode for all particles.

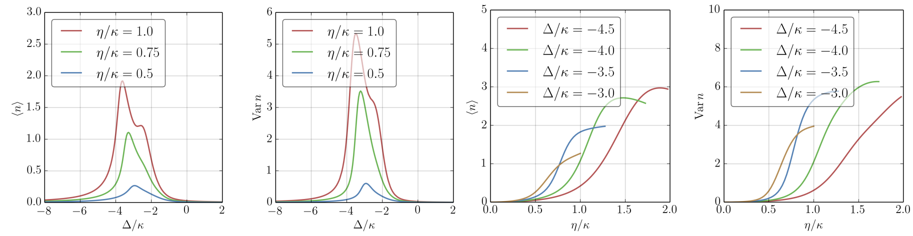

FIG. 8: Stationary expectation number of photons scattered into the cavity mode (leftmost graph) and their variance (adjacent right) for two atoms prepared in the trap ground state and different pump strengths as a function of the detunings chosen equal for both modes. The two plots on the right show the same behavior as a function of the pump strength for different negative detunings, where self ordering is expected.

IV. SIMULTANEOUS TWO COLOR PUMPING

Let us now turn to a completely new parameter regime. As we have seen above, for a single pump frequency above threshold the particles attain a rather complex superposition of trap eigenstates, which can be split approximately into two components corresponding to the two distinct field states of equal amplitude but opposite phase. In this section we now allow for two simultaneously injected excitation frequencies. Both frequencies are tuned closely to distinct longitudinal cavity modes, which are assumed to be separated sufficiently far, so that scattering of each field can occur solely into the corresponding mode. Each of the two laser powers and the detuning from their corresponding mode can be varied independently across the ordering threshold and for independent injection again has two possible stationary states. As one of our central goals in this work we now

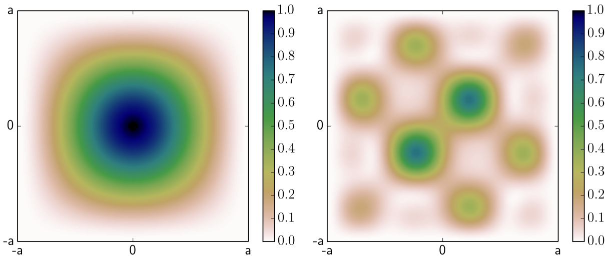

FIG. 9: Position density distribution $\rho_{x_1 x_2}$ for 2 particles and a single pumped mode 19 below (left) and above threshold (right) for $\eta = 4\kappa$ and $\Delta = -3\kappa$, showing a clear preference of the particles to occupy the same wells, or at least wells with the same associated field state.

study key properties of the enriched dynamics for simultaneous operation of these pumps.

A. Stationary state manifold for two color pump

As a generic example we choose simultaneous operation on the 11th and 19th cavity mode and a trap size of 1/4-th of the cavity length. This minimizes cross coupling matrix elements which facilitates an easier analysis of the complexity of the dynamics. As both lasers act on the same particles, we find a competition between the possible optimal orders for each field. It is now interesting to see for which pump ratios and strengths a single or even both orders are at least metastable and when the system is able to find completely new spatial distributions close to optimum for both fields. In general, besides a global optimum configuration several metastable local scattering maxima and potential energy minima exist. We will use QMCWF simulations, allowing us to study the multitude of quasi stationary solutions and also to retrieve important characteristics of the time evolution. As any momentary particular order leads to a characteristic scattering, we can use the photon number to quantify the corresponding order parameters. To get a first insight, in fig. 10 we plot the stationary averages of the photon numbers in the two modes, first as a function of the detunings for fixed pump amplitudes, then as a function of the two pump amplitudes for fixed negative detunings. While for preferential pumping of one field the corresponding photon number and a spatial order clearly dominates, a finite pump at one field can either suppress or enhance the scattering and spatial order of the other mode. For our chosen example the threshold of mode 11 is shifted upwards by the mode 19 field, while almost no effect is visible in the other direction. For close to equal pump strength, there are regions in parameter space where both modes oscillate simultaneously. This can be seen clearly in fig. 11 (first two images) showing the corresponding Q-functions. A bimodal distribution is also visible in the spatial density distribution shown in the third image of fig. 11.

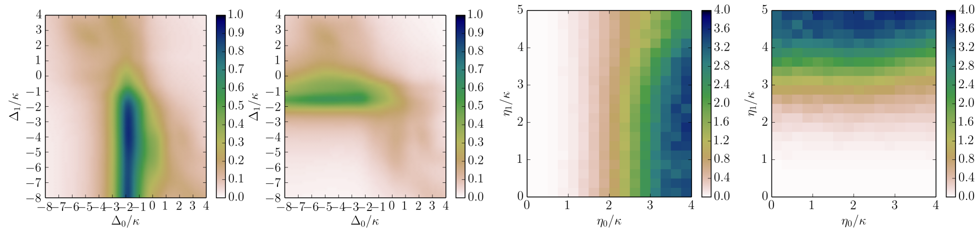

FIG. 10: Stationary photon number in mode 11 (a) and mode 19 (b) as a function of the detunings Δ_0, Δ_1 for equal pump amplitudes $\eta = 1\kappa$. Stationary photon number in mode 11 (c) and mode 19 (d) as a function of the pump amplitudes η_0, η_1 for equal detunings $\Delta = -3\kappa$.

Note, that no direct light scattering between the modes is possible because their frequency difference is too large. As can be inferred from the missing vacuum contribution in the Q-functions and the dominance of the diagonal in the photon number distribution on the lower left, the two modes are oscillating at the same time. Microscopically this corresponds to an atom-field state of the approximate form

$$|\psi_{t\to\infty}\rangle = \frac{1}{\sqrt{2}}(|c\rangle|\alpha_0\rangle|\alpha_1\rangle + |d\rangle|-\alpha_0\rangle|-\alpha_1\rangle). \tag{13}$$

Each field amplitude pertains to a characteristic component of the particle density distribution, possibly allowing for various orthogonal combinations. Again, the number of such states rapidly grows with increasing particle number, so that even for such a small system size one quickly reaches the limits of classical computers. Experimentally, much higher particle and mode numbers seem easily possible, allowing to study and simulate Hamiltonians of the type of eq. 5.

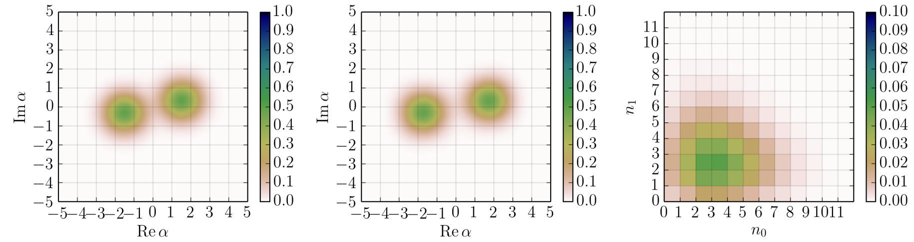

FIG. 11: (a) Averaged Q-function of mode 11, (b) Q-function of mode 19 and (c) joint photon number distribution probabilities $\rho_{n_1 n_2}$ for two simultaneously strongly pumped modes where we have chosen $\eta_0 = 5\kappa, \eta_1 = 6\kappa$ and $\Delta_0 = \Delta_1 = -4\kappa$.

B. Time evolution between different metastable states

So far we have concentrated on average stationary long time properties of the system to characterize the multitude of stationary quantum states and their intrinsic correlations. It is, however, almost equally interesting and important to study the time evolution and temporal fluctuations of the system. Due to limited space, here, we will restrict ourselves to a single typical example when the pump is tuned somewhat above the common oscillation threshold of the system. In this case several possible spatial configurations will compete and pure quantum fluctuations turn out to be sufficient to induce transitions between different spatial orders. This is presented in the final figure fig. 12 where we show the temporal behavior of a typical single trajectory. Quantum jumps in the form of photo detection events eventually lead to a particle rearrangement between different spatial structures, which can also be accompanied by phase reversals in the field modes as depicted in the third subgraph from above. In some cases even transitions back to a completely disordered state where light scattering stops almost completely can occur (see last third on the right). In the ordered time periods we observe, as shown in the lowest graph, that the acquired state is very close to the heuristically expected and predicted cat like quantum state of eq. 13. The parameters of this state are dynamically obtained from the momentary maxima of the field Q-function. Note that each trajectory thus remains a coherent superposition between states of opposite field phase and the system does not break the inversion symmetry in respect to the trap center. As state changes can be triggered by pure quantum fluctuations, one can of course actively switch between them by injecting corresponding signals into the cavity mode. Their stability can be increased by using higher pump powers. All these fascinating features are, unfortunately, computationally very time consuming and beyond the scope of this work at this point. Qualitatively such effects could be investigated in strongly mode truncated models or by adiabatic elimination of the field dynamics.

V. CONCLUSIONS

Adding extra pump frequencies to the self-ordering dynamics of ultracold particles in a cavity field significantly changes the dynamics and enlarges the complexity of the system from a dynamical as well as computational

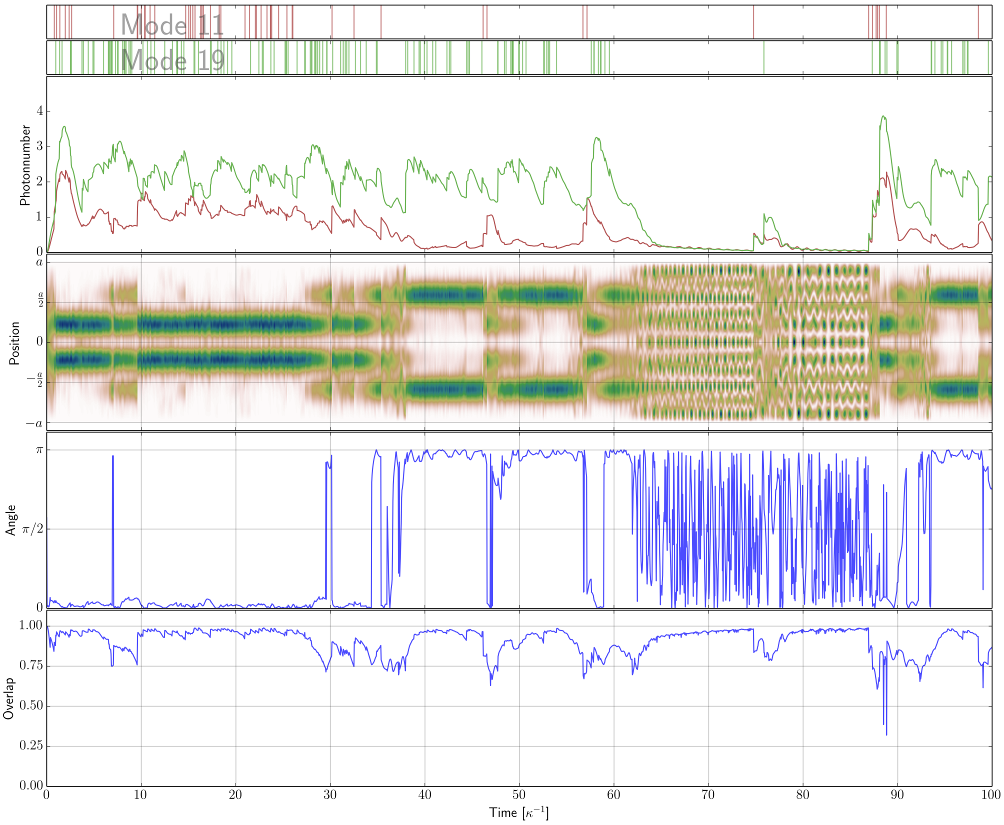

FIG. 12: Single Monte Carlo wave function trajectory for a trapped particle with a two-color pump. The upper part shows intra cavity photon numbers and photo-detection events in the two modes, which clearly correlates with the spatial density distribution of the particles below. In the last two plots we show the changes of the relative field phases as well as the large momentary overlap with the heuristically expected approximate state of the form of eq. 13 with dynamically optimized state parameters.

point of view. Even with moderate particle and mode numbers, the limits of computability are soon reached. An alternative description in terms of an effective multi-mode Dicke model might catch essential qualitative features of the dynamics but quantitative reliable modeling is hardly possible. By including the trap dynamics in a consistent form we get a complex, widely tunable and very precisely controllable coupled quantum system, which can be mapped to a coupled oscillator system with tailorable long and short range interactions. The observation of photon scattering allows precise real time monitoring of the atomic dynamics, which can then be controlled also by pump strength and detuning. With the help of frequency combs suitable cavity matched frequencies are available over a very wide range of longitudinal modes without the need for individual stabilization of each color. This should allow experimental studies far beyond Dicke physics as a very general quantum simulator.

In this work, we have mainly derived the basic Hamiltonian and only scratched the surface of the underlying complex nonlinear dynamics by means of a few simple but typical examples. A systematic investigation is certainly necessary and worthwhile but unfortunately beyond the scope of this work. Even more complex results could be expected from a generalization to fermionic particles [5] or particles with several internal levels [27]. Of course, one of the most interesting aspects and motivations of this approach is the fact that only minor additions to current experimental setups are required and the theoretical model for the current generations of experiments have proven to be surprisingly accurate and reliable [6, 8, 17, 28, 29].

VI. ACKNOWLEDGMENTS

This work was supported by the Austrian Science Fund FWF project F4013 within the SFB FoQus. We also would like to thank Wolfgang Niedenzu for invaluable physical discussions and Laurin Ostermann for taking the language of this document a step closer to English.

[1] P. Domokos and H. Ritsch, Physical review letters **89**, 253003 (2002).
[2] A. T. Black, H. W. Chan, and V. Vuletić, Physical review letters **91**, 203001 (2003).
[3] K. Arnold, M. Baden, and M. Barrett, Physical Review Letters **109**, 153002 (2012).
[4] C. Maschler, H. Ritsch, A. Vukics, and P. Domokos, Optics Communications **273**, 446 (2007).
[5] F. Piazza and P. Strack, arXiv preprint arXiv:1309.2714 (2013).
[6] K. Baumann, C. Guerlin, F. Brennecke, and T. Esslinger, Nature **464**, 1301 (2010).
[7] D. Nagy, G. Kónya, G. Szirmai, and P. Domokos, Physical review letters **104**, 130401 (2010).
[8] H. Ritsch, P. Domokos, F. Brennecke, and T. Esslinger, Reviews of Modern Physics **85**, 553 (2013).
[9] K. Hepp and E. H. Lieb, Annals of Physics **76**, 360 (1973).
[10] S. Sachdev, *Quantum phase transitions* (Wiley Online Library, 2007).
[11] P. Strack and S. Sachdev, Physical review letters **107**, 277202 (2011).
[12] D. Tolkunov and D. Solenov, arXiv preprint cond-mat/0606270 (2006).
[13] F. Piazza, P. Strack, and W. Zwerger, arXiv preprint arXiv:1305.2928 (2013).
[14] G. Kónya, D. Nagy, G. Szirmai, and P. Domokos, Physical Review A **86**, 013641 (2012).
[15] Y. Li, L. He, and W. Hofstetter, Physical Review A **87**, 051604 (2013).
[16] S. Gopalakrishnan, B. Lev, and P. Goldbart, Nature Physics **5**, 845 (2009).
[17] S. Gopalakrishnan, B. L. Lev, and P. M. Goldbart, Phys. Rev. A **82**, 043612 (2010).
[18] S. Gopalakrishnan, B. L. Lev, and P. M. Goldbart, Philosophical Magazine **92**, 353 (2012).
[19] J. Keeling, M. Bhaseen, and B. Simons, arXiv preprint arXiv:1309.2464 (2013).
[20] Y. Chen, Z. Yu, and H. Zhai, arXiv preprint arXiv:1309.3784 (2013).
[21] J. Asbóth, P. Domokos, H. Ritsch, and A. Vukics, Physical Review A **72**, 053417 (2005).
[22] G. Kónya, G. Szirmai, and P. Domokos, The European Physical Journal D **65**, 33 (2011).
[23] E. Jones, T. Oliphant, P. Peterson, et al., *SciPy: Open source scientific tools for Python* (2001–), URL `http://www.scipy.org/`.
[24] T. Grießer, H. Ritsch, M. Hemmerling, and G. Robb, The European Physical Journal D **58**, 349 (2010).
[25] A. Vukics, C. Maschler, and H. Ritsch, New Journal of Physics **9**, 255 (2007).
[26] I. B. Mekhov, C. Maschler, and H. Ritsch, Nature Physics **3**, 319 (2007).
[27] E. G. Dalla Torre, S. Diehl, M. D. Lukin, S. Sachdev, and P. Strack, Physical Review A **87**, 023831 (2013).
[28] M. Wolke, J. Klinner, H. Keßler, and A. Hemmerich, Science **337**, 75 (2012).
[29] R. M. Sandner, W. Niedenzu, and H. Ritsch, EPL (Europhysics Letters) **104**, 43001 (2013).

3. Outlook: Steady-state solutions

An interesting feature of self-organization is that in the case of a single pump laser there are two equally likely steady state solutions. The system has to decide spontaneously which one of them it will take on. By adding additional lasers it seems plausible that even more possible steady states might emerge. To look for this effect we use the semi-classical equations as well as a slightly more quantum approach along the lines of a cumulant expansion to try to identify such solutions.

3.1. 1st approach: Semi-classical equations

For the sake of simplicity we neglect the noise term and the non-linearity U_0 more or less neglecting any quantum effects. The semi-classical equations then lead to the following conditions for the steady states:

$$v_j = 0 \tag{3.1.1a}$$

$$\alpha_n = \frac{N\eta_n\theta_n}{\Delta_c^n + i\kappa_n} \tag{3.1.1b}$$

$$\frac{\partial \sum_n U_n(x_j, \alpha_n)}{\partial x_j} = 0 \tag{3.1.1c}$$

where every single particle sees the same optical potential

$$U(x) = \hbar \sum_n \eta_n(\alpha_n + \alpha_n^*) \sin(k_n x). \tag{3.1.1d}$$

Finding particle distributions that solve all these equations simultaneously is not straight forward. While using an iterative fixed point approach is straight forward there is no guarantee that it finds all possible solutions. Basically, every point in the $N_{\text{particlenumber}}$ dimensional space has to be checked. The key observation is that all possible optical potentials are identified by $N_{\text{cavitmodes}}$ real numbers $\xi_n = \eta_n(\alpha_n + \alpha_n^*)$

$$U_\xi(x) = \sum_n \xi_n \sin(k_n x) \tag{3.1.2}$$

For a fixed potential U_ξ, we know that in the steady state the particles have to be located in local minima. The exact distribution among those minima does not change the optical potential, but of course the self-consistently determined pump strengths have to be adapted.

Single-mode

In the case of only a single pumped mode the situation becomes especially simple. Then the particles are either all in the maxima or all in the minima of the optical potential depending on the sign of the parameter ξ. The order parameter is then either $+1$ or -1 so that the pump strength for a given optical potential parameter is

$$\sqrt{N}\eta = \sqrt{\frac{\Delta_c^2 + \kappa^2}{|\Delta_c|}|\xi|}. \tag{3.1.3}$$

In Fig. 3.1 these relations are plotted and it is graphically clear that for every choice of pump strength $\eta > 0$ there are always two possible solutions which correspond to the previously mentioned cases of all particles sitting in the maxima or all particles sitting in the minima.

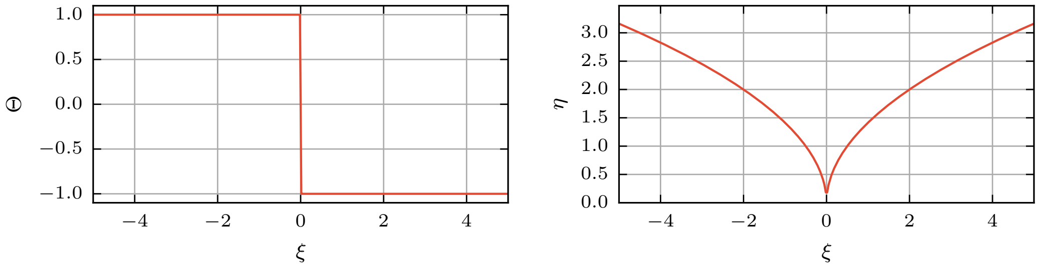

Figure 3.1.: Order parameter and pump strength depending on light potential parameter ξ for a single mode in the semi-classical limit.

Double-mode

The situation gets much more interesting if more than one mode is pumped. We consider in the following a system where two modes with wave number ratio $\frac{k_1}{k_2} = \frac{2}{3}$ are pumped as shown in Fig. 3.2a. Some of the possible optical potentials are shown in Fig. 3.2b where the color encodes the relative strengths of the two modes. The

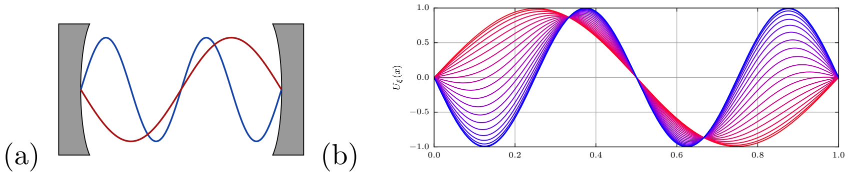

Figure 3.2.: (a) Modes chosen for the simulation: First (red) and third (blue) harmonic. (b) Resulting optical potentials for different choices of ξ_1 and ξ_2. Blue if the third harmonic is dominating, red when the first harmonic is dominating.

number of local minima depends on the exact choice of ξ_n but for now we assume that all particles are placed in the global minimum. As long as there is only one global minimum the state and therefore also the order parameters (Fig. 3.3) and the real pump strengths (Fig. 3.4) are uniquely defined by the optical potential. Choosing a specific pump strength for η_1 and η_2 is equivalent to selecting isolines in Fig. 3.4. Since both conditions have to be fulfilled at the same time this amounts to intersecting these two isolines as is indicated in Fig. 3.4(c).

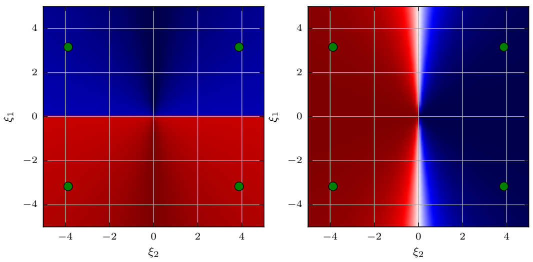

Figure 3.3.: Order parameters in respect to the first (left) and third (right) harmonic mode for different choices of light potential ξ_1 and ξ_2. Blue is completely anti-ordered, red completely ordered.

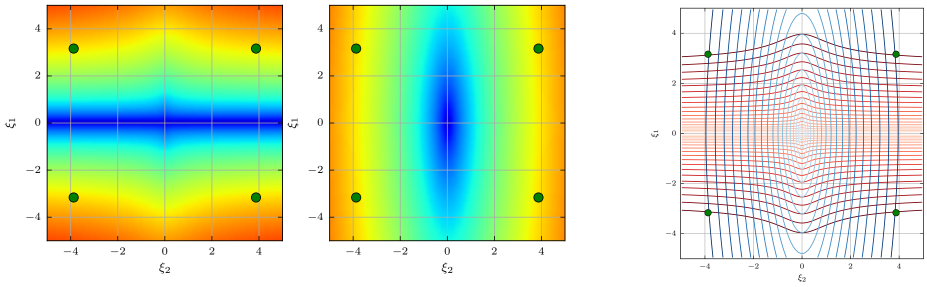

Figure 3.4.: Self-consistently determined pump strengths for different choices of light potential parameters ξ_1 and ξ_2 in respect to the first (a) and third (b) harmonic. (c) Isolines of the self-consistently determined pump strengths for different choices of light potential parameters ξ_n with all particles in the global minimum. Intersection points for the isolines $\eta_1 = c_1$ and $\eta_2 = c_2$ correspond to different possible steady state optical potentials for a fixed set of pump strengths.

3.2. 2nd approach: 1st order cumulant expansion

For small enough systems consisting to up to only two particles and two cavity modes it is possible to simulate the complete master equation numerically. For the steady state of a moderately pumped system this reveals that the quantum correlations between the light modes and the particles and especially between the different light modes directly are rather small. Depending on the initial state and the strength of the coupling terms this is, however, only to a much lesser extent true during earlier parts of the time evolution. Therefore, a factorized Ansatz for the steady state,

$$\rho^{\mathrm{ss}} = \rho_p \bigotimes_n \rho_f^{(n)}, \tag{3.2.1}$$

seems justified. Tracing out all field degrees of freedom in the master equation results in the condition

$$0 = \dot{\rho}_p = \left[H^{\mathrm{eff}}, \rho_p\right] \tag{3.2.2}$$

for the particle density operator with effective Hamiltonian

$$H^{\mathrm{eff}} = H_p + \sum_n \hbar U_0^n \langle a_n^\dagger a_n \rangle \hat{A}_n + \sum_n \hbar \eta_n (\langle a_n^\dagger \rangle + \langle a_n \rangle) \hat{B}_n. \tag{3.2.3}$$

This Hamiltonian depends on the expectation values $\langle a_n \rangle$ which can be calculated in the steady state case to be

$$\langle a_n \rangle = \frac{\eta \langle \hat{B}_n \rangle}{\Delta_c^n - U_0^n \langle \hat{A}_n \rangle + i\kappa_n} \tag{3.2.4}$$

The particle equation 3.2.2 and the equations for the cavity modes 3.2.4 are coupled nonlinearly and solutions have to simultaneously solve all of them. Similarly to the classical case in the previous section it is in principle possible to use a fixed point method to find steady states. However, again it's not assured that all solutions are found.

Single-mode

Neglecting the U_0 term and reintroducing the light potential parameter used in the last section results in

$$H^{\mathrm{eff}} = H_p + \hbar \eta_n (\langle a_n^\dagger \rangle + \langle a_n \rangle) \hat{B}_n \equiv H_p + \xi \hat{B}_n$$

We solve the steady state particle equation 3.2.2 by determining the ground state of the effective Hamiltonian

$$H(\xi) |\Psi_0(\xi)\rangle = E_\xi |\Psi_0(\xi)\rangle,$$

Then the order parameter is

$$\langle \hat{B} \rangle = \langle \Psi_0(\xi) | \hat{B} | \Psi_0(\xi) \rangle,$$

the pump parameter can be determined by

$$\eta(\xi) = \sqrt{\frac{\Delta_c^2 + \kappa^2}{\Delta_c \langle \hat{B} \rangle} \xi},$$

and the cavity mode is in a coherent state with

$$\alpha = \frac{\eta(\xi) \langle \hat{B} \rangle}{\Delta_c + i\kappa}.$$

Now to answer the question if the system has several steady states for a given pump strength we just have to determine if $\eta(\xi) = \eta_0$ has more than one solutions for a given η_0. A few examples are shown in the figures 3.5, 3.6 and 3.7.

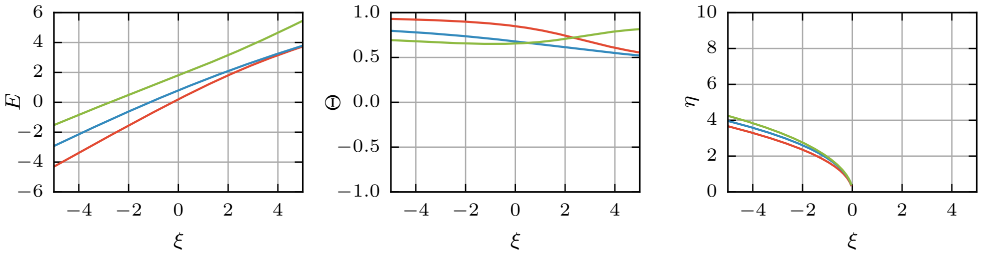

Figure 3.5.: Total energy, order parameter and pump strength for varying perturbation strength ξ for the ground state (red), first excited state (blue) and second excited state (green). The particles are trapped in a box potential of equal length as the cavity and only the fundamental mode of the cavity is pumped. As seen in the third image, for a given pump strength there is only one possible solution.

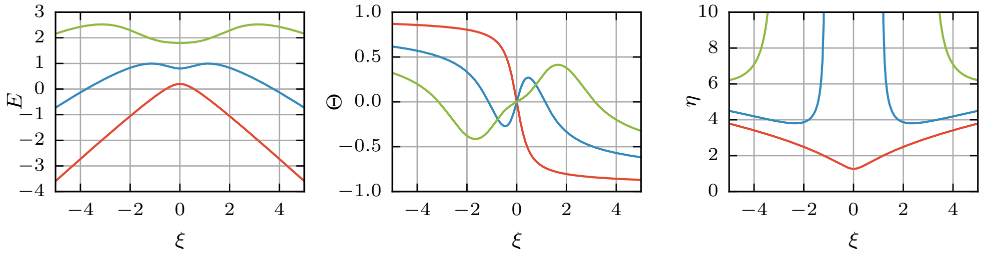

Figure 3.6.: Total energy, order parameter and pump strength for varying perturbation strength ξ for the ground state (red), first excited state (blue) and second excited state (green). The particles are trapped in a box potential of equal length as the cavity and only the first harmonic mode of the cavity is pumped. This is equivalent to the usual self organization situation where two possible solutions exist.

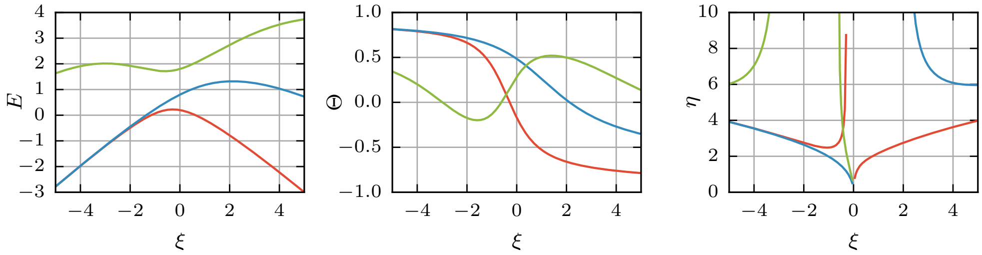

Figure 3.7.: Total energy, order parameter and pump strength for varying perturbation strength ξ for the ground state (red), first excited state (blue) and second excited state (green). The particles are trapped in a box potential of equal length as the cavity and only the second harmonic mode of the cavity is pumped.

Part II.

Dipole-dipole interaction in large spin systems

4. Introduction

The second part of this thesis is focused on how the dynamics of a particle and especially the emittance of photons from it is influenced by the presence of other nearby particles.

Several different quantum mechanical systems where this effect may be of interest are investigated. For most cases its magnitude is negligibly small compared to other more dominating processes, however, for large particle numbers in close enough vicinity it can be of significance.

The first example is the superradiant laser which can be modeled similarly to the traditional laser as N-particles inside of a cavity. The crucial difference is that the system is operated in the bad cavity limit and therefore instead of the many photons that are traditionally needed for lasing only a few or even less than one photons are captured inside the cavity at a time. The excitations are instead stored inside of the particles and the cavity is mainly used to synchronize the internal particle dynamics [1].

As second example, we investigate optical lattice clocks. Atoms containing a state which decays very slowly into another state, i.e. a clock transition, are used as very accurate frequency reference. Increasing the number of atoms by storing them in an optical lattice allows a further increase of accuracy. Averaging over all particles results in an improvement proportional to the square root of the particle number but only if the particles are not interacting with each other [2, 3].

The general description of this phenomenon, which was derived by Lehmberg in 1970, will be sketched in the next section [4, 5]. It shows that this problem can essentially be reduced to two mechanisms. A dipole-dipole interaction resulting in an energy shift of the internal particle transitions and additional two-particle decay channels describing incoherent transfer of excitations from one particle to another via a photon. A possible consequence of this compared to the independent particle case can be a highly enhanced emission rate of photons from the system which is also called superradiance. Depending on the concrete distribution of the particles also the contrary situation, subradiance, can be reached where the photon emission rate is highly diminished. Simply by varying the geometry of the system, i.e. changing the relative position of the particles, can completely change the system behavior resulting in rather complex dynamics.

References

1. Maier, T., Kraemer, S., Ostermann, L. & Ritsch, H. A superradiant clock laser on a magic wavelength optical lattice. *Optics Express* **22,** 13269. ISSN: 1094-4087 (2014).
2. Krämer, S. & Ritsch, H. Generalized mean-field approach to simulate the dynamics of large open spin ensembles with long range interactions. *The European Physical Journal D* **69,** 282. ISSN: 1434-6060 (2015).
3. Krämer, S., Ostermann, L. & Ritsch, H. Optimized geometries for future generation optical lattice clocks. *EPL (Europhysics Letters)* **114,** 14003. ISSN: 0295-5075 (2016).
4. Lehmberg, R. H. Radiation from an N -Atom System. II. Spontaneous Emission from a Pair of Atoms. *Physical Review A* **2,** 889–896. ISSN: 0556-2791 (1970).
5. Lehmberg, R. H. Radiation from an N -Atom System. I. General Formalism. *Physical Review A* **2,** 883–888. ISSN: 0556-2791 (1970).

4.1. Dipole-Dipole Interaction

When multiple atoms in close proximity interact with a light-field, the theoretical description has to explicitly take effects into account where radiation emitted by one atom influences the other atoms. Equivalently to the single atom case, a master equation can be obtained where the light fields are treated as bath for the atomic system. The derivation of this master equation was originally done by Lehmberg [1, 2] and can be found in many quantum optics books, i.e. in [3]. In the end, it turns out that the inclusion of the light fields results in an effective interaction between the atoms, the so called Dipole-Dipole interaction, and additionally modifies the decaying processes. Photons are then emitted collectively by several atoms together leading to, depending on the spatial distribution of the atoms, either an increased or a suppressed photon emission rate called superradiance and subradiance. In the following, a sketch of the derivation of these effects is presented, roughly following the guidance of Gardiner and Zoller's book "Quantum World" [3].

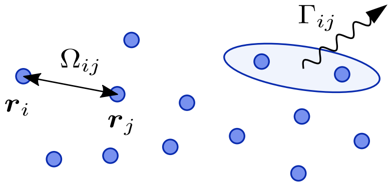

Figure 4.1.: System consisting of multiple atoms in close proximity interacting via the free space light fields. Eliminating the fields leads to an effective dipole-dipole force between the particles and to collective decay resulting in super or subradiance.

4.1.1. Derivation

The system under consideration consists of the particles and the light fields and is characterized by the Hamiltonian H_{tot} which can be separated into three parts,

$$H_{\text{tot}} = H_{\text{sys}} + H_{\text{int}} + H_{\text{field}}, \tag{4.1.1}$$

the particles, the interaction and the field Hamiltonian. The particles are modeled as two level systems with transition frequency ω_0 where all other levels only appear implicitly as Stark shifts in these two levels.

$$H_{\text{sys}} = \sum_i \hbar\omega_a \sigma_i^z \tag{4.1.2}$$

For the electro-magnetic field we exclusively allow frequencies in a certain range around ω_0 defined by $\|\omega_k - \omega_0\| < \delta$.

$$H_{\text{field}} = \sum_{\substack{k \\ \|\omega_k - \omega_0\| < \delta}} \hbar\omega_k b_k^\dagger b_k \tag{4.1.3}$$

The atom-light interaction is obtained using the electric dipole approximation and rotating wave approximation which leads to

$$H_{\text{Int}} = i\hbar \sum_{\substack{k,j \\ \|\omega_k - \omega_0\| < \delta}} \Big(\kappa_k^*(\vec{x}_j) b_k^\dagger \sigma_j^- - \kappa_k(\vec{x}_j) b_k \sigma_j^+\Big), \tag{4.1.4}$$

where the sum over $k = (\lambda, \vec{k})$ is a summation over all k-vectors as well as the two different possible polarizations. As can be seen in [4] the coupling strength is given by

$$\kappa_k(\vec{x}) = -\sqrt{\frac{\omega}{2\hbar\epsilon_0}} \vec{d}_{eg}.\vec{u}_k(\vec{x}) \tag{4.1.5}$$

with planar wave functions

$$\vec{u}_k(x) = \frac{1}{V} \vec{e}^{(\lambda)} e^{i\vec{k}.\vec{x}}. \tag{4.1.6}$$

In the interaction picture with respect to $H = H_{\text{sys}} + H_{\text{field}}$ the interaction Hamiltonian takes on the form

$$\begin{aligned} \tilde{H}_{\text{Int}} &= i\hbar \sum_{\substack{k,j \\ \|\omega_k - \omega_0\| < \delta}} \Big(\kappa_k^*(\vec{x}_j) e^{i(\omega_k - \omega_a)t} b_k^\dagger \sigma_j^- - \kappa_k(\vec{x}_j) e^{-i(\omega_k - \omega_a)t} b_k \sigma_j^+\Big) \\ &\equiv i\hbar \sum_j \Big(f_j^\dagger(t)\sigma_j^- - \sigma_j^+ f_j(t)\Big) \end{aligned} \tag{4.1.7}$$

where we introduced the noise operators

$$f_j(t) = \sum_{\substack{k \\ \|\omega_k - \omega_0\| < \delta}} \kappa_k(\vec{x}_j) e^{-i(\omega_k - \omega_a)t} b_k \tag{4.1.8}$$

which obey the commutation relation

$$\big[f_i(t), f_j^\dagger(t')\big] = \gamma_{ij}(t - t') = \sum_{\substack{k \\ \|\omega_k - \omega_0\| < \delta}} \kappa_k(\vec{x}_i)\kappa_k^*(\vec{x}_j) e^{-i(\omega_k - \omega_a)(t - t')}. \tag{4.1.9}$$

The Schroedinger equation of this system in the interaction picture,

$$i\hbar \frac{\mathrm{d}}{\mathrm{dt}} |\Psi(t)\rangle = \tilde{H}_{\text{Int}}(t)|\Psi(t)\rangle \tag{4.1.10}$$

can be formally solved by using a Dyson series. Defining the propagation operator $U(t,t_0)$ as $\Psi(t) = U(t,t_0)\Psi(t_0)$ allows us to rewrite the Schroedinger equation as

$$i\frac{\mathrm{d}}{\mathrm{dt}}U(t,t_0)|\Psi(t_0)\rangle = \frac{1}{\hbar}\tilde{H}_{\mathrm{Int}}(t)U(t,t_0)|\Psi(t_0)\rangle \tag{4.1.11}$$

and consequently

$$\begin{aligned} U(t,t_0) &= 1 - i\int_{t_0}^{t} dt_1 \frac{1}{\hbar}\tilde{H}_{\mathrm{Int}}(t_1)U(t_1,t_0) \\ &= 1 - i\int_{t_0}^{t} dt_1 \frac{1}{\hbar}\tilde{H}_{\mathrm{Int}}(t_1)\Big(1 - i\int_{t_0}^{t_1} dt_2 \frac{1}{\hbar}\tilde{H}_{\mathrm{Int}}(t_2)U(t_2,t_0)\Big) \\ &= 1 - i\frac{1}{\hbar}\int_{t_0}^{t} dt_1 \tilde{H}_{\mathrm{Int}}(t_1) - \frac{1}{\hbar^2}\int_{t_0}^{t} dt_1 \tilde{H}_{\mathrm{Int}}(t_1)\int_{t_0}^{t_1} dt_2 \tilde{H}_{\mathrm{Int}}(t_2)U(t_2,t_0) \end{aligned} \tag{4.1.12}$$

which gives the formal exact solution

$$\begin{aligned} |\Psi(t)\rangle &= \Big(1 - i\frac{1}{\hbar}\int_{t_0}^{t} dt_1 \tilde{H}_{\mathrm{Int}}(t_1)\Big)|\Psi(t_0)\rangle \\ &\quad - \frac{1}{\hbar^2}\int_{t_0}^{t} dt_1 \tilde{H}_{\mathrm{Int}}(t_1)\int_{t_0}^{t_1} dt_2 \tilde{H}_{\mathrm{Int}}(t_2)|\Psi(t_2)\rangle \\ &= \Big(1 + \int_{t_0}^{t} dt_1 \sum_j \Big(f_j^\dagger(t_1)\sigma_j^- - \sigma_j^+ f_j(t_1)\Big)\Big)|\Psi(t_0)\rangle \\ &\quad + \int_{t_0}^{t} dt_1 \sum_i \Big(f_i^\dagger(t_1)\sigma_i^- - \sigma_i^+ f_i(t_1)\Big) \\ &\qquad \int_{t_0}^{t_1} dt_2 \sum_j \Big(f_j^\dagger(t_2)\sigma_j^- - \sigma_j^+ f_j(t_2)\Big)|\Psi(t_2)\rangle. \end{aligned} \tag{4.1.13}$$

Using the assumption that the interaction is weak enough so that for a chosen time interval Δt the field is not changed significantly, which is called the Born approximation, allows us to substitute $|\Psi(t_2)\rangle$ with $|\Psi(t_0)\rangle$. In the following we assume that the field is initially in the vacuum state which simplifies 4.1.13 to

$$\begin{aligned} |\Psi(\Delta t)\rangle &= \Big(1 + \int_{t_0}^{\Delta t} dt_1 \sum_j \Big(f_j^\dagger(t_1)\sigma_j^- - \sigma_j^+ f_j(t_1)\Big)\Big)|\Psi(t_0)\rangle \\ &\quad + \int_{t_0}^{\Delta t} dt_1 \int_{t_0}^{t_1} dt_2 \sum_{ij} \Big(\sigma_i^-\sigma_j^- f_i^\dagger(t_1)f_j^\dagger(t_2) - \sigma_i^+\sigma_j^- f_i(t_1)f_j^\dagger(t_2)\Big)|\Psi(t_0)\rangle. \end{aligned} \tag{4.1.14}$$

The commutation relation 4.1.9 implies that

$$f_i(t_1)f_j^\dagger(t_2)|\Psi(t_0)\rangle = \Big(f_j^\dagger(t_2)f_i(t_1) + \gamma_{ij}(t_1 - t_2)\Big)|\Psi(t_0)\rangle = \gamma_{ij}(t_1 - t_2)|\Psi(t_0)\rangle \tag{4.1.15}$$

which finally allows us to rewrite 4.1.13 as

$$\begin{aligned}|\Psi(\Delta t)\rangle = \Big(1 - \sum_{ij} \sigma_i^+ \sigma_j^- \int_{t_0}^{\Delta t} dt_1 \int_{t_0}^{t_1} dt_2 \gamma_{ij}(t_1 - t_2)\Big)|\Psi(t_0)\rangle \\ + \sum_j \sigma_j^- \int_{t_0}^{\Delta t} dt_1 f_j^\dagger(t_1)|\Psi(t_0)\rangle \\ + \sum_{ij} \sigma_i^- \sigma_j^- \int_{t_0}^{\Delta t} dt_1 \int_{t_0}^{t_1} dt_2 f_i^\dagger(t_1) f_j^\dagger(t_2)|\Psi(t_0)\rangle. \qquad (4.1.16)\end{aligned}$$

Using these results to derive a quantum stochastic calculus shows that all physical parameters necessary to describe the system are contained in the γ_{ij} term which we will identify as collective decay rates Γ_{ij} and collective dipole-dipole shifts $\delta\omega_{ij}$ connected by

$$\int_0^{\Delta t} dt_1 \int_0^{t_1} dt_2 \gamma_{ij}(t_1 - t_2) \equiv (\frac{1}{2}\Gamma_{ij} + i\delta\omega_{ij})\Delta t. \qquad (4.1.17)$$

Starting by performing the polarization summation occurring in $\gamma_{ij}(t - t')$,

$$\begin{aligned}\gamma_{ij}(\tau) &= \sum_{\substack{k \\ \|\omega_k - \omega_0\| < \delta}} \kappa_k(\vec{x}_i)\kappa_k^*(\vec{x}_j) e^{-i(\omega_k - \omega_a)\tau} \\ &= \sum_{\vec{k}} \frac{\omega}{2\hbar\epsilon_0 V} \big(|\vec{d}_{eg}.\vec{e}^{(1)}|^2 + |\vec{d}_{eg}.\vec{e}^{(2)}|^2\big) e^{-i(\omega_k - \omega_a)\tau + i\vec{k}.(\vec{x}_i - \vec{x}_j)}, \qquad (4.1.18)\end{aligned}$$

which can by using the relation

$$\begin{aligned}|\vec{d}_{eg}.\vec{e}^{(k)}|^2 = |\vec{d}_{eg}.\big(\vec{e}^{(1)} \times \vec{e}^{(2)}\big)|^2 = \det(\begin{pmatrix}\vec{d}_{eg} \\ \vec{e}^{(1)} \\ \vec{e}^{(2)}\end{pmatrix} \cdot \begin{pmatrix}\vec{d}_{eg} & \vec{e}^{(1)} & \vec{e}^{(2)}\end{pmatrix}) \\ = \begin{vmatrix} |\vec{d}_{eg}|^2 & \vec{d}_{eg}.\vec{e}^{(1)} & \vec{d}_{eg}.\vec{e}^{(2)} \\ \vec{e}^{(1)}.\vec{d}_{eg} & 1 & 0 \\ \vec{e}^{(2)}.\vec{d}_{eg} & 0 & 1 \end{vmatrix} = |\vec{d}_{eg}|^2 - |\vec{d}_{eg}.\vec{e}^{(1)}|^2 - |\vec{d}_{eg}.\vec{e}^{(2)}|^2 \quad (4.1.19)\end{aligned}$$

rewritten into

$$\gamma_{ij}(\tau) = \sum_{\vec{k}} \frac{\omega}{2\hbar\epsilon_0 V} \big(|\vec{d}_{eg}|^2 - |\vec{d}_{eg}.\vec{e}^{(k)}|^2\big) e^{-i(\omega_k - \omega_a)\tau + i\vec{k}.(\vec{x}_i - \vec{x}_j)}. \qquad (4.1.20)$$

Taking the limit from discrete modes to a continuum of modes using the substitution

$$\frac{1}{V}\sum_{\vec{k}} \longrightarrow \frac{1}{(2\pi)^3}\int \mathrm{d}\vec{k} \longrightarrow \frac{1}{(2\pi c)^3}\int \omega^2 \mathrm{d}\omega \int \mathrm{d}\Omega_{\vec{k}} \qquad (4.1.21)$$

we obtain

$$\gamma_{ij}(\tau) = \frac{1}{2\hbar\epsilon_0(2\pi c)^3}\int \mathrm{d}\omega\omega^3 e^{-i(\omega-\omega_a)\tau}\int \mathrm{d}\Omega_{\vec{k}}\big(|\vec{d}_{eg}|^2 - |\vec{d}_{eg}.\vec{e}^{(k)}|^2\big)e^{i\vec{k}.(\vec{x}_i-\vec{x}_j)}. \tag{4.1.22}$$

The angular integral can be evaluated by writing the dipole part in terms of Legendre polynomials $P_0(x) = 1$ and $P_2(x) = \frac{1}{2}(3x^2 - 1)$,

$$\begin{aligned}|\vec{d}_{eg}|^2 - |\vec{d}_{eg}.\vec{e}^{(k)}|^2 &= \frac{2}{3}|\vec{d}_{eg}|^2(\frac{3}{2} - \frac{3}{2}|\vec{e}^{(\vec{d}_{eg})}.\vec{e}^{(k)}|^2)\\ &= \frac{2}{3}|\vec{d}_{eg}|^2\Big(1 - \frac{1}{2}(3|\vec{e}^{(\vec{d}_{eg})}.\vec{e}^{(k)}|^2 - 1)\Big)\\ &= \frac{2}{3}|\vec{d}_{eg}|^2(P_0(|\vec{e}^{(\vec{d}_{eg})}.\vec{e}^{(k)}) - P_2(|\vec{e}^{(\vec{d}_{eg})}.\vec{e}^{(k)})),\end{aligned} \tag{4.1.23}$$

expressing the exponential term as a plane wave expansion,

$$e^{iz\vec{e}^{(k)}.\vec{e}^{(r)}} = \sum_{l=0}^{\infty}(2l+1)i^l j_l(z)P_l(\vec{e}^{(k)}.\vec{e}^{(r)}) \tag{4.1.24}$$

where $\vec{r}_{ij} \equiv \vec{x}_i - \vec{x}_j$ and $z \equiv |\vec{k}||\vec{r}_{ij} = \omega|\vec{r}_{ij}|/c$ and using the integral identity

$$\int \mathrm{d}\Omega_{\vec{k}}P_l(\vec{e}^{(k)}.\vec{e}^{(r)})P_{l'}(\vec{e}^{(k)}.\vec{e}^{(d_{eg})}) = \frac{4\pi}{2l+1}\delta_{l,l'}P_l(\vec{e}^{(r)}.\vec{e}^{(d_{eg})}). \tag{4.1.25}$$

Combining all these relations allows us to solve the angular integral,

$$\begin{aligned}&\int \mathrm{d}\Omega_{\vec{k}}\big(|\vec{d}_{eg}|^2 - |\vec{d}_{eg}.\vec{e}^{(k)}|^2\big)e^{i\vec{k}.(\vec{x}_i-\vec{x}_j)}\\ &\quad= \frac{2}{3}|\vec{d}_{eg}|^2\int \mathrm{d}\Omega_{\vec{k}}\big(P_0(|\vec{e}^{(\vec{d}_{eg})}.\vec{e}^{(k)}) - P_2(|\vec{e}^{(\vec{d}_{eg})}.\vec{e}^{(k)})\big)\\ &\qquad\qquad \sum_{l=0}^{\infty}(2l+1)i^l j_l(z)P_l(\vec{e}^{(k)}.\vec{e}^{(r)})\\ &\quad= \frac{2}{3}|\vec{d}_{eg}|^2\sum_{l=0}^{\infty}(2l+1)i^l j_l(z)\\ &\qquad\qquad \int \mathrm{d}\Omega_{\vec{k}}\big(P_0(|\vec{e}^{(\vec{d}_{eg})}.\vec{e}^{(k)}) - P_2(|\vec{e}^{(\vec{d}_{eg})}.\vec{e}^{(k)})\big)P_l(\vec{e}^{(k)}.\vec{e}^{(r)})\\ &\quad= \frac{8\pi}{3}|\vec{d}_{eg}|^2\big(j_0(z) - j_2(z)P_2(\vec{e}^{(r)}.\vec{e}^{(d_{eg})})\big),\end{aligned} \tag{4.1.26}$$

and therefore the commutation relation is given by

$$\gamma_{ij}(\tau) = \frac{|\vec{d}_{eg}|^2}{6\hbar\epsilon_0\pi^2c^3}\int \mathrm{d}\omega\omega^3 e^{-i(\omega-\omega_a)\tau}\big(j_0(z) - j_2(z)P_2(\vec{e}^{(r)}.\vec{e}^{(d_{eg})})\big) \tag{4.1.27}$$

At this point we can perform the time integrals as stated in 4.1.16,

$$\int_0^{\Delta t} dt_1 \int_0^{t_1} dt_2 \gamma_{ij}(t_1-t_2) = \int \mathrm{d}\omega f(\omega) \int_0^{\Delta t} dt_1 \int_0^{t_1} dt_2 e^{-i(\omega-\omega_a)(t_1-t_2)}, \tag{4.1.28}$$

where

$$f(\omega) = \frac{|\vec{d}_{eg}|^2}{6\hbar\epsilon_0\pi^2 c^3}\omega^3\big(j_0(z) - j_2(z)P_2(\vec{e}^{(r)}.\vec{e}^{(d_{eg})})\big). \tag{4.1.29}$$

Using the integral identities

$$\begin{aligned}
\int_0^{t_1} \mathrm{d}t_2 e^{-i(\omega-\omega_0)(t_1-t_2)} &= \frac{1}{i(\omega-\omega_0)} - \frac{e^{-i(\omega-\omega_0)t_1}}{i(\omega-\omega_0)} \\
\int_0^{\Delta t} \mathrm{d}t_1 \frac{1}{i(\omega-\omega_0)} &= \frac{\Delta t}{i(\omega-\omega_0)} \\
\int_0^{\Delta t} \mathrm{d}t_1 \frac{e^{-i(\omega-\omega_0)t_1}}{i(\omega-\omega_0)} &= \frac{e^{-i(\omega-\omega_0)\Delta t}}{(\omega-\omega_0)^2} + \frac{1}{(\omega-\omega_0)^2} \\
\int_0^{\Delta t} \mathrm{d}t_1 \frac{1}{i(\omega-\omega_0)} + \frac{e^{-i(\omega-\omega_0)t_1}}{i(\omega-\omega_0)} &= \frac{2\sin^2(\frac{\omega-\omega_0}{2}\Delta t)}{(\omega-\omega_0)^2} \\
&\quad - i\Big(\frac{\Delta t}{\omega-\omega_0} - \frac{2\sin\big((\omega-\omega_0)\Delta t\big)}{(\omega-\omega_0)^2}\Big)
\end{aligned} \tag{4.1.30}$$

we are left with just one integral over ω,

$$\begin{aligned}
\int_0^{\Delta t} dt_1 \int_0^{t_1} dt_2 \gamma_{ij}(t_1-t_2) &= \int \mathrm{d}\omega f(\omega) \frac{2\sin^2(\frac{\omega-\omega_0}{2}\Delta t)}{(\omega-\omega_0)^2} \\
&\quad - i \int \mathrm{d}\omega f(\omega) \Big(\frac{\Delta t}{\omega-\omega_0} - \frac{2\sin\big((\omega-\omega_0)\Delta t\big)}{(\omega-\omega_0)^2}\Big) \\
&\equiv \big(\frac{1}{2}\Gamma_{ij} + i\delta\Omega_{ij}\big)\Delta t.
\end{aligned} \tag{4.1.31}$$

The real part of this function is straight forward to calculate since the sinc function can be interpreted as a δ function for the case $\delta\Delta t \ll 1$ and therefore

$$\Gamma_{ij} = \frac{|\vec{d}_{eg}|^2 k_a^3}{3\hbar\epsilon_0\pi}\big(j_0(k_a r) - j_2(k_a r)P_2(\vec{e}^{(r)}.\vec{e}^{(d_{eg})})\big) \tag{4.1.32}$$

where $k_a \equiv \frac{\omega_a}{c} \equiv \frac{2\pi}{\lambda_{eg}}$. For the case $r = 0$ we retrieve the single atom decay $\Gamma = \frac{|\vec{d}_{eg}|^2 k_a^3}{3\hbar\epsilon_0\pi}$ which can be used to write the formula more compactly as

$$\Gamma_{ij} = \Gamma\big(j_0(k_a r) - j_2(k_a r)P_2(\vec{e}^{(r)}.\vec{e}^{(d_{eg})})\big) \tag{4.1.33}$$

The second, purely imaginary term requires a more involved discussion which concludes with the expression

$$\delta\omega_{ij} = \frac{1}{2}\Gamma\big(n_0(k_a r) + n_2(k_a r)P_2(\vec{e}^{(r)}.\vec{e}^{(d_{eg})})\big) \tag{4.1.34}$$

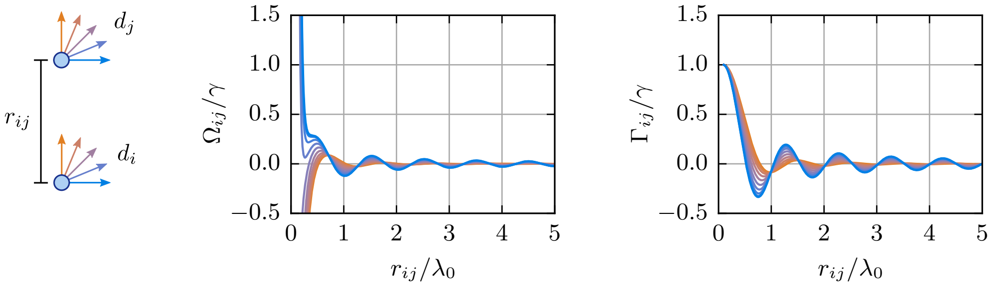

Figure 4.2.: Dipole-dipole interaction energy (left plot) and collective decay rate (right plot) for two atoms in distance r_{ij} and various relative dipole orientations. The dipole orientation in respect to the line connecting the two atoms is defined by the line colors and can be interpreted using the accordingly colored arrow diagram on the very left side.

where n are the spherical Neumann functions in physicists notation. Expressing the Bessel functions as well as the Neumann functions in the formulas for the spontaneous emission rates and the dipole-dipole shifts results in

$$\Gamma_{ij} = \frac{3}{2}\Gamma F_{ij}(k_a r_{ij}) \tag{4.1.35a}$$

$$\delta\omega_{ij} = \frac{3}{4}\Gamma G_{ij}(k_a r_{ij}) \tag{4.1.35b}$$

with the functions

$$F_{ij}(\xi) = \big(1 - (\vec{e}^{(r)}.\vec{e}^{(d_{eg})})^2\big)\frac{\sin\xi}{\xi} + \big(1 - 3(\vec{e}^{(r)}.\vec{e}^{(d_{eg})})^2\big)\Big(\frac{\cos\xi}{\xi^2} - \frac{\sin\xi}{\xi^3}\Big) \tag{4.1.36a}$$

$$G_{ij}(\xi) = -\big(1 - (\vec{e}^{(r)}.\vec{e}^{(d_{eg})})^2\big)\frac{\cos\xi}{\xi} + \big(1 - 3(\vec{e}^{(r)}.\vec{e}^{(d_{eg})})^2\big)\Big(\frac{\sin\xi}{\xi^2} - \frac{\cos\xi}{\xi^3}\Big). \tag{4.1.36b}$$

References

1. Lehmberg, R. H. Radiation from an N -Atom System. I. General Formalism. *Physical Review A* **2,** 883–888. ISSN: 0556-2791 (1970).
2. Lehmberg, R. H. Radiation from an N -Atom System. II. Spontaneous Emission from a Pair of Atoms. *Physical Review A* **2,** 889–896. ISSN: 0556-2791 (1970).
3. Gardiner, C. & Zoller, P. *The Quantum World of Ultra-Cold Atoms and Light Book II: The Physics of Quantum-Optical Devices (World Scientific)* en, 1–524. doi:`10.1142/9781783266784`. <`http://www.worldscientific.com/doi/abs/10.1142/9781783266784`> (IMPERIAL COLLEGE PRESS, 2015).

4. Gardiner, C. & Zoller, P. *The Quantum World of Ultra-Cold Atoms and Light Book 1: Foundations of Quantum Optics* ISBN: 978-1-78326-460-5. doi:`10.1142/p941`. <`http://www.worldscientific.com/worldscibooks/10.1142/p941`> (IMPERIAL COLLEGE PRESS, 2014).

4.2. Atomic clocks

4.2.1. A short history of time

The development of increasingly accurate time keeping devices is probably one of the biggest endeavors in the history of human kind. Propelled by changing and because of the increasingly demanding needs, huge efforts were undertaken that resulted in tremendous improvements. While in the beginning the interest in time often originated from religious reasons, the significance of clocks reached unknown heights with the desire for better navigation on sea, which was a necessity for the economical as well as military aspirations of the colonial powers. Despite the invention of sufficient accurate pendulum clocks in the 17th century it took nearly another 100 years until devices were build that were able to defy the harsh conditions on ships - the so called marine chronometers. Over centuries pendulum clocks were improved to their limit, resulting in the Shortt-Synchrotron clock [1] which was the pinnacle of classical clock making and only had an error of around one second every year [2]. For a long time, pendulum clocks stayed the undisputed winners in the race for accuracy. Only with the invention of Quartz clocks around 1920 a new contender for the title appeared. Beside the gain in accuracy also their smaller size and later on easier production made them the new standard time keeping device, which was also affordable for the general public. The latest breakthrough in technology was the development of atomic clocks, which use the transition frequency between atomic levels as their time keeping element. Although the first versions were inferior to the available quartz clocks [3], improvements were achieved at incredible rates so that nowadays state of the art optical lattice clocks only go wrong by one second after 10 billion years [4].

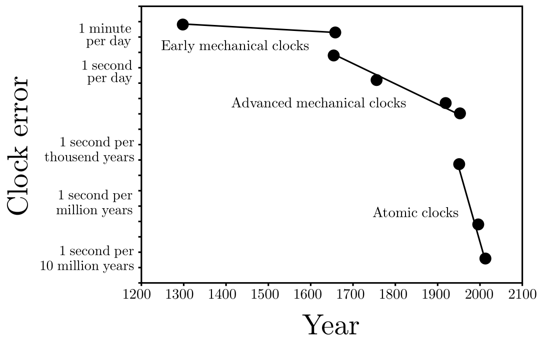

Figure 4.3.: Improvement of clocks over time.

4.2.2. Applications

With the construction of clocks that even after millions of years go wrong by less than one second an outside observer might raise the question if further advancement is necessary or just a meaningless undertaking of scientists, desperately looking for new challenges. Indisputably, the competition is an additional motivating factor, but the research is mainly fueled by the desire to reach new, untouched fields of physics. The success of modern theories which agree with the experimental results to astonishing accuracy requires increasingly more elaborate methods to even hope to measure deviations necessary to evolve our understanding of nature. One of the many paths for exploration is the possibility that fundamental constants are in defiance of their name not really constant but might vary over time and space. In the year 1937 Dirac presented a hypothesis, also called Dirac's large number hypothesis, where he speculated that the gravitational constant changes proportional to the inverse of the age of the universe [5]. Although this proposition didn't gain too much acceptance, it set a precedent to challenge the constancy of all quantities that were thus far regarded as constants.

The search for new physics beyond the standard model of particle physics led to theories that not ultimately require but at least consider changes of the fine structure constant causing a frantic search using a multitude of different experiments [6]. A promising candidate is based on comparison of atomic clocks which use distinct types of atoms [7].

Another example is the search for the existence of gravitational waves predicted by the theory of general relativity. Recent successful detection by the LIGO experiment [8] caused huge waves in the media arousing the interest of the public. While atomic clocks played only a minor role in this triumph other designs utilize them as main ingredients in order to raise the sensitivity and at the same time reducing the necessary dimensions [9] for gravitational wave sensors. This might also lead to development of ultra-sensitive gravimeters and gravity gradiometers.

In contrast to these mainly scientific interests devices along this line of investigation have considerable practical applications. Detectors based on atomic clocks can be used for precise measurements of the Earth's gravity field and will undoubtedly become the main instrument for Geodesy. Knowledge of the exact form of equipotential surfaces can be used to infer density variations and therefore assist with the search for valuable resources hidden in the depth of our planet. Relative time inaccuracies of 10^{-18}, already achievable by top of the art atomic lattice clocks enable detection of height differences of 1cm near the surface of the earth. This is for example sufficient to detect density anomalies of 20% over a sphere with a radius of 1.5km in the depth of 2km [10].

4.2.3. Characteristics of good clocks in general

Probably the most intuitive way to define a measure for the quality of a clock is by assessing the deviation of the clock from a perfect clock. Of course in absence of a perfect clock the only alternative is to compare various imperfect clocks with one another, preferably of different kind and use the gained information to estimate the inaccuracy. Assuming the error will grow linearly in time it makes sense to use the relative error

$$\sigma = \frac{\Delta T}{T} \tag{4.2.1}$$

as measure instead of bothering with specifying the deviation as function of time. In many cases this is an adequate assumption. but there are time keeping devices which have either a great short time accuracy but are worthless on the long run and vice versa.

All modern clocks like e.g. pendulum clocks, quartz clocks and atomic clocks rely on some kind of oscillatory phenomenon simply because they historically proved to be superior. For these kind of clocks the error in time can be directly related to a frequency error

$$\sigma = \frac{\Delta T}{T} = \frac{\Delta \omega}{\omega} \tag{4.2.2}$$

which can have various origins. It is clear that in order to use any physical system as clock one has to have complete knowledge of the physical theory describing it as well as complete experimental control of all of its properties. Not understanding the underlying theory but having great experimental mastery results in a precise yet inaccurate clock while the inverse situation will lead to an accurate but imprecise one. For the pendulum clock for example one has to be able to accurately determine the length, or to be more precise, the moment of inertia around the pivot point of its pendulum. Inadequate control over environmental influences like variations of temperature or humidity will cause changes that will result in a drifting frequency. Further on differences of the gravitational strength as well as damping will influence the ticking of the clock.

It turns out that this relation is closely connected to the Q-factor which is defined as the ratio between the initial energy of an oscillating system and the energy loss after one cycle:

$$Q = \frac{\text{Initial Energy}}{\text{Energy lost after one cycle}}. \tag{4.2.3}$$

While experimentally it shows that by comparing many different types of clocks that the Q-factor is a very good indicator for their accuracy [11], this result is in the case of pendulum clocks not immediately obvious. Including damping to the description of the pendulum,

$$\ddot{x} + \gamma \dot{x} + \omega_0^2 x, \qquad \omega_0^2 = \frac{g}{l} \tag{4.2.4}$$

just leads to a reduced but well defined oscillation frequency $\omega^2 = \omega_0^2 - \frac{1}{4}\gamma^2$ where of course the amplitude will damp out with $e^{-\frac{1}{2}\gamma t}$. For a real clock this energy loss has to be compensated using a driving force, which is done by, in the context of horology called, anchor escapements. Using a deadbeat escapement which in its perfect form applies delta impulses at times, where $x = 0$, it can be shown that this driving force results in a stable limit cycle with the same frequency as the damped pendulum without driving [12]. The influence of the Q-factor on the quality of the clock enters the picture in a more roundabout way, which can be understood by studying a damped harmonic oscillator driven by a frequency ω

$$\ddot{x} + 2\gamma\dot{x} + \omega_0^2 x = F_\omega \sin\omega t. \tag{4.2.5}$$

It has the steady state solution

$$x(t) = A\sin(\omega t + \phi) \tag{4.2.6}$$

with Amplitude A

$$A = \frac{F_\omega}{\sqrt{\gamma^2\omega^2 + (\omega_0^2 - \omega^2)^2}}. \tag{4.2.7}$$

For small damping, i.e. $\gamma \ll \omega_0$ and for driving frequencies close around the oscillator frequency ω_0 the formula for the amplitude simplifies to

$$A^2 = \frac{\frac{1}{4\omega_0^2}}{\frac{\gamma^2}{4} + (\omega - \omega_0)^2} \tag{4.2.8}$$

which is a Lorentzian function with width $\gamma/2$ around ω_0. For pendulum clocks this has immediate consequences. If through imperfections in the escapement mechanism additional frequencies are driven, a smaller friction leads to a smaller influence of these unwanted frequencies on the motion of the pendulum explaining the connection between Q-factor and quality of a pendulum clock.

4.2.4. Basic principles of optical atomic clocks

For atomic clocks, the connection between the Q-factor and the clock error is in some sense much easier to understand. The underlying principle is to tune a clock oscillator like a laser to a reference oscillator, i.e. an atomic transition, as seen in Fig. 4.4. This situation is completely equivalent to the periodically driven harmonic oscillator investigated in the previous section where the oscillator corresponds to the atomic transition and the harmonic driving is replaced by the laser. The measured signal, whatever that turns out to be, depends heavily on the difference between those two frequencies, following a Lorentzian curve. By adjusting the laser frequency to keep the signal as constant as possible, the laser is stabilized to the atomic transition frequency. It is clear that the narrower the resonance curve, which corresponds to small atomic decay, the more sensitive the signal reacts to frequency changes and the better the laser can be stabilized. For this to work the probing laser has to be highly spectrally pure to be able to resolve the atomic resonance. This might at first sound strange, since if the oscillator by itself already has an adequate quality, then why do we trouble ourself with atoms that are notoriously hard to control? The answer is two-fold. First, the frequency of the laser is determined by a length scale - the length of the cavity used to stabilize the laser, which is necessary to obtain such high precision in the first place. Due to our inability to

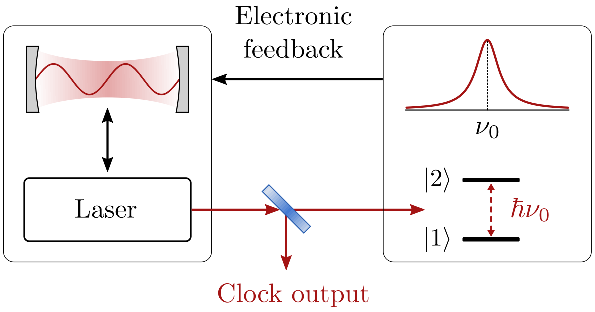

Figure 4.4.: Basic operating principle of a typical atomic clock. A laser is tuned to a narrow atomic transition.

produce cavities with a well enough defined length, every single exemplar of this type of clock, while admittedly having an exceptionally constant frequency, will show huge deviations compared to all other clocks. In other words, it would be a clock with high precision but low accuracy. Atoms provide in this regard a universal reference since their transition frequency is, hopefully, independent of space and time. The second point is that although these cavities are very stable on short time scales, on longer time scales, around 10 seconds, inevitable external influences lead to length changes in the cavity used to stabilize the laser and consequently to a frequency shift of the clock signal. Again atoms, unperturbed by such minor influences, circumvent this problem by providing an unwavering, steady reference frequency.

Despite the simplicity of the basic idea, experimentalists, confronted with the harsh influences of the real world, struggle to realize this concept. To appreciate the challenges that have to be overcome in the laboratory one has to examine all the interfering physical processes in greater detail.

Spectrally pure lasers – Fabricating a laser of the necessary quality is a difficult task [13]. Although lasers are commonly viewed as sources of incredibly coherent light they are still inadequate to resolve the narrow lines of atomic clock transitions. Utilizing an additional empty high-Q cavity, which isn't subjugated by the noise created by the laser's gain medium, accomplishes the required improvements. Essential is that the length of this empty cavity is as stable as possible which in practice is achieved by using a specialized highly rigid material that keeps the mirror distance constant [14]. Stabilizing the laser to this high-Q cavity is by itself a nontrivial endeavor needing the capability to swiftly adjust the laser frequency to compensate all noise processes.

Synchronization of the laser to the atomic transition – In order to determine the deviation of the clock laser from the atomic transition various kinds of spectroscopy are used. Most schemes are based on Rabi and Ramsey spectroscopy [15] but over the years many variations have been tried out [16, 17]. The underlying idea is always that the relative phase of the superposition of the ground and excited state of the clock transition, $|\Psi\rangle = |g\rangle + e^{i\phi}|e\rangle$, will exactly oscillate with the transition frequency, but only in the absence of disturbances. Due to the accurateness of modern atomic clocks, even smallest outside influences result in measurable errors, which on the one hand will be great for incredibly sensitive measurement devices, but in this context limits the clocks accuracy to an unacceptable extent. Therefore, each of the following effects has to be theoretically perfectly understood and experimentally controlled.

Doppler effect Movement of the atoms was for a long time the biggest source of error [18]. Even though some spectroscopy schemes circumvent at least the first order Doppler shift, imperfect application and the second order Doppler shift still make trapping and cooling of the atoms mandatory.

Magnetic fields - Zeeman effect Besides the inevitable magnetic fields imposed by the environment, static magnetic fields are often applied purposely in order to define a quantization axis. Either way, the atomic levels used for the clock transition have to be chosen carefully to avoid [19] or at least provide ways to correct the influence of magnetic fields [20].

Electric fields - Stark effect Clock transitions are usually chosen to eliminate the influence of static electric fields arising from potential differences in surrounding materials, at least in first order. Next order shifts can usually be calculated to acceptable precision [21]. In atomic clocks, which use trapped particles, the AC-Stark effect caused by the trapping laser induces gigantic shifts which have to be accounted for. However, for a carefully chosen trapping wavelength, a so called magic wavelength, both clock states are shifted by the same amount and the transition is unaffected. Another source of electric fields is the black body radiation [22] emitted by the surrounding containment demanding cooling of the vacuum chamber to reach highest possible clock accuracy.

Collisions Collisions of clock atoms with one another and collisions with background gas atoms are notoriously hard to calculate and can mostly only be estimated experimentally. For ions, which are well separated in the trap, this is a minor issue but in the case of neutral particles where usually several atoms are in a common location this can be substantial [23].

Dipole-dipole interaction Contrary to collisions, which occur only between particles in close proximity, the dipole-dipole interaction leads to interactions between well separated atoms. Albeit small for two single atoms the effect can accumulate and can, if enough particles are involved, make a non-negligible contribution.

The last point is the main focus of this part of the theses and will be investigated in great detail in the following chapters. For a much better and detailed introduction into the world of optical atomic clocks the reader is referred to the excellent review articles [24, 25].

References

1. Britten. *Britten's Watch & Clock Makers' Handbook Dictionary & Guide Fifteenth Edition* (Taylor & Francis).
2. Jones, A. *Splitting The Second: The Story of Atomic Time* 199. ISBN: 1-4200-3349-2 (CRC Press, 2000).
3. Sullivan, D. *Time and frequency measurement at NIST: the first 100 years* in *Proceedings of the 2001 IEEE International Frequncy Control Symposium and PDA Exhibition (Cat. No.01CH37218)* (IEEE, 2001), 4–17. ISBN: 0-7803-7028-7. doi:`10.1109/FREQ.2001.956152`.
4. Bloom, B. J. *et al.* An optical lattice clock with accuracy and stability at the 10(-18) level. *Nature* **506,** 71–5. ISSN: 1476-4687 (2014).
5. DIRAC, P. A. M. The Cosmological Constants. *Nature* **139,** 323–323. ISSN: 0028-0836 (1937).
6. Uzan, J. The fundamental constants and their variation: observational and theoretical status. *Reviews of modern physics* (2003).
7. Marion, H., Santos, F. D. & Abgrall, M. Search for variations of fundamental constants using atomic fountain clocks. *Physical review ...* (2003).
8. Abbott, B. P. & Al., E. Observation of Gravitational Waves from a Binary Black Hole Merger. *Physical Review Letters* **116,** 061102. ISSN: 0031-9007 (2016).
9. Graham, P. W., Hogan, J. M., Kasevich, M. A. & Rajendran, S. New Method for Gravitational Wave Detection with Atomic Sensors. *Physical Review Letters* **110,** 171102. ISSN: 0031-9007 (2013).
10. Bondarescu, R. *et al.* Geophysical applicability of atomic clocks: direct continental geoid mapping. *Geophysical Journal International* **191,** 78–82. ISSN: 0956540X (2012).
11. Bateman, D. Vibration theory and clocks. Part 3. Q and the practical performance of clocks. *Horological J* **120,** 48–55 (1977).
12. Denny, M. The pendulum clock: a venerable dynamical system. en. *European Journal of Physics* **23,** 449–458. ISSN: 01430807 (2002).
13. Salomon, C., Hils, D. & Hall, J. L. Laser stabilization at the millihertz level. EN. *Journal of the Optical Society of America B* **5,** 1576. ISSN: 0740-3224 (1988).

14. Young, B. C., Cruz, F. C., Itano, W. M. & Bergquist, J. C. Visible Lasers with Subhertz Linewidths. *Physical Review Letters* **82,** 3799–3802. ISSN: 0031-9007 (1999).
15. Ramsey, N. *Molecular Beams* ISBN: 0198520212 (1956).
16. Bordé, C. J. *et al.* Optical Ramsey fringes with traveling waves. *Physical Review A* **30,** 1836–1848. ISSN: 0556-2791 (1984).
17. Warren, W. S. Multiple phase-coherent laser pulses in optical spectroscopy. I. The technique and experimental applications. *The Journal of Chemical Physics* **78,** 2279. ISSN: 00219606 (1983).
18. Vanier, J. & Audoin, C. *The quantum physics of atomic frequency standards* 2nd ed. (CRC Press, 1989).
19. Bernard, J., Marmet, L. & Madej, A. A laser frequency lock referenced to a single trapped ion. *Optics Communications* **150,** 170–174. ISSN: 00304018 (1998).
20. Rosenband, T. *et al.* Observation of the 1S0–¿3P0 clock transition in 27Al+. *Physical review letters* **98,** 220801. ISSN: 0031-9007 (2007).
21. Lodewyck, J., Zawada, M., Lorini, L., Gurov, M. & Lemonde, P. Observation and cancellation of a perturbing dc stark shift in strontium optical lattice clocks. *IEEE transactions on ultrasonics, ferroelectrics, and frequency control* **59,** 411–5. ISSN: 1525-8955 (2012).
22. Farley, J. W. & Wing, W. H. Accurate calculation of dynamic Stark shifts and depopulation rates of Rydberg energy levels induced by blackbody radiation. Hydrogen, helium, and alkali-metal atoms. *Physical Review A* **23,** 2397–2424. ISSN: 0556-2791 (1981).
23. Akatsuka, T., Takamoto, M. & Katori, H. Optical lattice clocks with non-interacting bosons and fermions. *Nature Physics* **4,** 954–959. ISSN: 1745-2473 (2008).
24. Poli, N., Oates, C. W., Gill, P. & Tino, G. M. Optical atomic clocks, 69 (2014).
25. Ludlow, A. D., Boyd, M. M., Ye, J., Peik, E. & Schmidt, P. O. Optical atomic clocks. *Reviews of Modern Physics* **87,** 637–701. ISSN: 0034-6861 (2015).

4.3. Superradiant laser

As was presented in the chapter about atomic clocks, the short term accuracy and the narrow bandwidth of the clock signal originate from a laser which is stabilized to an empty high-Q optical cavity. Synchronization to the atomic transition is in principle only necessary as universal reference and to compensate long-term instabilities due to changes of the cavity length. The precision of the atomic clock is therefore, among other things, limited by the quality of the cavity. State of the art ultra-stable optical cavities achieve incredible small linewidths of less than 1 Hz. However, atomic transitions utilized in the newest atomic clocks have a natural line Q of order 10^{18} even surpassing the fractional instabilities of these cavities by a factor 100 [1]. Further improvement is hindered by thermal noise [2] of the cavity mirrors, which is notoriously difficult to remove [3].

An alluring alternative approach would be to use the naturally narrow linewidths of the atoms directly and thereby avoiding the necessity to fight these technical difficulties. However, due to the long lived nature of the clock transition and the relatively small achievable particle numbers in the order of 10^6 the emitted fluorescent light is too weak for any practical applications. Using the effect of superradiance [4], that is the fact that in an ensemble of directly or indirectly interacting dipoles the light emitted per particle can be much higher than for a single dipole, can enhance the output power to sufficient magnitudes [1]. Of course, this effect is worthless if the increased emission rate is accompanied by a simultaneous increase of the linewidth of the outgoing light. However, it turns out that utilizing this effect in various different superradiant laser setups can leave the coherence approximately unchanged or even improve it by surprisingly large factors [5–7]. All of these systems have in common that they operate in the bad cavity regime, i.e. that the cavity loss is much larger than the atomic decay rate. This leads to relatively small photon numbers, in some cases of even less than one photon, inside the cavity. The excitations are contrary to a common laser not stored in the cavity field but in the dipoles which use the cavity mode more or less only to couple their dynamics. Similarly to the classical situation, already observed by Huygens in the 17th century [8] where clocks mounted on the same wall will interact via vibrations and adjust to a common frequency, the dipoles in the cavity communicate with help of the cavity mode and, if the right conditions are met, start to synchronize their oscillations. This simple picture already gives a great intuitive explanation of the ongoing physics which also can be quantified in a more rigorous manner.

The first model of a superradiant laser was discussed in a publication by Fritz Haake and Mikhail Kolobov in 1993 [5], who investigate the case of many particles in close proximity, which are modeled by a three level scheme (see Fig. 4.5a). The ensuing collective decay leads to astonishing properties for this system. For N particles inside the cavity they predict that the intensity increases with N^2 compared to the classical laser setup which only raises proportional to N, while at the same time the resulting linewidth of the superradiant laser improves from being

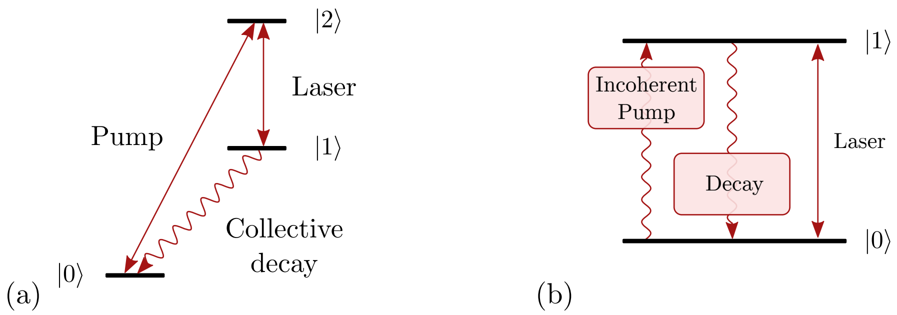

Figure 4.5.: (a) Three level superradiant laser model investigated in [5]. Superradiant decay from level $|1\rangle$ to $|0\rangle$ leads to synchronization effects and therefore a higher laser intensity as well as decreased laser linewidth. (b) Common two level laser model but calculated in the bad cavity regime. The artificially introduced incoherent pump stemming from eliminating the in praxis necessary third level has to be higher than the spontaneous decay rate of the transition. Superradiance is introduced implicitly via the cavity mode.

independent of the particle number to a $1/N$ scaling.

A resembling approach discussed by D. Meiser, Jun Ye, D. R. Carlson and M. J. Holland in [1] considers the effect of superradiance induced by the cavity mode in the common two-level laser model shown in Fig. 4.5b. In this case the required strong particle-particle interaction is not achieved directly by the closeness of the atoms but is mediated by the more or less infinitely ranged photon interaction inside of the cavity. They estimate that also in this model, for realistic experimental parameters, the resulting linewidth can be even smaller than the single atom linewidth of the clock transition. Using techniques from the atomic lattice clocks, this setup provides much better control over the error sources that are present in the system, which were discussed in the previous chapter, especially noteworthy in the context of this thesis, the dipole-dipole interaction.

References

1. Meiser, D., Ye, J., Carlson, D. R. & Holland, M. J. Prospects for a millihertz-linewidth laser. *Physical review letters* **102,** 163601. ISSN: 0031-9007 (2009).
2. Ludlow, A. D. *et al.* Compact, thermal-noise-limited optical cavity for diode laser stabilization at 10^{-15}. EN. *Optics Letters* **32,** 641. ISSN: 0146-9592 (2007).
3. Kimble, H. J., Lev, B. L. & Ye, J. Optical interferometers with reduced sensitivity to thermal noise. *Physical review letters* **101,** 260602. ISSN: 0031-9007 (2008).

4. Dicke, R. H. Coherence in Spontaneous Radiation Processes. *Physical Review* **93,** 99–110. ISSN: 0031-899X (1954).
5. Haake, F., Kolobov, M., Fabre, C., Giacobino, E. & Reynaud, S. Superradiant laser. *Physical review letters* **71,** 995–998. ISSN: 1079-7114 (1993).
6. Bohnet, J. G. *et al.* A steady-state superradiant laser with less than one intracavity photon. *Nature* **484,** 78–81. ISSN: 1476-4687 (2012).
7. Norcia, M. A., Winchester, M. N., Cline, J. R. K. & Thompson, J. K. Superradiance on the milliHertz linewidth strontium clock transition, 6 (2016).
8. Oliveira, H. M. & Melo, L. V. Huygens synchronization of two clocks. en. *Scientific reports* **5,** 11548. ISSN: 2045-2322 (2015).

5. Publication: A superradiant clock laser on a magic wavelength optical lattice

A superradiant clock laser on a magic wavelength optical lattice

Thomas Maier, Sebastian Kraemer,
Laurin Ostermann and Helmut Ritsch
Institute for Theoretical Physics, University of Innsbruck
Technikerstrasse 25/2, A-6020 Innsbruck, Austria
laurin.ostermann@uibk.ac.at

Abstract: An ideal superradiant laser on an optical clock transition of noninteracting cold atoms is predicted to exhibit an extreme frequency stability and accuracy far below mHz-linewidth. In any concrete setup sufficiently many atoms have to be confined and pumped within a finite cavity mode volume. Using a magic wavelength lattice minimizes light shifts and allows for almost uniform coupling to the cavity mode. Nevertheless, the atoms are subject to dipole-dipole interaction and collective spontaneous decay which compromises the ultimate frequency stability. In the high density limit the Dicke superradiant linewidth enhancement will broaden the laser line and nearest neighbor couplings will induce shifts and fluctuations of the laser frequency. We estimate the magnitude and scaling of these effects by direct numerical simulations of few atom systems for different geometries and densities. For Strontium in a regularly filled magic wavelength configuration atomic interactions induce small laser frequency shifts only and collective spontaneous emission weakly broadens the laser. These interactions generally enhance the laser sensitivity to cavity length fluctuations but for optimally chosen operating conditions can lead to an improved synchronization of the atomic dipoles.

OCIS codes: (270.0270) Quantum Optics, (140.6630) Superradiance and superfluorescence, (020.7010) Laser trapping

---

References and links

1. T. Kessler, C. Hagemann, C. Grebing, T. Legero, U. Sterr, F. Riehle, M. Martin, L. Chen, and J. Ye, “A sub-40-mHz-linewidth laser based on a silicon single-crystal optical cavity,” Nature Photonics **6**, 687–692 (2012).
2. D. Meiser, J. Ye, D. Carlson, and M. Holland, “Prospects for a millihertz-linewidth laser,” Physical review letters **102**, 163601 (2009).
3. J. Bohnet, Z. Chen, J. Weiner, D. Meiser, M. Holland, and J. Thompson, “A steady-state superradiant laser with less than one intracavity photon,” Nature **484**, 78–81 (2012).
4. J. G. Bohnet, Z. Chen, J. M. Weiner, K. C. Cox, and J. K. Thompson, “Active and passive sensing of collective atomic coherence in a superradiant laser,” Physical Review A **88**, 013826 (2013).
5. V. Vuletic, “Atomic physics: An almost lightless laser,” Nature **484**, 43–44 (2012).
6. M. Xu, D. Tieri, and M. Holland, “Simulating Open Quantum Systems using the Simple Lie Group SU (4),” arXiv preprint arXiv:1302.6284 (2013).
7. K. Henschel, J. Majer, J. Schmiedmayer, and H. Ritsch, “Cavity QED with an ultracold ensemble on a chip: Prospects for strong magnetic coupling at finite temperatures,” Physical Review A **82**, 033810 (2010).
8. F. Haake, M. I. Kolobov, C. Fabre, E. Giacobino, and S. Reynaud, “Superradiant laser,” Physical review letters **71**, 995 (1993).
9. P. Horak, K. Gheri, and H. Ritsch, “Quantum dynamics of a single-atom cascade laser,” Physical Review A **51**, 3257 (1995).

10. M. D. Swallows, M. Bishof, Y. Lin, S. Blatt, M. J. Martin, A. M. Rey, and J. Ye, “Suppression of collisional shifts in a strongly interacting lattice clock,” science **331**, 1043–1046 (2011).
11. M. Gross and S. Haroche, “Superradiance: An essay on the theory of collective spontaneous emission,” Physics Reports **93**, 301–396 (1982).
12. R. Bonifacio, P. Schwendimann, and F. Haake, “Quantum statistical theory of superradiance. I,” Physical Review A **4**, 302 (1971).
13. N. E. Rehler and J. H. Eberly, “Superradiance,” Phys. Rev. A **3**, 1735–1751 (1971).
14. H. Zoubi, “Collective light emission of a finite-size atomic chain,” EPL (Europhysics Letters) **100**, 24002 (2012).
15. J. MacGillivray and M. Feld, “Theory of superradiance in an extended, optically thick medium,” Physical Review A **14**, 1169 (1976).
16. L. Ostermann, H. Zoubi, and H. Ritsch, “Cascaded collective decay in regular arrays of cold trapped atoms,” Opt. Express **20** (2012).
17. N. Skribanowitz, I. P. Herman, J. C. MacGillivray, and M. S. Feld, “Observation of Dicke Superradiance in Optically Pumped HF Gas,” Phys. Rev. Lett. **30**, 309–312 (1973).
18. S. Inouye, A. Chikkatur, D. Stamper-Kurn, J. Stenger, D. Pritchard, and W. Ketterle, “Superradiant Rayleigh scattering from a Bose-Einstein condensate,” Science **285**, 571–574 (1999).
19. M. Moore and P. Meystre, “Theory of superradiant scattering of laser light from Bose-Einstein condensates,” Physical Review Letters **83**, 5202–5205 (1999).
20. M. Takamoto, F. Hong, R. Higashi, and H. Katori, “An optical lattice clock,” Nature **435**, 321–324 (2005).
21. L. Casperson, “Spectral narrowing in double-pass superradiant lasers,” Optics Communications **8**, 85–87 (1973).
22. R. Lehmberg, “Radiation from an N-atom system. I. General formalism,” Physical Review A **2**, 883 (1970).
23. Z. Ficek, R. Tanaś, and S. Kielich, “Quantum beats and superradiant effects in the spontaneous emission from two nonidentical atoms,” Physica A: Statistical Mechanics and its Applications **146**, 452–482 (1987).
24. Z. Ficek and R. Tanaś, “Entangled states and collective nonclassical effects in two-atom systems,” Physics Reports **372**, 369–443 (2002).
25. P. Meystre and M. Sargent, *Elements of Quantum Optics* (Springer-Verlag, 1990).
26. R. H. Dicke, “Coherence in Spontaneous Radiation Processes,” Phys. Rev. **93**, 99–110 (1954).
27. G. Campbell, A. Ludlow, S. Blatt, J. Thomsen, M. Martin, M. de Miranda, T. Zelevinsky, M. Boyd, J. Ye, S. Diddams *et al.*, “The absolute frequency of the 87Sr optical clock transition,” Metrologia **45**, 539 (2008).
28. B. Bloom, T. Nicholson, J. Williams, S. Campbell, M. Bishof, X. Zhang, W. Zhang, S. Bromley, and J. Ye, “An optical lattice clock with accuracy and stability at the 10-18 level,” Nature (2014).

1. Introduction

An essential and characteristic property of laser light, observed since its first generation, is its extraordinary coherence and frequency stability well below the width of the optical resonator used. Far above threshold the linewidth is limited by technical noise of the gain medium and the mirrors only. Continuous technological advances have brought this limit down to an incredible stability below the Hz-level [1], which competes against the Q and the linewidth of long lived atomic clock states. At this point, further technological improvements seem extremely challenging. Therefore, it has been suggested recently [2] and to some extent demonstrated experimentally [3, 4] that an atomic clock transition could be used as a narrow band gain medium to run a laser. Due to the very feeble individual dipole moments of the atoms such a device can only be operated in the strong collective coupling regime, where superradiant emission into the field mode provides for the necessary gain [5]. In this domain of operation a huge collective dipole constituted by a large number of atoms, which are synchronized via their common coupling to the cavity field [6, 7], will build up.

The general idea of superradiant lasers and their properties have been discussed already two decades ago [8, 9], where a unique frequency stability scaling with the inverse square of the atom number N and squeezed output light was predicted. Their superb accuracy in the regime of a cavity linewidth much larger than the atomic linewidth were highlighted just recently [3]. Most importantly, in this case the laser becomes very insensitive to technical noise in the resonator and its properties are dominated by the intrinsic stability of the collective atomic dipole. Under favorable conditions, with only a few photons and millions of atoms present, a natural width of the system several orders of magnitude below the 1 Hz-level could be envisaged.

A central, yet open technical problem here is the implementation of a uniform collective coupling of the atoms to the field mode as well as the optical pumping in the atomic system without a considerable perturbation of the lasing levels, which in this case include the atomic ground state. Thus, a very careful choice of operating parameters is required. Here, we study another intrinsic source of perturbation in this sensitive system, namely direct dipole-dipole interaction between the laser active atoms, as they are densely confined within the optical resonator. Similar to atom-atom collisions in Ramsey experiments [10], dipole-dipole couplings tend to induce phase noise and decoherence of the collective atomic dipole. In particular in lattice setups at low filling, where collisions are strongly suppressed, this should constitute the most prominent source of noise for such a laser.

The basic phenomenon of superradiance was theoretically studied in detail, e.g. by Haroche and coworkers [11], about 50 years ago using a variety of analytical approximation methods [12, 13]. As an important effect one finds that the decay rate of low energy collective excitations grows linearly with the particle number N [14]. For multiply excited states the effect is increased further and the collective decay of a strongly inverted ensemble exhibits a delayed intensity maximum largely proportional to N^2 as a significant deviation from the exponential decay of individual atoms [15, 11, 16]. The phenomenon has been observed in a large number of experiments in gases and solids [17, 15] and more recently also for ultracold quantum gases [18, 19].

As in every laser setup, we naturally have to deal with inverted ensembles. Hence, we can expect that superradiant effects will play an important role and the assumption of individual atomic decay at the independent free space single atom rate will loose its validity. Let us emphasize that the collective symmetric coupling of the atoms to the cavity mode does not require the atoms to occupy a small volume of the order of a cubic wavelength, but simply calls for an almost equal cavity coupling constant for all atoms. Dicke superradiant spontaneous decay, on the other hand, is maximal for closely spaced emitters, but still plays a decisive role in more extended geometries and in particular for regularly ordered ensembles. While this free space superradiant interaction and decay was incorporated intrinsically in the early works on superradiant lasing [8], it was neglected in the more recent considerations on superradiant lasing on ultra narrow atomic transitions [2].

In the present paper we investigate the full model for the collective decay process in a superradiant laser configuration. While the underlying Hamiltonian and dynamical master equations for the coupled atom-field dynamics are well established, exact treatments of the full decay problem for more than a few particles is hardly possible apart from some special cases. Numerical simulations can be performed for somewhat higher atom numbers in the fully collective limit. However, for more particles in a small but finite volume, collective and individual decay are present and the equations immediately become very cumbersome, as the number of occupied states within the total physical Hilbert space (growing as 2^N) gets prohibitively large. Interesting results can still be obtained for special finite configurations, which should exhibit the qualitative consequences of dipole-dipole coupling quite well. Besides demonstrating the underlying basic physical mechanisms, our study aims at direct implications for the laser linewidth of a magic wavelength lattice laser in the superradiant regime [20, 21, 3, 7].

2. Model

We consider N identical two-level atoms held in a regular spaced configuration, e.g. in a far detuned optical trap, each of them symmetrically coupled to a single mode of a high Q optical resonator. Due to the inherent exposure of the atoms to the vacuum bath the ensemble is affected by coherent dipole-dipole energy exchange processes and also by collective spontaneous emission [22]. Further, we employ a transverse incoherent pump, which allows us to use the atoms as an active medium, as well as another dissipative process, the cavity loss. Upon Born,

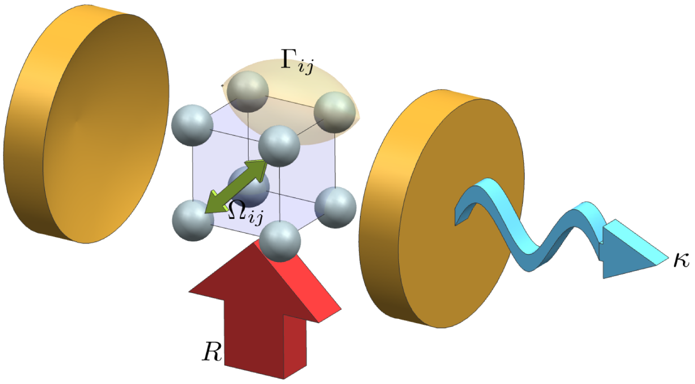

Fig. 1: Schematics of a lattice laser setup. A transversely pumped (pumping rate R) finite atomic ensemble with dipole-dipole couplings Ω_{ij} and collective spontaneous emission Γ_{ij} inside an optical resonator with a loss rate of κ

rotating wave and Markov approximation we end up with a standard Lindblad type master equation. Explicitly the time-dependence of the N-atom density matrix is governed by ($\hbar = 1$)

$$\frac{\partial \rho}{\partial t} = i\left[\rho, H\right] + \mathscr{L}_{\mathrm{cd}}\left[\rho\right] + \mathscr{L}_{\mathrm{pump}}\left[\rho\right] + \mathscr{L}_{\mathrm{cav}}\left[\rho\right] = \mathscr{L}\left[\rho\right], \tag{1}$$

with the Hamiltonian

$$H = \frac{\omega_0}{2}\sum_i \sigma_i^z + \sum_{i\neq j}\Omega_{ij}\,\sigma_i^+\sigma_j^- + \omega_c\, a^\dagger a + H_{\mathrm{int}}, \tag{2}$$

where σ_i^+ and σ_i^- are the raising and lowering operators for the atomic dipole of the i-th atom with the transition energy ω_0, the operators $a^\dagger$ and a correspond to the creation and annihilation of a photon with the frequency ω_c in the cavity mode , Ω_{ij} denotes the resonant dipole-dipole energy transfer between the atoms i and j, and

$$H_{\mathrm{int}} = g\sum_i\left(a\sigma_i^+ + a^\dagger\sigma_i^-\right) \tag{3}$$

represents the Jaynes-Cummings type interaction between the individual atomic transition dipoles and the cavity mode with g being the coupling that emerges if a constant mode function is assumed. This approximation is justified in the situation where the atomic ensemble is aligned transversely to the propagation direction of the cavity mode or its dimensions are much smaller than the length of the resonator.

The collective atomic damping is accounted for by the Liouvillian

$$\mathscr{L}_{\mathrm{cd}}\left[\rho\right] = \frac{1}{2}\sum_{i,j}\Gamma_{ij}\left(2\sigma_i^-\rho\sigma_j^+ - \sigma_i^+\sigma_j^-\rho - \rho\sigma_i^+\sigma_j^-\right) \tag{4}$$

with generalized spontaneous emission rates Γ_{ij} arising from the coupling of the atomic transition dipoles through the vacuum field [23]. The incoherent transverse broadband pumping, which in our model acts on each atom in the same way, leads to

$$\mathscr{L}_{\text{pump}}[\rho] = \frac{R}{2}\sum_i \left(2\sigma_i^+\rho\sigma^- - \sigma_i^-\sigma_i^+\rho - \rho\sigma_i^-\sigma_j^+\right) \tag{5}$$

with R quantifying the pumping rate and cavity loss with the rate κ is described by

$$\mathscr{L}_{\text{cav}}[\rho] = \kappa\left(2a\rho a^\dagger - a^\dagger a\rho - \rho a^\dagger a\right). \tag{6}$$

Observe that the collective coupling and decay matrices $[\Omega_{ij}]$ and $[\Gamma_{ij}]$ possess non-diagonal elements, which have to be calculated as a function of the system's geometry [16]. In many other cases, due to the finite correlation length of vacuum fluctuations, these nondiagonal parts can be safely neglected. Explicitly, for identical atoms we have [24]

$$\Gamma_{ij} = \frac{3\Gamma}{2}F(k_0 r_{ij}) \qquad \Omega_{ij} = \frac{3\Gamma}{4}G(k_0 r_{ij}) \tag{7}$$

with Γ the single atom linewidth, $k_0 = \omega_0/c = 2\pi/\lambda_0$ and

$$\begin{aligned} F(\xi) &= \left(1-\cos^2\theta\right)\frac{\sin\xi}{\xi} + \left(1-3\cos^2\theta\right)\left(\frac{\cos\xi}{\xi^2} - \frac{\sin\xi}{\xi^3}\right), \\ G(\xi) &= -\left(1-\cos^2\theta\right)\frac{\cos\xi}{\xi} + \left(1-3\cos^2\theta\right)\left(\frac{\sin\xi}{\xi^2} + \frac{\cos\xi}{\xi^3}\right), \end{aligned} \tag{8}$$

where $\xi = k_0 r_{ij}$. Here, r_{ij} denotes the relative distance between the atoms i and j and θ is the angle the transition dipole draws with the vector connecting the two atoms.

A crucial property of a laser is its spectrum in the steady state. In order to calculate the spectral distribution of the light field inside the cavity we employ the Wiener-Khinchin theorem [25], where

$$S(\omega,t) = \int e^{-i\omega\tau}\left\langle a^\dagger(t+\tau)a(t)\right\rangle \mathrm{d}\tau. \tag{9}$$

Numerically, this is achieved by at first determining the steady state ρ_S, which can be calculated as the kernel of the Liouvillian, i.e. solving $\mathscr{L}[\rho_S] = 0$. Now, the annihilation operator a is applied and we let this state evolve. After a time τ has elapsed, we apply the creation operator $a^\dagger$ and Fourier-transform the trace of this aggregate, as the Fourier transformation of the expectation value of the field correlation function equates to the spectrum of the intra cavity and output light field.

3. Superradiant laser dynamics with confined ensembles

3.1. General properties of superradiant lasing

First, let us exhibit some general features of the dynamics of a laser with all atoms coupled equally to the cavity mode in the two idealized limiting cases of (a) fully collective and (b) individual independent spontaneous decay. Mathematically, this is implemented simply by setting (a) $\Gamma_{ij} = \Gamma$ for the collective case as discussed in [8] and (b) $\Gamma_{ij} = \Gamma\delta_{ij}$ for independent decay as studied in [2]. Surprisingly, the fully collective case is much easier to deal with numerically as the total collective spin magnitude is conserved and the Hilbert space for N atoms is restricted to the $N+1$ states of a spin-$N/2$ system. The effective pumping of the atoms can also be described as an independent or collective mechanism. Here we refrain from including dipole-dipole induced excitonic shifts of the energy levels. This assumption can be justified

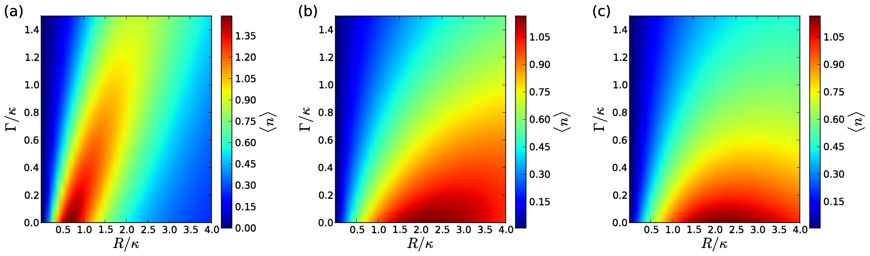

Fig. 2: Stationary photon number as a function of the pump strength R and the spontaneous decay rate Γ for collectively pumped and collectively decaying atoms (a), individually pumped but collectively decaying atoms (b) and individually pumped and individually decaying atoms (c)

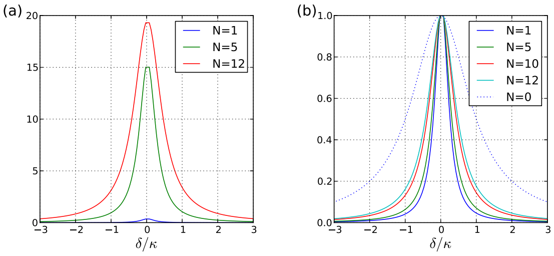

Fig. 3: Output spectrum of a fully collective laser with different atom numbers N for $\Gamma = \kappa/20$ and $R = \kappa/5$ compared to the empty cavity linewidth ($N = 0$), absolute (a) and normalized (b)

for a completely homogeneous atomic density [11] but has to be reconsidered for concrete finite size implementations. We will explicitly account for this in the finite lattice geometries discussed below.

Fig. 2 shows the mean photon number as a function of the pump strength R and the single atom decay rate Γ for the three cases of collective pump and collective decay, individual pump and collective decay and independent pump and independent decay for $N = 4$ atoms. We see that the maximum photon number is not so different for the three cases and appears at small spontaneous decay rates. For fully collective pump and collective spontaneous decay (fig. 2a)superradiant emission into free space limits the optimal operation regime to a lower pump intensity, though.

Now, it is of course most interesting to look at the frequency stability or line-width of this laser. As seen in fig. 3 the output intensity spectrum exhibits a nonlinear growth with the atom number (green line), as expected, until it saturates (red line). Remarkably, however, the linewidth does not narrow with the photon or atom number, but is even increased by superradiant spontaneous emission. Thus, the optimal case seems to be collective emission into the lasing mode without superradiant spontaneous decay. We will investigate this in more detail in the following sections.

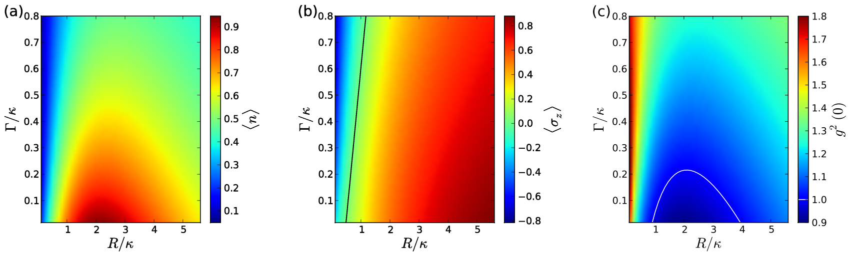

Fig. 4: Stationary operation of a four atom laser on a square lattice. (a) photon number, (b) atomic inversion, where the black line indicates equal population of the excited and the ground state, (c) $g^2(0)$ function, with the white line at $g^{(2)}(0) = 1$ representing a coherent state

3.2. *The superradiant lattice laser*

Above we have seen that collective decay and collective pump strongly change the laser dynamics and its properties. Besides modified decay rates governed by eq.4 in any finite size geometry dipole-dipole interaction as given by eq.2 has to be taken into account as well. To study the basic physical effects, in this section we will investigate three different regular geometric arrangements for the laser active atoms. We compare a linear chain, where we go beyond the single excitation and nearest-neighbor coupling limits discussed in [14], to an equilateral triangle and a square configuration. Let us point out, that for two atoms, e.g. [26], the particular relative arrangement is irrelevant, and therefore the system can be handled analytically.

3.2.1. A square lattice of four atoms

As a generic example we first show the photon number, the inversion of the active medium atoms and the $g^{(2)}(0)$ correlation function for a fixed cavity loss κ while tuning the pumping rate R and the individual atom decay rate Γ for a four atom laser in a square lattice. The chosen lattice constant is half of the magic wavelength for Strontium, $\lambda_{magic}/(2\lambda_0) \approx 0.58$ [27, 20]. For the photon number shown in fig. 4a the maximum appears at a pumping ratio of $R/\kappa = 2.2$, which is equal to the result from above for individual pumping and collective decay as depicted in fig. 2b.

In fig. 4b the expectation value of the σ_z operator is illustrated, where the black line represents the crossover to population inversion. On the right-hand side of the line the atom population is inverted, corresponding to the lasing case. Fig. 4c presents the $g^2(0)$ function, where the white line highlights a value of $g^2(0) = 1$, indicating a perfectly coherent light field. The area where $g^2(0) < 1$ could be referred to as an anti-bunching regime.

3.2.2. Comparison of different geometrical configurations

Let us study the influence of the geometric arrangement of the particles for different numbers of atoms and compare the results for the square discussed above to an equilateral triangle of atoms and a three and four atom chain. In order to obtain a substantial effect despite our small atom numbers, we choose a smaller lattice constant of $a = \lambda_0/10$ and a fixed atomic decay rate of $\Gamma/\kappa = 0.2$.

In fig. 5 we show, that for the average values the atom number is more important than the particular geometric arrangement. Interestingly for four atoms one can even reach sub Poissonian photon statistics.

Naturally, the results depend on the average distance of the atoms, which is shown in the

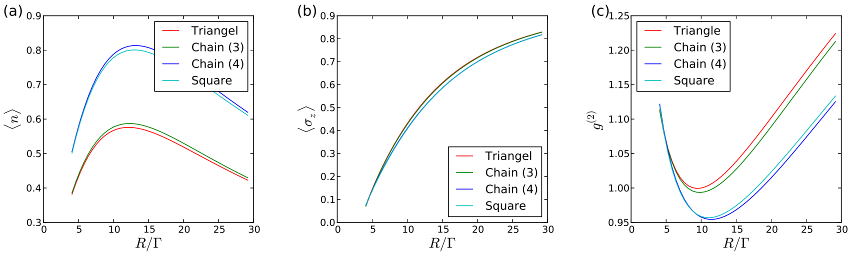

Fig. 5: Photon number (a), atomic inversion (b) and g^2 function (c) of the laser as a function of the pump strength R for different atomic arrangements and a fixed spontaneous decay rate $\Gamma = 0.2\kappa$

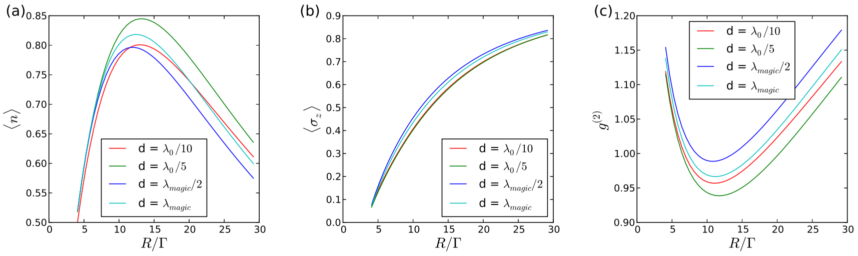

Fig. 6: Photon number (a), atomic inversion (b) and g^2 function (c) of the laser as a function of the pump strength R for a square of different lattice constants a and a fixed spontaneous decay rate $\Gamma = 0.2\kappa$

following set of pictures in fig. 6 for a square of different lattice constants a with a fixed spontaneous emission rate of $\Gamma/\kappa = 0.2$. As one might have expected, fig. 6 demonstrates a much more pronounced effect when varying the distance as opposed to changing the geometry.

Overall, despite fairly strong interactions of the atoms at small distances, the laser seems to be very robust against such pairwise perturbations, which appear to average out quite well once the oscillation threshold is surpassed. The differences increase with pump strength where, on average, more particles are excited.

4. Laser stability and frequency shifts for different atomic distances

Of course, the most sought after quality of a superradiant laser is its superb frequency stability and accuracy. In the first section we have seen that collective spontaneous decay can broaden the laser line and dipole-dipole interactions potentially shift its position. Now, we will study this effect for a lattice laser.

4.1. Laser linewidth and frequency shift

As is well known, the spectrum of a laser in the bad cavity limit deviates from the idealized Shawlow-Townes result, but the center of the line still approximately follows a Lorentzian [7] so that in our numerical analysis the linewidth and its center position relative to the bare atom line can be determined from a Lorentzian fit to the steady state spectrum, as described in sec. 2. Therefore, the width of the Lorentzian corresponds to the laser's linewidth while the offset

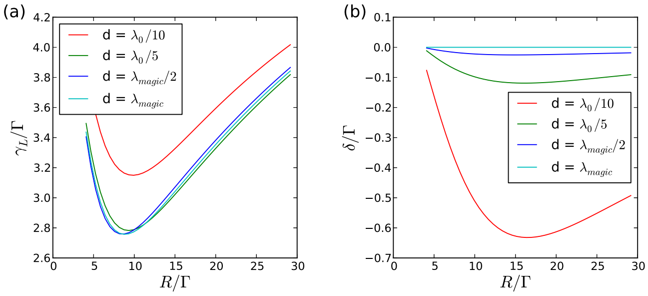

Fig. 7: Laser linewidth (a) and frequency shift (b) for a square atom arrangement at different distances as a function of the pump strength for a fixed atomic decay rate of $\Gamma = 0.2\kappa$

in the maximum describes the energy shift, which is the energy of the light field in the cavity relative to the cavity ground frequency. Fig. 7 and fig. 8 present the fitted width γ_L and the energy shift δ for different interatomic distances and geometrical configurations as a function of the pumping rate R. For these calculations the same parameters as above were used.

In fig. 7 we depict the linewidth and frequency shift of a laser with four atoms in a square configuration as a function of the pump strength for different inter atomic distances. We observe a minimum linewidth at a moderate pump strength of $R/\kappa \approx 1.9$, which corresponds to an operation at the maximally achievable photon number, as shown in fig. 4.

For a stronger pump the perturbations due to collective interactions dominate, though significant effects appear for very closely positioned atoms, i.e. $a < \lambda/2$, only. Even with just four atoms it is possible to achieve a linewidth significantly below the resonator's linewidth. The predicted frequency shift with respect to the bare atom frequency (as depicted in fig. 7) remains very small for larger interatomic distances and reaches a maximum value when the laser is operated at $R/\kappa \approx 3$, close to the maximum photon number. This could certainly be an observable phenomenon, but it is not detrimental for the operation of such a laser.

Interestingly, for the linewidth and shift properties, geometrical effects are more important than they are for the average intensity. A square arrangement of the atoms creates a much larger shift than a triangular or a linear array, as can be seen in fig. 8. Note that the increased shift with the atom number could lead to observable perturbations for larger ensembles. Again, operation at a lower pump intensity could help to minimize the effect.

4.2. *Laser sensitivity to cavity length fluctuations*

A central criterion for the stability of a laser is its sensitivity to fluctuations of the effective cavity length, which at present is one of the main limitations of reference oscillator stabilized lasers. Despite spectacular recent progress [28], comprehensive control at this level is still an extraordinary technical challenge. With the atoms acting as reference oscillators less effort in order to achieve technical stabilization is expected in an ideal superradiant laser. In the following we will study the effect of a varying cavity frequency described by an effective detuning ($\Delta = \omega_c - \omega_0$) on the average photon number (fig. 9) and the frequency mismatch between the bare atomic transition frequency and the laser field ($\delta_a = \omega_0 - \omega_L$) as seen in fig. 10 depending on the average atomic distance. As shown in fig. 9a for closely positioned atoms the interaction evokes a significant blue shift of the cavity frequency, generating the maximum photon number with respect to the clock transition. For atoms in a magic wavelength lattice (fig. 9b) this shift is much smaller and close to the interaction-free case. The detuning sensitivity of the laser output

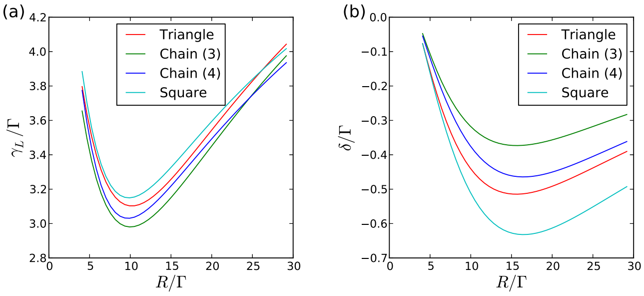

Fig. 8: Laser linewidth (a) and frequency shift (b) for different geometric configurations as a function of the pump strength for a fixed atomic decay rate of $\Gamma = 0.2\kappa$

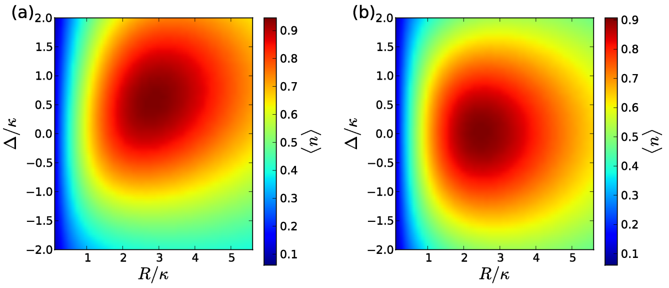

Fig. 9: Average photon number for atoms on a square with $a = \lambda_0/10$ (a) and $a = \lambda_{magic}/2$ (b) for variable cavity detuning and an atomic decay rate $\Gamma = 0.2\kappa$

spectrum in these two cases is depicted in fig. 10.

We see that the laser frequency pulling via the cavity changes with the interaction and increases with pumping and the intracavity photon number. Nevertheless, as indicated by the solid and dashed lines, the effective laser frequency change remains within an atomic linewidth even for cavity fluctuations on the order of the cavity width. At low pump strength and small inversion a sort of self-synchronization of the atomic dipoles via direct interactions can lead to very strong suppression of cavity fluctuations at the expense of very little output light, while for stronger pumping interaction effects are suppressed and the cavity drifts produce a more significant impact on the laser frequency. Overall, we observe that by choosing optimal operating conditions a decoupling of the cavity fluctuations from the laser frequency can be suppressed very effectively, even in the case of atomic interactions. However, this decoupling generally also reduces the output power of the laser.

5. Conclusions and outlook

By means of numerically solvable examples involving a few particles only, we have evaluated the influence of dipole-dipole interaction and collective spontaneous emission on the radiative properties of a superradiant laser in a lattice geometry. In general, even for fairly closely spaced atoms, shifts and frequency uncertainties are of the order of the free space atomic linewidth. Only for very densely packed ensembles superradiant free space decay will sub-

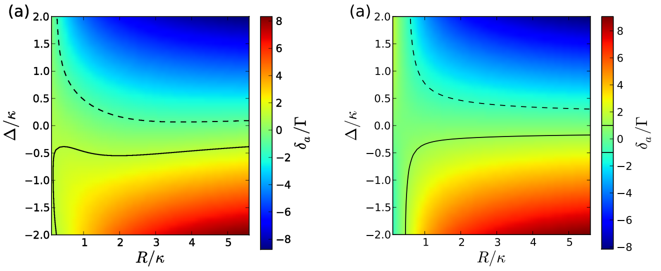

Fig. 10: Frequency shift for a square atom configuration with $a = \lambda_0/10$ (a) and $a = \lambda_{magic}/2$ (b) for variable detuning and a fixed atomic decay rate of $\Gamma = 0.2\kappa$. The dashed line represents $\delta_a/\Gamma = -1$ and the solid line corresponds to $\delta_a/\Gamma = 1$

stantially broaden the laser line and increase the sensitivity of the laser frequency to cavity drifts. Quantitatively, the various limiting cases of a completely collective laser as opposed to an independent atom system can lead to a different scaling behavior of the photon number and the linewidth with substantially different photon statistics. Fortunately, for a Strontium setup based on a magic wavelength lattice, the detrimental effects remain very small, although they could attain an observable magnitude at high filling. At optimally chosen operating conditions dipole dipole interaction can be exploited to reduce laser frequency fluctuations via direct phase stabilization even at very low photon numbers.

In this work we still assumed a rather ideal and to some extent artificial pumping mechanism, replenishing the upper atomic state by introducing the minimum necessary decoherence only, while also neglecting light shifts from the pump lasers. Any more realistic pumping via extra levels or an injection of excited atoms would, of course, add extra noise and has to be designed very carefully. This is one of the major remaining challenges for the implementation of such an optical version of the hydrogen maser. In any case, from the point of view of stability and shifts, the operation at weak pump strength seems favorable, although the very weak output field could be a technical challenge for practical use.

Acknowledgements

We thank M. Holland, D. Meiser, J. Ye, C. Genes and A. M. Rey for stimulating discussions and acknowledge support by DARPA through the QUASAR project and the Austrian Science Fund via the SFB Foqus project F4013.

6. Publication: Generalized mean-field approach to simulate the dynamics of large dissipative spin ensembles with long range interactions

Generalized mean-field approach to simulate the dynamics of large dissipative spin ensembles with long range interactions

S. Krämer and H. Ritsch
Institute for Theoretical Physics, Universität Innsbruck, Technikerstrasse 21, 6020 Innsbruck, Austria

We numerically study the collective coherent and dissipative dynamics in spin lattices with long range interactions in one, two and three dimensions. For generic geometric configurations with a small spin number, which are fully solvable numerically, we show that a dynamical mean-field approach based upon a spatial factorization of the density operator often gives a surprisingly accurate representation of the collective dynamics. Including all pair correlations at any distance in the spirit of a second order cumulant expansion improves the numerical accuracy by at least one order of magnitude. We then apply this truncated expansion method to simulate large numbers of spins from about ten in the case of the full quantum model, a few thousand, if all pair correlations are included , up to several ten-thousands in the mean-field approximation. We find collective modifications of the spin dynamics in surprisingly large system sizes. In 3D, the mutual interaction strength does not converge to a desired accuracy within the maximum system sizes we can currently implement. Extensive numerical tests help in identifying interaction strengths and geometric configurations where our approximations perform well and allow us to state fairly simple error estimates. By simulating systems of increasing size we show that in one and two dimensions we can include as many spins as needed to capture the properties of infinite size systems with high accuracy. As a practical application our approach is well suited to provide error estimates for atomic clock setups or super radiant lasers using magic wavelength optical lattices.

I. INTRODUCTION

Ensembles of interacting spins in various geometries have been at the heart of quantum statistical physics since the first models on magnetism were proposed [1]. As the spin-spin interaction is nonlinear and the corresponding Hilbert space grows exponentially with the number of spins, exact analytic as well as full numeric solutions are only possible for very special cases and geometries [2–4] or a small number of spins. The complexity increases even further for an open system including collective decay. As a very successful approximate numerical approach based on the factorization of single site expectation values, a dynamical mean-field method was developed for efficient treatment of larger systems [5]. On the one hand it allowed for analytical results in the large dimensions limit [6] while, on the other hand, it soon proved very useful for a numerical treatment in low dimensions. Subsequently, the general idea of the method was successfully applied to a wide range of solid state physics models in the very low temperature quantum domain [7]. Recently, this approach has proven useful in the description of ultra-cold particle dynamics in optical lattices [8, 9].

The present work is motivated by another, more recent implementation of spin lattices based on ultra-cold atoms or molecules trapped in an optical lattice, which nowadays can be prepared almost routinely in the laboratory with well defined filling factors and close to zero temperature [10, 11]. When excited on an optical or infrared transition, the trapped particles will interact via dipole-dipole energy exchange forming collective excitations [12, 13]. In addition, optical transitions intrinsically exhibit dissipation via spontaneous decay, which in such a lattice becomes a collective effect leading to super- or sub-radiance [14]. In order to consistently treat such an open system, one has to start from a master equation instead of the Schroedinger equation after having traced out the electromagnetic vacuum modes [15]. While the interaction between a pair of spins can be rather small at a larger distance, the collective effect of a sizable number of particles can still generate noticeable effects in this case[13].

Besides using polar molecules, which can possess relatively strong dipole moments [16], another interesting implementation is based on using long lived atomic clock transitions in a differential light-shift-free magic wavelength lattice [17, 18], where one obtains extremely well controllable and precisely measurable systems to study even weak spin interactions [19] and collective decay via dipole-dipole energy exchange [14]. For sufficient densities the particles' effective transition frequency and spontaneous decay is modified by dipole-dipole interaction [20], which in turn will influence the performance of a corresponding clock or super-radiant laser [21].

While the extremely small dipole moment of a clock transition keeps these interactions small, even tiny shifts and broadenings will ultimately influence clock accuracy and precision. Hence, reliable and converging numerical models are required to estimate these effects to many digits, in particular as one tries to work with as large as possible an ensemble to reduce measurement time and projection noise. For rather small atom numbers, up to about 10, a numerical solution of the full master equation is still possible [20] and has showed that shifts and broadening can be non-negligible. For larger ensembles at low densities a so called cluster approach based on statistical averaging of important small particle number configurations has already produced first estimates of their scaling with the system's size [22]. Here, we focus on a more generally valid approach, namely the above mentioned mean-field plus pair-correlation method (MPC) to tackle large systems at high densities, i.e. up to unit filling. The long range nature of the dipole coupling is accounted for by adding higher order corrections to the standard local factorization approach. In particular, for cavity mediated dipole interactions or coupling via nano-fibers even infinite range interactions have to be considered [23]. The focus of this work is put on developing the appropriate general numerical framework to treat such extended open spin lattices in various configurations and test their accuracy and convergence properties by means of the example of collective decay of a highly excited spin state. This should be the basis of future more specific work on concrete implementations of lattice clock Ramsey spectroscopy [24] and super-radiant laser setups [21, 25].

This work is organized as follows. First, we give a short description of the system of coupled spins and introduce the corresponding master equation governing their time evolution including decay. Using generalized factorization assumptions for the density operator of the system we derive two approximate and numerically advantageous methods to calculate its time evolution. In the subsequent section we perform calculations for large ensembles studying the influence of long-range interactions. Here, we add an extensive numerical analysis to characterize the magnitude and scaling of the error of these two approximations depending on the geometry and the choice of initial state. Finally, we use this method to simulate systems of increasing size to study to which extend a finite sized sample can capture the dynamics of larger or even infinite systems.

II. INTERACTING SPIN DYNAMICS

We consider a system consisting of N two-level subsystems with transition frequency ω_0 and decay rate γ in an arbitrary spatial configuration. Each particle couples to the modes of the free electro-magnetic field and therefore all particles are indirectly coupled to one another. Mathematically, this problem can be simplified by treating the electro-magnetic modes as a single bath and introducing effective particle-particle interactions and effective decay of particle excitations into this bath, according to [12]. The time evolution of the N spins in a rotating frame corresponding to $\sum_i \omega_0 \sigma_i^z$ is then governed by a master equation

$$\dot{\rho} = -\frac{i}{\hbar}\big[H, \rho\big] + \mathcal{L}[\rho] \tag{1}$$

with the Hamiltonian

$$H = \sum_{ij;i\neq j} \hbar \Omega_{ij} \sigma_i^+ \sigma_j^- \tag{2}$$

and Lindblad-term

$$\mathcal{L}[\rho] = \frac{1}{2}\sum_{i,j} \Gamma_{ij}(2\sigma_i^- \rho \sigma_j^+ - \sigma_i^+ \sigma_j^- \rho - \rho \sigma_i^+ \sigma_j^-). \tag{3}$$

The dipole-dipole interaction $\Omega_{ij} = \frac{3}{4}\gamma G(k_0 r_{ij})$ and the collective decay $\Gamma_{ij} = \frac{3}{2}\gamma F(k_0 r_{ij})$ can be obtained analytically with

$$F(\xi) = \alpha \frac{\sin\xi}{\xi} + \beta\left(\frac{\cos\xi}{\xi^2} - \frac{\sin\xi}{\xi^3}\right) \tag{4a}$$

$$G(\xi) = -\alpha \frac{\cos\xi}{\xi} + \beta\left(\frac{\sin\xi}{\xi^2} + \frac{\cos\xi}{\xi^3}\right) \tag{4b}$$

with $\alpha = 1 - \cos^2\theta$ and $\beta = 1 - 3\cos^2\theta$, where θ represents the angle between the line connecting atoms i and j and the common atomic dipole orientation [12].

While in systems consisting of only very few particles we can study the time evolution by directly integrating the master equation, the exponential scaling of the dimension of the Hilbert space soon defeats any numerical abilities. To be able to represent the state of such a high particle number system in a computer one has to make simplifying assumptions about the form of the density matrix. In our following calculations we will truncate correlations between the particles at a certain order which greatly reduces the space needed to store the state of the system in memory and allows for treating larger particle numbers.

A. Mean-field method: product state assumption

In the first nontrivial approximation we neglect correlations altogether and assume that the system is at all times in a product state of the subsystems at each site. The density matrix is approximated by $\rho = \bigotimes_k \rho^{(k)}$, which is also called *mean-field approximation*. The time evolution of the system is then governed by the local on site density matrices, which for two-level systems can be obtained from a complete set of expectation values for each spin, i.e. the expectation values of the Pauli operators $\langle\sigma_x\rangle$, $\langle\sigma_y\rangle$ and $\langle\sigma_z\rangle$ for a spin 1/2 system. Using this Pauli representation we need three real numbers to characterize the state of each of the two-level sub-systems at a certain point in time. The resulting equations for the local spin provide an intuitive insight into the corresponding physics. Explicitly we get:

$$\dot{\langle\sigma_k^x\rangle} = \sum_{i;i\neq k} \Omega_{ki} \langle\sigma_i^y \sigma_k^z\rangle - \frac{1}{2}\gamma\langle\sigma_k^x\rangle - \frac{1}{2}\sum_{i;i\neq k} \Gamma_{ki}\langle\sigma_i^x \sigma_k^z\rangle \tag{5a}$$

$$\dot{\langle\sigma_k^y\rangle} = -\sum_{i;i\neq k} \Omega_{ki} \langle\sigma_i^x \sigma_k^z\rangle - \frac{1}{2}\gamma\langle\sigma_k^y\rangle - \frac{1}{2}\sum_{i;i\neq k} \Gamma_{ki}\langle\sigma_i^y \sigma_k^z\rangle \tag{5b}$$

$$\begin{aligned}\dot{\langle\sigma_k^z\rangle} = &-i\sum_{i;i\neq k} \Omega_{ki}\Big(\langle\sigma_k^x \sigma_i^y\rangle - \langle\sigma_i^x \sigma_k^y\rangle\Big) + \gamma\big(1 - \langle\sigma_k^z\rangle\big) \\ &+ \frac{1}{2}\sum_{i;i\neq k} \Gamma_{ki}\Big(\langle\sigma_k^x \sigma_i^x\rangle + \langle\sigma_i^y \sigma_k^y\rangle\Big)\end{aligned} \tag{5c}$$

These equations still contain two-particle expectation values of the form $\langle\sigma_i^\alpha \sigma_j^\beta\rangle$, which according to our above assumption can be factorized, i.e. $\langle \sigma_i^\alpha \sigma_j^\beta \rangle \approx \langle \sigma_i^\alpha \rangle \langle \sigma_j^\beta \rangle$. As we will see in the next section for weak inter-particle interactions this gives a surprisingly good approximation to the interaction induced shifts and can also account for spatial inhomogeneities of the system.

B. Extended mean-field method including pair-correlations (MPC)

As a next-order correction to the above mean-field approach we now include pair-correlations but still neglect all higher-order correlations. To this end the density matrix can be approximated by $\rho = \bigotimes_i \rho^{(i)} + \sum_{j<k} \Big(\rho^{(j,k)} \otimes \bigotimes_{i \neq j,k} \rho^{(i)} \Big)$, where the first term is the previously used product state and the correlations are captured in the operators $\rho^{(j,k)}$. The correlations thus have to be chosen to generate vanishing single particle expectation values, i.e. $\mathrm{Tr}\left\{ \sigma_i^\alpha \rho^{(j,k)} \right\} = 0$. Deriving the equations of motion in terms of expectation values of Pauli operators leads to the same equations as in the mean-field case (eq. 5). The two-particle expectation values are then determined via a set of additional equations for the expectation values of all two-particle Pauli operator pairs of the type $\langle \sigma_i^\alpha \sigma_j^\beta \rangle$. In principle, there are nine such quantities for any pair of particles $\rho^{(j,k)}$. For symmetry reasons three of them are trivially obtained from the others. Similarly to the mean-field in the equations for these two-particle correlations higher order three-particle correlations appear, which based on our assumption of the form of the density operator are again approximated by

$$\begin{aligned} \langle \sigma_i^\alpha \sigma_j^\beta \sigma_k^\gamma \rangle \approx & -2 \langle \sigma_i^\alpha \rangle \langle \sigma_j^\beta \rangle \langle \sigma_k^\gamma \rangle + \langle \sigma_i^\alpha \rangle \langle \sigma_j^\beta \sigma_k^\gamma \rangle + \langle \sigma_j^\beta \rangle \langle \sigma_i^\alpha \sigma_k^\gamma \rangle \\ & + \langle \sigma_k^\gamma \rangle \langle \sigma_i^\alpha \sigma_j^\beta \rangle. \end{aligned} \tag{6}$$

Although the resulting equations of motions for the two-particle correlations are arguably bulky, we want to display them explicitly, as the form an essential basis of our work.

$$\begin{aligned} \dot{\langle \sigma_k^x \sigma_l^x \rangle} = & \sum_{j;j \neq k,l} \Omega_{kj} \langle \sigma_k^z \sigma_l^x \sigma_j^y \rangle + \sum_{j;j \neq k,l} \Omega_{lj} \langle \sigma_k^x \sigma_l^z \sigma_j^y \rangle \\ & - \gamma \langle \sigma_k^x \sigma_l^x \rangle + \Gamma_{kl} \Big(\langle \sigma_k^z \sigma_l^z \rangle - \frac{1}{2} \langle \sigma_k^z \rangle - \frac{1}{2} \langle \sigma_l^z \rangle \Big) \\ & - \frac{1}{2} \sum_{j;j \neq k,l} \Gamma_{kj} \langle \sigma_k^z \sigma_l^x \sigma_j^x \rangle - \frac{1}{2} \sum_{j;j \neq k,l} \Gamma_{lj} \langle \sigma_k^x \sigma_l^z \sigma_j^x \rangle \end{aligned} \tag{7a}$$

$$\begin{aligned} \dot{\langle \sigma_k^y \sigma_l^y \rangle} = & - \sum_{j;j \neq k,l} \Omega_{kj} \langle \sigma_k^z \sigma_l^y \sigma_j^x \rangle - \sum_{j;j \neq k,l} \Omega_{lj} \langle \sigma_k^y \sigma_l^z \sigma_j^x \rangle \\ & - \gamma \langle \sigma_k^y \sigma_l^y \rangle + \Gamma_{kl} \Big(\langle \sigma_k^z \sigma_l^z \rangle - \frac{1}{2} \langle \sigma_k^z \rangle - \frac{1}{2} \langle \sigma_l^z \rangle \Big) \\ & - \frac{1}{2} \sum_{j;j \neq k,l} \Gamma_{kj} \langle \sigma_k^z \sigma_l^y \sigma_j^y \rangle - \frac{1}{2} \sum_{j;j \neq k,l} \Gamma_{lj} \langle \sigma_k^y \sigma_l^z \sigma_j^y \rangle \end{aligned} \tag{7b}$$

$$\begin{aligned} \dot{\langle \sigma_k^z \sigma_l^z \rangle} = & \sum_{j;j \neq k,l} \Omega_{kj} \Big(\langle \sigma_k^y \sigma_l^z \sigma_j^x \rangle - \langle \sigma_k^x \sigma_l^z \sigma_j^y \rangle \Big) \\ & + \sum_{j;j \neq k,l} \Omega_{lj} \Big(\langle \sigma_k^z \sigma_l^y \sigma_j^x \rangle - \langle \sigma_k^z \sigma_l^x \sigma_j^y \rangle \Big) \\ & - 2\gamma \langle \sigma_k^z \sigma_l^z \rangle + \gamma \big(\langle \sigma_l^z \rangle + \langle \sigma_k^z \rangle \big) \\ & + \Gamma_{kl} \Big(\langle \sigma_k^y \sigma_l^y \rangle + \langle \sigma_k^x \sigma_l^x \rangle \Big) \\ & + \frac{1}{2} \sum_{j;j \neq k,l} \Gamma_{kj} \Big(\langle \sigma_k^x \sigma_l^z \sigma_j^x \rangle + \langle \sigma_k^y \sigma_l^z \sigma_j^y \rangle \Big) \\ & + \frac{1}{2} \sum_{j;j \neq k,l} \Gamma_{lj} \Big(\langle \sigma_k^z \sigma_l^x \sigma_j^x \rangle + \langle \sigma_k^z \sigma_l^y \sigma_j^y \rangle \Big) \end{aligned} \tag{7c}$$

$$\begin{aligned} \dot{\langle \sigma_k^x \sigma_l^y \rangle} = & \, \Omega_{kl} \Big(\langle \sigma_k^z \rangle - \langle \sigma_l^z \rangle \Big) + \sum_{j;j \neq k,l} \Omega_{kj} \langle \sigma_k^z \sigma_l^y \sigma_j^y \rangle \\ & - \sum_{j;j \neq k,l} \Omega_{lj} \langle \sigma_k^x \sigma_l^z \sigma_j^x \rangle - \gamma \langle \sigma_k^x \sigma_l^y \rangle \\ & - \frac{1}{2} \sum_{j;j \neq k,l} \Gamma_{kj} \langle \sigma_k^z \sigma_l^y \sigma_j^x \rangle - \frac{1}{2} \sum_{j;j \neq k,l} \Gamma_{lj} \langle \sigma_k^x \sigma_l^z \sigma_j^y \rangle \end{aligned} \tag{7d}$$

$$\begin{aligned} \dot{\langle \sigma_k^x \sigma_l^z \rangle} = & \, \Omega_{kl} \langle \sigma_l^y \rangle + \sum_{j;j \neq k,l} \Omega_{kj} \langle \sigma_k^z \sigma_l^z \sigma_j^y \rangle \\ & + \sum_{j;j \neq k,l} \Omega_{lj} \Big(\langle \sigma_k^x \sigma_l^y \sigma_j^x \rangle - \langle \sigma_k^x \sigma_l^x \sigma_j^y \rangle \Big) \\ & - \frac{3}{2} \gamma \langle \sigma_k^x \sigma_l^z \rangle + \gamma \langle \sigma_k^x \rangle - \Gamma_{kl} \Big(\langle \sigma_k^z \sigma_l^x \rangle - \frac{1}{2} \langle \sigma_l^x \rangle \Big) \\ & - \frac{1}{2} \sum_{j;j \neq k,l} \Gamma_{kj} \langle \sigma_k^z \sigma_l^z \sigma_j^x \rangle \\ & + \frac{1}{2} \sum_{j;j \neq k,l} \Gamma_{lj} \Big(\langle \sigma_k^x \sigma_l^x \sigma_j^x \rangle + \langle \sigma_k^x \sigma_l^y \sigma_j^y \rangle \Big) \end{aligned} \tag{7e}$$

$$\begin{aligned} \dot{\langle \sigma_k^y \sigma_l^z \rangle} = & - \Omega_{kl} \langle \sigma_l^x \rangle - \sum_{j;j \neq k,l} \Omega_{kj} \langle \sigma_k^z \sigma_l^z \sigma_j^x \rangle \\ & + \sum_{j;j \neq k,l} \Omega_{lj} \Big(\langle \sigma_k^y \sigma_l^y \sigma_j^x \rangle - \langle \sigma_k^y \sigma_l^x \sigma_j^y \rangle \Big) \\ & - \frac{3}{2} \gamma \langle \sigma_k^y \sigma_l^z \rangle + \gamma \langle \sigma_k^y \rangle - \Gamma_{kl} \Big(\langle \sigma_k^z \sigma_l^y \rangle - \frac{1}{2} \langle \sigma_l^y \rangle \Big) \\ & - \frac{1}{2} \sum_{j;j \neq k,l} \Gamma_{kj} \langle \sigma_k^z \sigma_l^z \sigma_j^y \rangle \\ & + \frac{1}{2} \sum_{j;j \neq k,l} \Gamma_{lj} \Big(\langle \sigma_k^y \sigma_l^x \sigma_j^x \rangle + \langle \sigma_k^y \sigma_l^y \sigma_j^y \rangle \Big) \end{aligned} \tag{7f}$$

Note, that the number of equations to be solved increases quadratically with the number of particles, as we include all possible two-particle combinations. This is exponentially slower than the growth of the corresponding Hilbert space. In many cases one might even be able to restrict this to nearest neighbor couplings only, but for long range dipole or cavity mediated interactions, in which we are interested here, no such truncations can be performed safely. In principle the method, which in many respects resembles the known cumulant expansion method [26], can be extended towards higher order. However, as we will see below, it is already very accurate for our purposes so that we will not pursue this task.

III. NUMERICAL ACCURACY OF MEAN-FIELD METHOD AND SECOND ORDER CORRECTIONS

In the previous section we have presented two numerical approaches to approximate the master equation (eq. 1) by neglecting higher-order quantum correlations. In order to examine for which conditions these assumptions lead to accurate solutions, we compare these approximations with the numerical solution of the full master equation for different spatial arrangements, numbers of particles and initial states. Additionally we also calculate the case of independent particles, which allows us to identify examples where the error of the approximation is small due to a negligible influence of the dipole-dipole-interaction and the collective decay.

1. Spin dynamics

To obtain a first intuitive understanding for the quality of the different methods we compare the time evolution of the expectation values of the Pauli operators for three different geometries, i.e. a chain (fig. 1), a square lattice (fig. 2) and a cube (fig. 3). As a generic physical example, we start with a product state of all spins pointing in x-direction. This is the state prepared in the first step of a typical Ramsey spectroscopy procedure. It is fully superradiant when all particles are confined in a very small spatial volume. Clearly, the dynamics of all three cases is significantly different, but they all share certain features. First, the solution of the full master equation deviates drastically from the independent particle case, which means that the effect of the collective interaction is significant. This deviation is almost perfectly captured by the second order MPC solution, which is, at least visually, almost identical to the full solution of the master equation. Surprisingly, the mean-field solution shows a qualitatively similar behavior already, although it is noticeably not as accurate. Note, that for the case of the cube (fig. 3) both methods predict the subradiance of the initial spin state well [24]. Let us now turn from a visual to a more systematic numerical error estimation.

2. Systematic accuracy analysis

In the following we will perform a more rigorous, quantitative analysis for a large range of parameters. In order to do this effectively we need a simple measure of accuracy of the different methods. A frequently used tool, especially in quantum information, is the trace distance which is defined as $\mathcal{T}(\rho,\sigma) = \frac{1}{2}|\lambda_i|$ where the λ_i are the eigenvalues of the matrix representation of $\rho - \sigma$. For qubits this measure has a very intuitive interpretation, it is just half of the geometric distance of the two states on the Bloch sphere. In fig. 4 we use this trace distance between the solution of the master equation and the previously presented numerical methods at equal points in time to characterize the error of the different approximations. In all our examples we initially start in a product state, which means that the error at $t = 0$ is always zero and since no additional pumping is included the system decays to the ground state and the trace distance in the long time limit will vanish for all numerical methods. Instead of inspecting the variation of the trace distance over time we will use the time-maximum of the trace distance as a characterization of the error.

A. Geometry dependence

In this section we study the geometry dependence of the error of the numerical methods measured by the previously introduced time maximum of the trace distance. We distinguish between systems of different dimensionality, a 1D chain consisting of 8 particles (fig. 5), a 3x3 section of a 2D square lattice (fig. 6) and a cube as a 3D configuration (fig. 7). For each of these examples we calculate the dependence of the error on the distance between the particles. Further on we vary the initial state and the orientation of the polarization vector and show three typical results. In the following the initial state is characterized by Θ which measures the polar angle between a given state towards the ground state on the Bloch sphere.

Several interesting features stand out immediately. The bigger the distance between the particles, the smaller the error of neglecting higher-order correlations. As can be seen from the trace distance between the solution of the master equation and the independently decaying case this is to some degree an artifact of the decreasing strength of the dipole-dipole interaction which in the far field limit has a $\frac{1}{r}$ dependency but at least for MPC the error decreases much faster. In nearly all cases the mean-field approach yields a noticeable improvement, yet, when all spins start in the excited state it reproduces the results of independent particles only. In fact, as one can show from the mean-field equations, in this case the time evolution is completely identical, so mean-field results in no improvement over simply ignoring the collective effects.

B. Initial state dependence

To further analyze the dependence of the error on the initial state we consider a chain of six particles with three different particle distances. Initially the system is in a product state where all single particles are in the same Bloch state. For simplicity we only consider pure states and since the time evolution is invariant under a global rotation around the z-axis the only remaining variable is

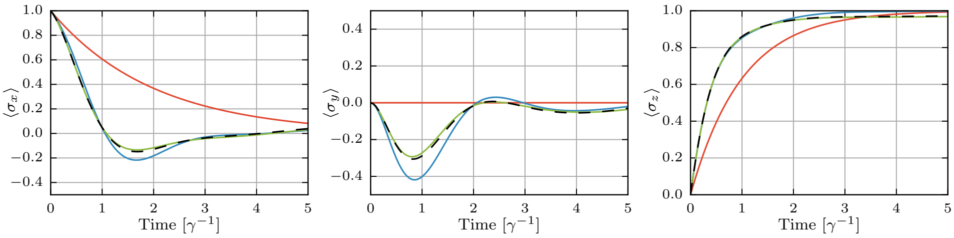

FIG. 1. Time evolution of the expectation values of the Pauli operators σ_x, σ_y and σ_z of the central spin in a chain consisting of 7 spins with spin-spin distance $d = 0.15\lambda_0$. The system is simulated using independent spins (red), the mean-field method (blue), MPC (green) and by solving the whole master equation (dashed black). The dipole is orientated orthogonally to the chain.

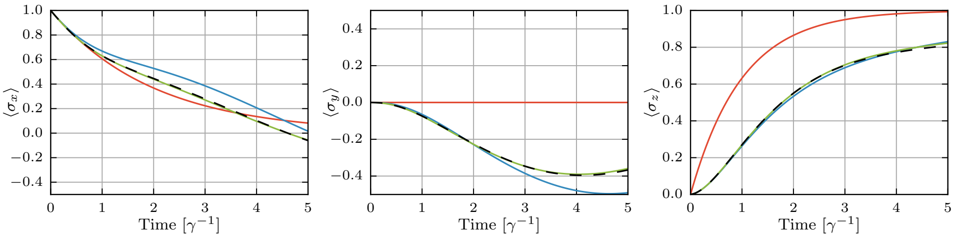

FIG. 2. Time evolution of the expectation values of the Pauli operators σ_x, σ_y and σ_z of the central spin in a 2D-square lattice consisting of 3x3 spins with nearest spin-spin distance $d = 0.5\lambda_0$. The system is simulated using independent spins (red), the mean-field method (blue), MPC (green) and by solving the whole master equation (dashed black). The dipole is orientated orthogonally to the plane.

the polar angle Θ. In fig. 8 the dependence of the error on this polar angle is shown. For $\Theta = 0$ the system is in the ground state and the error vanishes. For a small excitation the mean-field method gives a substantial improvement compared to the independently decaying system but for a nearly totally excited state the advantage disappears more and more. In contrast, MPC performs convincingly for all initial states.

C. Spin-number dependence

Finally, we investigate the dependence of the error on the number of particles in the system, i.e. a chain consisting of N particles. The result of this analysis is shown in fig. 9a. In this double logarithmic plot the error appears to be nearly linear but slightly shifted for varying particle numbers which leads us to the following estimate for the error

$$\mathrm{err}(N, d) = C_N * d^{k_N}. \tag{8}$$

The exponent k_N and the factor C_N can be extracted from this error plot and are shown in fig. 9b and fig. 9c respectively. The error exponent turns out to be independent of the number of particles and is -1 for independently decaying spins which is not surprising since the collective interaction in the far field drops with $\frac{1}{r}$. However, increasing the distances doesn't improve the mean-field results whereas MPC has an error exponent of -2 and gains drastically on accuracy.

IV. APPROXIMATION OF VERY LARGE (INFINITE) SYSTEMS

Recent research on the effect of geometry on the perturbation of the spin dynamics by collective interactions was mostly limited to systems consisting of only very few atoms. In lack of better alternatives one might be tempted to extrapolate results obtained from these small-sized systems to larger ensembles but in general this attempt could fail miserably. Armed with the knowledge about the accuracy of the mean-field and MPC methods and their ability to simulate moderately large systems we can use them to investigate how many particles are needed to make satisfying statements about infinite systems. More precisely, we want to know how collective spin quantities of the type $\frac{1}{N}\sum_i \langle\sigma_i^\alpha\rangle$ will change for different numbers of particles. Of course, it is not a priori clear if these expectation values will converge at all. To

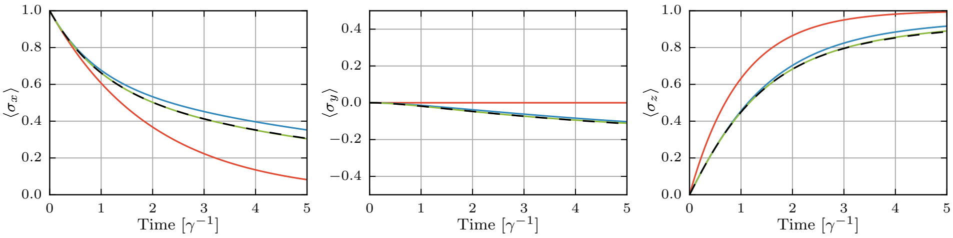

FIG. 3. Time evolution of the expectation values of the Pauli operators σ_x, σ_y and σ_z of a single spin in a cube configuration with nearest spin-spin distance $d = 0.6\lambda_0$. The system is simulated using independent spins (red), the mean-field method (blue), MPC (green) and by solving the whole master equation (dashed black). The dipole is orientated orthogonally to an arbitrary face of the cube.

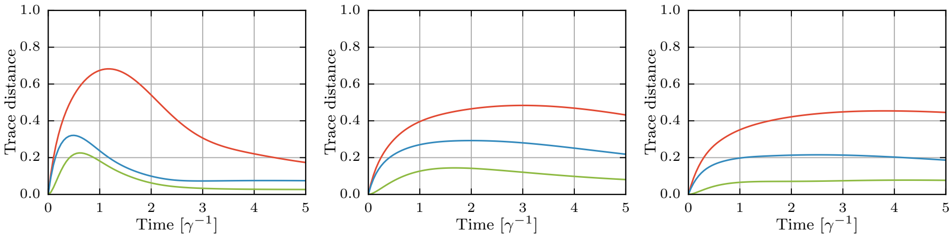

FIG. 4. Trace distance between the density operators calculated by the master equation and density operators calculated for independent spins (red), mean-field (blue) and MPC (green) for the previously discussed chain configuration (a), 3x3 square lattice (b) and cube configuration (c).

answer this question we will study two different examples.

A. Linear equidistant chain

We consider a N-particle spin chain with particle distance d and calculate the dynamics of the whole system where initially all spins are in the $\langle\sigma_x\rangle = 1$ state. Tracing out all but the innermost spin allows us to compare the dynamics of this single spin for a varying number of surrounding particles. The result of this analysis for a certain distance d after an integration time of $2\gamma^{-1}$ is shown in fig. 10. Fortunately, all methods yield more or less the same result and differ significantly from the independently decaying case, indicating that the variation for small particle numbers and the ultimate convergence for large systems is not a numerical artifact. This result hints at the fact that a suitable number of particles will indeed give a usable approximation of big systems. To consolidate this claim we perform a more extensive and quantitative test. What we actually would like to test is how much the time evolution of the single central spin in a chain consisting of N particles differs from the time evolution of a spin in an infinite chain. However, we are not aware of a method to solve the infinite chain exactly which leaves us with the option to compare the central spin of a N particle chain with a chain containing as many spins as numerically possible only. In fig. 11 and fig. 12, the dynamics of a 20001 particle mean-field simulation and a 401 particle MPC simulation are used as the best possible approximation of an infinite chain for three different spin-spin distances, respectively. In most cases the addition of further spins affects the central spin less and less and is approximately linear in this double logarithmic plot, i.e. the trace distance between the infinite chain and the N-particle chain for a certain distance can be estimated by $T(N, \inf) = C_d N_d^k$. By fitting this function to the numerical results we can determine the exponent k_d and the factor C_d depending on the distance which is plotted in fig. 13. For nearly all distances both the mean-field method as well as the MPC method predict that adding further particles has an effect proportional to $\frac{1}{N}$ only, allowing us to easily estimate the number of particles needed to approximate the infinite chain dynamics to a desired accuracy. However, when the spin-spin distance is close to a multiple of the transition wavelength λ_0, the dynamics of the infinite chain never seems to be captured by a finite size approximation.

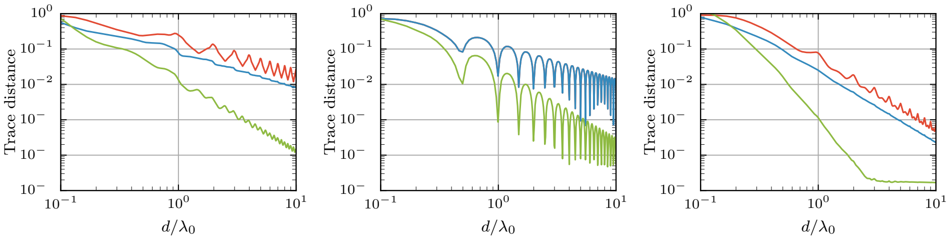

FIG. 5. Distance dependency of the time-maximum of the trace distance between the results of the master equation and the results of an independent evolution (red), mean-field (blue) and MPC (green) for a chain consisting of 8 spins for different initial states and dipole orientations. (a) $\Theta = \pi/2$, $e_{dipole} = e_z$. (b) $\Theta = \pi$, $e_{dipole} = e_z$. (c) $\Theta = \pi/2$, $e_{dipole} = e_x$.

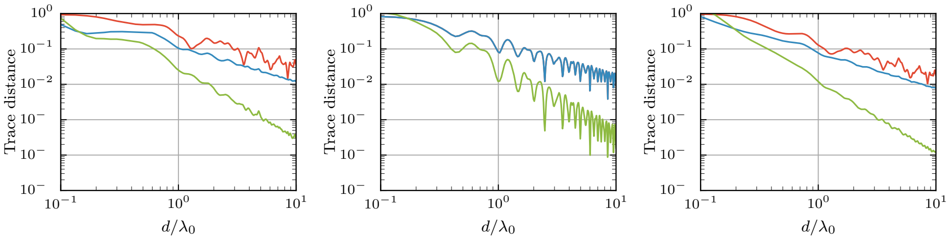

FIG. 6. Distance dependency of the time-maximum of the trace distance between results of the master equation and results of independent evolution (red), mean-field (blue) and MPC (green) for a square lattice consisting of 3x3 spins for different initial states and dipole orientations. (a) $\Theta = \pi/2$, $e_{dipole} = e_z$. (b) $\Theta = \pi$, $e_{dipole} = e_z$. (c) $\Theta = \pi/2$, $e_{dipole} = e_x$.

B. Hexagonal lattice

With these very encouraging results for a 1D chain, let us see, if this holds true for higher dimensional geometries as well. Unfortunately we failed to obtain convincing results for 3D cubic lattices, since the number of particles needed for convergence of the numerical result turns out to very much exceed the possibility of MPC and even of the mean-field method. For 2D geometries at least, the mean-field method delivers some meaningful, albeit by far not as beautiful results. Fig. 14 shows the numerically obtained approximations for the error exponent and the error factor for the case of a hexagonal lattice, where additional particles are added in rings around the central spin. The outcome looks rather noisy, probably due to too small a choice for the number of particles used as an approximation of the infinite lattice. It turns out that compared to the chain a lot more particles are needed to reliably approximate an infinite hexagonal lattice, i.e. the influence of additional particles reduces the error with approximately $N^{-0.3}$, where this exponent is a rather rough estimate.

V. NUMERICAL COMPLEXITY OF THE DIFFERENT METHODS

Finally we want to add some considerations on the memory and CPU requirements of the different methods and show that our implementations behave as expected in this regard. When solving the master equation the state of the system is captured as a density matrix of dimension 2^{2N}. The time evolution according to a master equation is equivalent to a matrix-matrix multiplication and therefore has a time complexity of $O(2^{3N})$. In the case of mean-field a state can be characterized by $3N$ real numbers and according to the mean-field equations (eq. 5) the time complexity is then approximately $O(N^2)$. For the MPC method the state consists of one mean-field state and nine correlation matrices of the form $C_{ij}^{\alpha\beta} = \langle\sigma_i^\alpha \sigma_j^\beta\rangle$. Using the relation $C_{ij}^{\alpha\beta} = C_{ji}^{\alpha\beta}$ means that we need roughly $\frac{9N^2}{2}$ real numbers to represent one MPC state. The time complexity is, according to the MPC equations (eq. 7), approximately $O(N^3)$. The results of this analysis are presented in fig. 15.

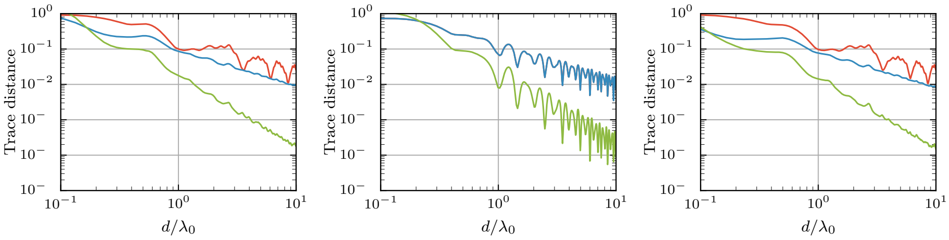

FIG. 7. Distance dependency of the time-maximum of the trace distance between the results of the master equation and the results of independent evolution (red), mean-field (blue) and MPC (green) for 8 spins in a cube configuration for different initial states and dipole orientations. (a) $\Theta = \pi/2$, $e_{dipole} = e_z$. (b) $\Theta = \pi$, $e_{dipole} = e_z$. (c) $\Theta = \pi/2$, $e_{dipole} = \frac{1}{\sqrt{3}}(e_x + e_y + e_z)$.

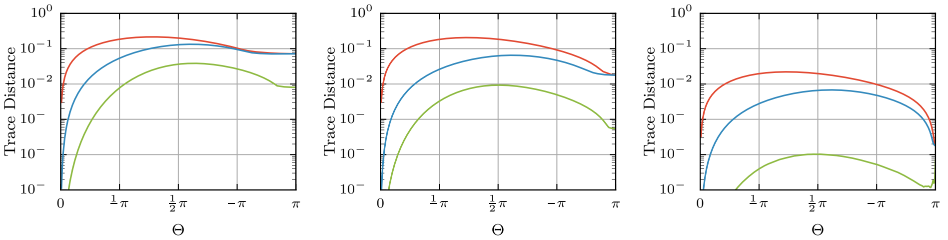

FIG. 8. Dependence of the time-maximum of the trace distance between the results of the master equation and the results of an independent evolution (red), mean-field (blue) and MPC(green) on the initial Bloch state characterized by the polar angle Θ for a chain consisting of 6 spins with spin-spin distance $d = 0.5\lambda_0$ (a), $d = 1.0\lambda_0$(b) and $d = 10.0\lambda_0$ (c).

VI. CONCLUSIONS AND OUTLOOK

We have demonstrated that an effective mean-field method with added pair correlations provides a numerically efficient and surprisingly accurate method to simulate open spin systems with general non local spin-spin interaction and collective decay up to moderately high particle numbers and significant interaction strength. Particularizing to dipole-dipole interaction and collective spontaneous decay has allowed us to establish a numerical estimate of the accuracy and scaling properties of our methods. Furthermore we can show for 1D chains that tractable system sizes already approach the behavior of infinite systems allowing for an estimate of the magnitude of the error due to the truncation of the system. For 2D systems the lowest order mean-field approach still allows to reach adequate system sizes to approximate infinite systems, whereas the scaling is unfavorable to accurately approximate infinite 3D systems. In future work, we plan to apply these methods to study collectively enhanced as well as suppressed decay in magic wavelength lattices for clock atoms. The simulations should also provide us with predictions of geometries and excitation schemes to minimize dipole-dipole induced shifts in order to improve the accuracy of atomic clocks. Possible approaches would be to analyze different geometries, use initial phase spread rotations and spin squeezing. As an interesting extension of this model we also want to embed such spin systems inside a cavity and derive corresponding mean-field and MPC equations for the arising infinite range interactions. This should give us a basis to simulate superradiant lasers for larger ensembles including their interaction. Note, that as we are simulating an open system anyway, including a finite bath temperature will hardly change the complexity of these calculations and could be used to identify temperature dependent phase transitions in the system.

ACKNOWLEDGMENTS

This work has been supported by the Austrian Science Fund FWF through the SFB F4013 FoQuS.

---

[1] W. Heisenberg, Zeitschrift für Physik **49**, 619 (1928).

[2] H. B. Thacker, Reviews of Modern Physics **53**, 253 (1981).

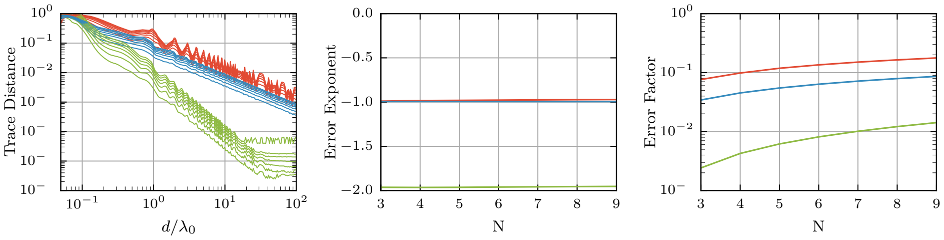

FIG. 9. Dependence analysis of the time-maximum trace distance between results of the master equation and results of an independent evolution (red), mean-field (blue) and MPC (green) on the spin distance of a chain consisting of $N = 3 \dots 9$ spins. Higher spin numbers correspond to slightly increased trace distances (a). An approximation of the trace distances by $C_N * d^{k_N}$ results in the spin-number dependency of the error-exponent k_N (b) and the error-factor C_N (c).

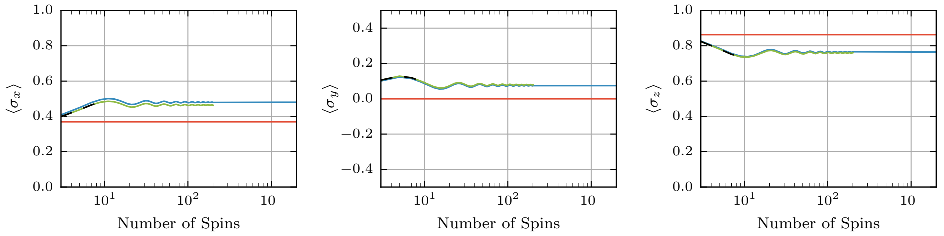

FIG. 10. Expectation values of the Pauli operators $\langle\sigma_x\rangle$, $\langle\sigma_y\rangle$ and $\langle\sigma_z\rangle$ of the central spin in a chain consisting of N spins with distance $d = 0.9\lambda_0$ after a time evolution for $2\gamma^{-1}$. Initially all spins are in the state $\langle\sigma_x\rangle = 1$ and the system is solved for independent spins (red), using mean-field (blue), MPC (green) and the master-equation (dashed black).

[3] M. E. Fisher, American Journal of Physics **32**, 343 (1964).
[4] F. Haldane, Physical Review Letters **50**, 1153 (1983).
[5] P. Van Dongen and D. Vollhardt, Physical review letters **65**, 1663 (1990).
[6] P. A. Pearce and C. J. Thompson, Comm. Math. Phys. **58**, 131 (1978), URL `http://projecteuclid.org/euclid.cmp/1103901439`.
[7] A. Georges, G. Kotliar, W. Krauth, and M. J. Rozenberg, Reviews of Modern Physics **68**, 13 (1996).
[8] K. Byczuk and D. Vollhardt, Physical Review B **77**, 235106 (2008).
[9] E. Altman, W. Hofstetter, E. Demler, and M. D. Lukin, New Journal of Physics **5**, 113 (2003).
[10] M. Lewenstein, A. Sanpera, V. Ahufinger, B. Damski, A. Sen, and U. Sen, Advances in Physics **56**, 243 (2007).
[11] A. Micheli, G. Brennen, and P. Zoller, Nature Physics **2**, 341 (2006).
[12] Z. Ficek, R. Tanas, and S. Kielich, Optica Acta **33**, 1149 (1986).
[13] H. Zoubi and H. Ritsch, Advances in Atomic, Molecular, and Optical Physics **62**, 171 (2013).
[14] H. Zoubi and H. Ritsch, EPL (Europhysics Letters) **87**, 23001 (2009).
[15] C. Gardiner and P. Zoller, *Quantum noise: a handbook of Markovian and non-Markovian quantum stochastic methods with applications to quantum optics*, vol. 56 (Springer Science & Business Media, 2004).
[16] L. Pollet, J. Picon, H. Büchler, and M. Troyer, Physical review letters **104**, 125302 (2010).
[17] M. Takamoto, F.-L. Hong, R. Higashi, and H. Katori, Nature **435**, 321 (2005).
[18] A. D. Ludlow, T. Zelevinsky, G. Campbell, S. Blatt, M. Boyd, M. H. de Miranda, M. Martin, J. Thomsen, S. M. Foreman, J. Ye, et al., Science **319**, 1805 (2008).
[19] X. Zhang, M. Bishof, S. Bromley, C. Kraus, M. Safronova, P. Zoller, A. Rey, and J. Ye, science **345**, 1467 (2014).
[20] L. Ostermann, H. Zoubi, and H. Ritsch, Optics express **20**, 29634 (2012).
[21] T. Maier, S. Kraemer, L. Ostermann, and H. Ritsch, Optics express **22**, 13269 (2014).
[22] M. Martin, M. Bishof, M. Swallows, X. Zhang, C. Benko, J. Von-Stecher, A. Gorshkov, A. Rey, and J. Ye, Science **341**, 632 (2013).
[23] S. Gopalakrishnan, B. Lev, and P. Goldbart, Bulletin of the American Physical Society **57** (2012).
[24] L. Ostermann, H. Ritsch, and C. Genes, Physical review letters **111**, 123601 (2013).
[25] J. G. Bohnet, Z. Chen, J. M. Weiner, D. Meiser, M. J. Holland, and J. K. Thompson, Nature **484**, 78 (2012).
[26] K. Henschel, J. Majer, J. Schmiedmayer, and H. Ritsch, Physical Review A **82**, 033810 (2010).

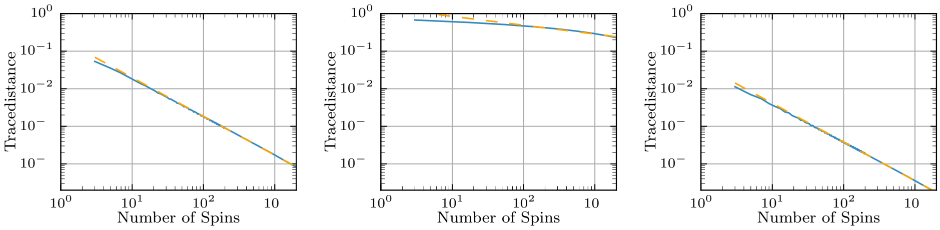

FIG. 11. Time-maximum of the trace-distance between the reduced density matrix of the central spin state in a chain consisting of N spins compared to the chain consisting of $N_{\max}^{\text{meanfield}} = 20001$ (blue) where both quantities are results of mean-field simulations. Approximation of this trace-distance by $C_d * N^{k_d}$ (dashed yellow) for different spin-spin distances $d = 0.7\lambda_0$(a), $d = 1.0\lambda_0$(b) and $d = 3.7\lambda_0$(c)

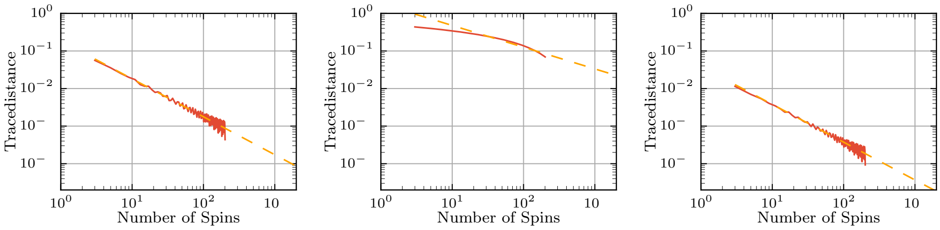

FIG. 12. Time-maximum of the trace-distance between the reduced density matrix of the central spin in a chain consisting of N spins compared to the chain consisting of $N_{\max}^{\text{MPC}} = 401$ (blue) where both quantities are results of MPC simulations for different spin-spin distances $d = 0.7\lambda_0$(a), $d = 1.0\lambda_0$(b) and $d = 3.7\lambda_0$(c). Approximation of this trace-distance by $C_d * N^{k_d}$ (dashed yellow).

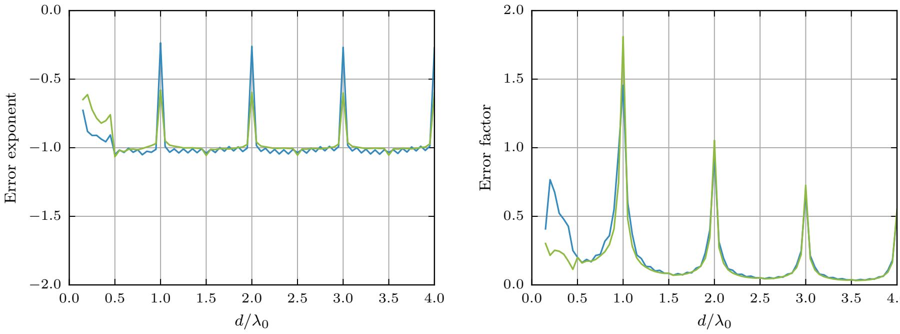

FIG. 13. Error exponent k_d and Error factor C_d dependence on the spin-spin distance determined in the previous fits $C_d * N^{k_d}$ using mean-field (blue) and MPC (green) in the case of a chain.

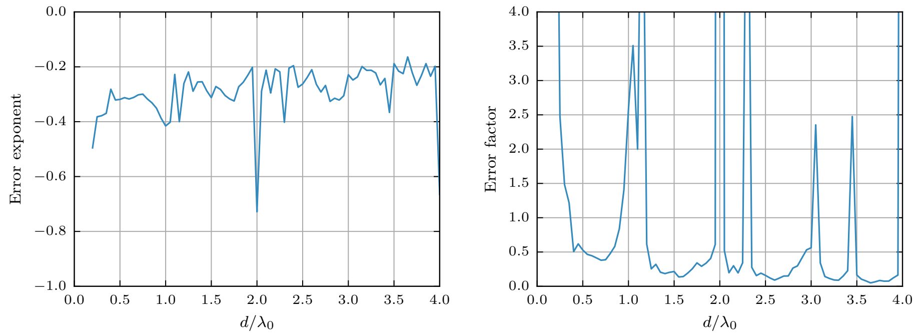

FIG. 14. Error exponent k_d and error factor C_d dependence on the spin-spin distance determined in the previous fits $C_d * N^{k_d}$ using mean-field in the case of a hexagonal lattice.

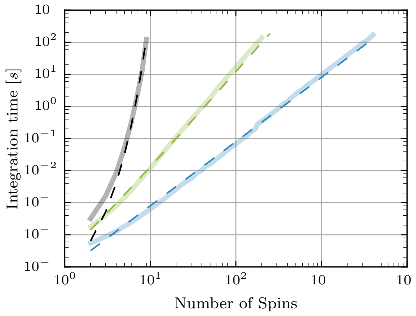

FIG. 15. Time needed to integrate a spin chain consisting of N spins from 0 to γ^{-1} on a single CPU. The solid lines are the result of the benchmarks for master (black), MPC (green) and mean-field (blue), the dashed lines are the corresponding theoretical predictions.

7. Publication: Optimized geometries for future generation optical lattice clocks

Optimized geometries for future generation optical lattice clocks

S. Krämer, L. Ostermann, and H. Ritsch
Institute for Theoretical Physics, Universität Innsbruck, Technikerstraße 21/3, 6020 Innsbruck, Austria

Atoms deeply trapped in magic wavelength optical lattices provide a Doppler- and collision-free dense ensemble of quantum emitters ideal for high precision spectroscopy. Thus, they are the basis of some of the best optical clock setups to date. However, despite their minute optical dipole moments the inherent long range dipole-dipole interactions in such lattices generate line shifts, dephasing and modified decay. We show that in a perfectly filled lattice these effects are resonantly enhanced depending on lattice constant, lattice geometry and excitation scheme inducing clock shifts of many atomic linewidths and reducing measurement precision via superradiance. However, under optimal conditions collective effects can be exploited to yield zero effective shifts and prolong dipole lifetimes beyond the single atom decay. In particular we identify 2D hexagonal or square lattices with lattice constants below the optical wavelength as most promising configurations for an accuracy and precision well below the independent ensemble limit. This geometry should also be an ideal basis for related applications such as superradiant lasers, precision magnetometry or long lived quantum memories.

Since the turn of the century the technology of manipulating and controlling ultracold atoms with lasers has seen breathtaking advances [1–3]. Following the seminal first demonstration of a quantum phase transition in an optical lattice [4], nowadays the so-called Mott insulator state can be prepared routinely [5, 6]. Experiments with photo-associated ultracold molecules have reached a comparable control [7–10] and coherent interactions between the atoms at neighboring sites can be tailored [11].

For some of the world's best optical clocks [12–14], atoms with a long-lived clock transition are prepared in an optical lattice using a differential light shift free (magic) trapping wavelength [15, 16]. In principle, this provides for a Doppler and collision free dense ensemble with negligible inhomogeneous broadening. However, when excited optically emitters will nevertheless interact via long range resonant dipole-dipole coupling [17].

Here we show that at sufficient densities the dipole interaction strength surpasses the excited state lifetime and collective excitations analogous to excitons appear [18]. For polar molecules in optical lattices they even dominate the dynamics [19] and allow for studying generic phenomena of solid state physics [1]. For clock transitions the extremely tiny dipole moment keeps these interactions small in absolute magnitude. Still, the exciton's effective transition frequencies and their spontaneous decay is governed by dipole-dipole interaction [20] deviating from the bare atom case. This limits accuracy and precision of corresponding clock setups. In an idealized Ramsey sequence for a clock setup, the first laser pulse creates a product state of all atoms prepared in a 50% superposition of ground and excited state with equal phase and all dipoles aligned in parallel. This state features the maximally possible dipole moment and typically exhibits superradiance. Even a tiny single particle spontaneous emission rate can be that strongly enhanced, that collective decay becomes a dominant factor limiting measurement time and precision [21]. In current setups based on 1D lattices with low filling this perturbation is often negligible compared to other noise like collisions, black body shifts or reference cavity fluctuations. However, in lattices with unit filling, dipole-dipole interaction shifts are larger than the atomic linewidth and constitute a significant inherent perturbation. Note that their absolute magnitude scales with the atomic dipole moment and thus strongly depends on the chosen transition.

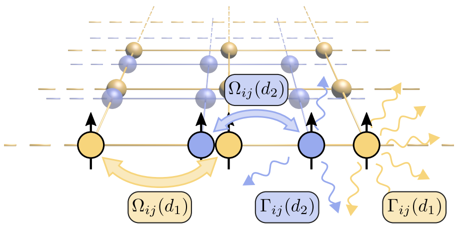

FIG. 1. (Color online) Scheme of a 2D optical lattice filled with clock atoms interacting via dipole-dipole energy exchange Ω_{ij} and a collectively modified spontaneous emission Γ_{ij} at two different lattice constants shown in blue and yellow. In a mean field treatment with translation invariance the sum over all interaction terms yields two effective couplings Ω^{eff} and Γ^{eff} only, which govern the approximate system dynamics.

As a key quantity to capture the collective modifications of the system dynamics, we use the decay and phase shift of the collective dipole generated by the first Ramsey pulse, which determines the contrast and shift of the central Ramsey fringes. Note, that due to the pairwise nature of dipole-dipole interactions a rephasing pulse cannot correct these errors. Here we ignore interaction induced perturbations during the Ramsey pulses, which introduce extra noise but could be reduced by very fast pulses or improved sequences [22].

For this we numerically solve the well established master equation for the atomic density matrix ρ including optical dipole-dipole interaction obtained by tracing over the electromagnetic vacuum field [17, 23, 24],

$$\dot{\rho} = i\,[\rho, H] + \mathcal{L}[\rho]. \tag{1}$$

As previously shown for small atom numbers ($N < 12$) a numerical solution of the full master equation yields non-negligible shifts already [20, 25]. As the Hilbert space grows exponentially with atom number, the full equation cannot be solved for ensembles of a realistic size. Since for precision measurements we need to evaluate collective effects precisely, reliable and converging alternative numerical methods are required. For larger ensembles at low densities a cluster approach has produced first estimates of the scaling of the dephasing with the system's size and density [12]. Recently, important self synchronization effects through dipole coupling were studied in a very high density limit using simplifying assumptions for the coupling [26].

In this letter we present an extensive analysis of the collective dynamics for fully populated lattices of different geometries and sizes containing a large or even an infinite number of particles. Our primary goal is to estimate the magnitude of the dipole phase shift and collective decay as a function of lattice and excitation geometry. Besides a resonant enhancement of shifts, decay and dephasing, we find cases where collective effects lead to improvements of the maximally achievable measurement precision beyond the independent particle level by virtue of subradiant states. We concentrate on an idealized setup ignoring lattice shifts, thermal effects or the hopping of atoms.

Numerically we apply an enhanced mean field approach whose validity has been extensively tested in recent work [27], which we can scale to realistic numbers up to $N \approx 10^5$ particles. If the particle distribution exhibits symmetries numbers up to even 10^{10} are possible, well approximating infinite systems in 1D and 2D. Its accuracy, however, breaks down at very close distances as it cannot capture higher order correlations. Similar deliberations for classical dipoles have recently been put forward [28].

Model – We consider an ensemble of N identical effective two-level atoms with transition frequency ω_0 and inverse lifetime γ at positions r_i ($i = 1..N$) interacting via optical dipole-dipole coupling described by the Hamiltonian [17, 24]

$$H = \sum_{ij;i\neq j} \Omega_{ij}(r_{ij})\sigma_i^+\sigma_j^- . \tag{2}$$

Here, $\sigma_i^{\pm}$ denotes the raising (lowering) operator of the i-th atom and $\Omega_{ij} = \frac{3}{4}\gamma G\left(k_0 r_{ij}\right)$ represents the energy exchange with $k_0 = \omega_0/c = 2\pi/\lambda_0$ and $r_{ij} = |r_i - r_j|$ being the distance between atoms i and j. Collective spontaneous emission is accounted for by a Liouvillian of the form [17, 23]

$$\mathcal{L}[\rho] = \frac{1}{2}\sum_{i,j}\Gamma_{ij}(r_{ij})(2\sigma_i^-\rho\sigma_j^+ - \sigma_i^+\sigma_j^-\rho - \rho\sigma_i^+\sigma_j^-), \tag{3}$$

where the off-diagonal rates $\Gamma_{ij} = \frac{3}{2}\gamma F\left(k_0 r_{ij}\right)$ introduce super- and subradiant decay [24]. Explicitly we have

$$F(\xi) = \alpha\frac{\sin\xi}{\xi} + \beta\left(\frac{\cos\xi}{\xi^2} - \frac{\sin\xi}{\xi^3}\right) \tag{4a}$$

$$G(\xi) = -\alpha\frac{\cos\xi}{\xi} + \beta\left(\frac{\sin\xi}{\xi^2} + \frac{\cos\xi}{\xi^3}\right) \tag{4b}$$

with $\alpha = 1 - \cos^2\theta$ and $\beta = 1 - 3\cos^2\theta$, where θ represents the angle between the line connecting atoms i and j and the common atomic dipole orientation.

Mean field approximation – To study large particle numbers we derive the equations of motion for the expectation values of the Pauli operators for the k-th atom as detailed in the appendix A. Assuming a separable density operator and factorizing the two-particle correlations via $\langle\sigma_i^\mu\sigma_j^\nu\rangle \approx \langle\sigma_i^\mu\rangle\langle\sigma_j^\nu\rangle$ for μ, $\nu \in \{x, y, z\}$ they transform to a closed set. As shown previously [27] these equations still capture the major part of the interaction up to a moderate interaction strength. For more accurate studies one may add second order corrections increasing the computational effort.

Symmetric configurations – For symmetric geometries with each atom initially in the same state and subject to the same effective interactions, the equations of motion for all particles become identical and read

$$\langle\dot{\sigma^x}\rangle = \Omega^{\text{eff}}\langle\sigma^y\rangle\langle\sigma^z\rangle - \frac{1}{2}\Big(\gamma - \Gamma^{\text{eff}}\langle\sigma^z\rangle\Big)\langle\sigma^x\rangle, \tag{5a}$$

$$\langle\dot{\sigma^y}\rangle = -\Omega^{\text{eff}}\langle\sigma^x\rangle\langle\sigma^z\rangle - \frac{1}{2}\Big(\gamma - \Gamma^{\text{eff}}\langle\sigma^z\rangle\Big)\langle\sigma^y\rangle, \tag{5b}$$

$$\langle\dot{\sigma^z}\rangle = -\gamma\big(1 + \langle\sigma^z\rangle\big) - \frac{1}{2}\Gamma^{\text{eff}}\Big(\langle\sigma^x\rangle^2 + \langle\sigma^y\rangle^2\Big). \tag{5c}$$

Hence instead of solving a huge set of coupled nonlinear equations we need to determine the effective couplings, i.e.

$$\Omega^{\text{eff}} = \sum_{j=2}^{N}\Omega_{1j} \qquad \Gamma^{\text{eff}} = \sum_{j=2}^{N}\Gamma_{1j}, \tag{6}$$

Of course, such a rigorous symmetry condition is fulfilled for very few atomic distributions only. Then, the essence of the interactions within the entire lattice is captured solely by two real numbers, the effective coupling Ω^{eff} and the collective decay rate Γ^{eff}. In a clock setup one seeks to minimize the energy shifts Ω^{eff} and find configurations with a maximally negative Γ^{eff}, minimizing decay and allowing for an as long as possible interrogation time.

Finite systems – Firstly, for finite symmetric configurations the effective quantities can be calculated easily. The most obvious symmetric structures are regular polygons. This might not be the most practical example but nicely displays the underlying physics. In Fig. 2 we compare the parameters for a square, a ten-sided and a 100000-sided polygon. The square shows a behavior quite similar to the underlying functions $F(\xi)$ and $G(\xi)$, while the two larger polygons exhibit strong size dependent variations, particularly at integral values of $d\lambda_0$ emerging from the accumulation of many $1/\xi$ contributions. Note that even with a relatively large atom spacing, cooperative collective effects are sizable and vary strongly with distance.

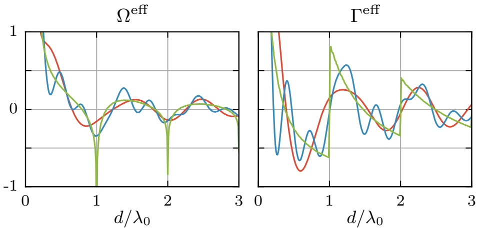

FIG. 2. (Color online) Distance dependence of the effective dipole coupling Ω^{eff} and Γ^{eff} for a square (red), a ten-sided (blue) and a 100000-sided (green) regular polygon. The fewer particles the closer the functions resemble the underlying couplings Ω_{ij} and Γ_{ij}. The divergences at integral d/λ_0 result from the $1/\xi$ terms in $F(\xi)$ and $G(\xi)$.

Infinite systems – In practice, extended regular systems, i.e. large periodic lattices, are experimentally more relevant. Fig. 3 depicts the effective couplings for an infinite chain, a square lattice and a hexagonal lattice. For comparison, we have overlaid the results for smaller atom numbers to demonstrate finite size effects. We observe stronger variations and again divergences at integral values of d/λ_0 . These manifest themselves in a much more pronounced way at huge atom numbers and therefore underpin the importance of properly treating long range interactions.

Note that for the two-dimensional square lattice and the hexagonal lattice Γ^{eff} exhibits a broad minimum for the effective decay close to $\Gamma^{\text{eff}} = -1$ for $d < \lambda_0$, where atomic decay is strongly inhibited. This favors such two-dimensional setups for lattice clocks as subradiant decay will dominate the system dynamics allowing for much longer Ramsey delay times and thus offering a higher overall precision [21]. Similarly we can identify lattice constants with a zero effective shift increasing clock accuracy. Extending these calculations to three dimensional lattices, we find that the necessary atom numbers to obtain smooth converging behavior are beyond our current numerical capabilities. For particle numbers of about 10^{12} the resulting effective quantities still fluctuate strongly, predicting potential problems for such 3D clock setups. A demonstration of this effect can be found in the appendix C.

Tailoring atomic excitations – So far we assumed a phase-symmetric excitation of all atoms by the first Ramsey pulse. In a practical excitation scheme this corresponds to illumination at right angle. In general, however, the effective couplings Ω^{eff} and Γ^{eff} will change, when we allow for a local phase shift imprinted on the atoms. In a $\pi/2$ Ramsey sequence [29] the excitation phase appears on the excited state directly, i.e.

$$|\Psi\rangle = \bigotimes_{j=1}^{N} \frac{1}{\sqrt{2}} \Big(|g\rangle + e^{i\Delta\phi(j-1)} |e\rangle \Big) . \tag{7}$$

In our treatment we can exploit the system's symmetry and absorb this phase into the effective couplings (Appendix B). For $\Delta\phi = 0$ we recover the above results. The closer the phase shift gets to $\Delta\phi = \pi$, however, the more half-integral values of $d\lambda_0$ yield minimal shifts and the maximally negative Γ^{eff} as seen in Fig. 4. Since the emitted light has interfered constructively at integral and destructively at half-integral distances for $\Delta\phi = 0$, it will do exactly the opposite at $\Delta\phi = \pi$. Furthermore, addressing atoms transversally ($\Delta\phi = 0$) seems more favorable at typical magic wavelength trapping distances, e.g. $d/\lambda_0 \approx 0.58$ for ^{87}Sr [15, 20, 30]. Again, for $d \ll \lambda_0$ the mean field approach breaks down and one should rather turn to the Dicke model [31], reducing N two-level emitters to one effective spin $N/2$-system [26]. Let us finally discuss the consequences for typical cases. Fig. 5 shows the time evolution of the average spin for an infinite chain initialized in a symmetric Ramsey state with either no phase shift or a phase shift of $\Delta\phi = \pi$ between neighboring atoms. The lattice constants have been chosen to be approximately $\lambda_0/2$ as would be typical [5]. We refrain from choosing exactly $\lambda_0/2$ to avoid the $1/\xi$ divergence. We observe that the dipoles' lifetimes vary strongly, comparing the subradiant behavior (red) where the collective dipole lives much longer than the natural lifetime of the atom to the superradiant (green) regime where the excitation vanishes very quickly. Additionally, to highlight the validity of the mean field approach, we add the results of a second order expansion simulation. Corresponding results for a full Ramsey sequence are shown in the appendix D.

Conclusions – In densely filled optical lattices dipole-dipole interaction and collective decay significantly change the evolution of an induced collective dipole. Due to the long range-nature of the coupling, sizable shifts appear even for long lived clock states despite their minute dipole moment, which limits accuracy and precision of Ramsey spectroscopy. Shifts and dephasing in large systems strongly depend on the dimensionality and geometry of the lattice, exhibiting resonant enhancements at particular lattice constants. While at current operating densities for Strontium [12–14] these shifts are smaller than other technical imperfections, they constitute inherent fundamental perturbations even in perfectly filled lattice clocks.

We have identified optimal operation geometries, which combine a negligible effective shift with a strong suppression of decay. In particular, for a 1D lattice with a tailored excitation angle and for a 2D hexagonal lattice favorable operation parameters for future generation clock setups were found. In this sense it seems possible to implement a high density dark exciton based atomic clock geometry with shifts many orders of magnitude be-

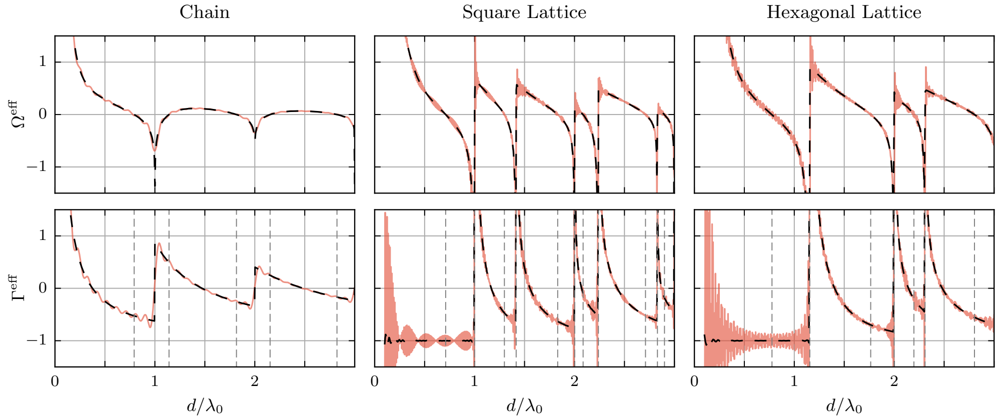

FIG. 3. (Color online) Distance dependence of the effective quantities Ω^{eff} and Γ^{eff} for an infinite equidistant chain, a square lattice and a hexagonal lattice (dashed black) compared to their not yet converged finite counterparts of 10, $4 * 10^4$ and 10^5 particles respectively (solid red). Again, we find divergences at integral d/λ_0 owing to the $1/\xi$-terms in $F(\xi)$ and $G(\xi)$. In the 2D configurations Γ^{eff} plateaus at -1 for $d < \lambda_0$, suggesting that this parameter range will be the most favorable for clock setups as decay is strongly suppressed.

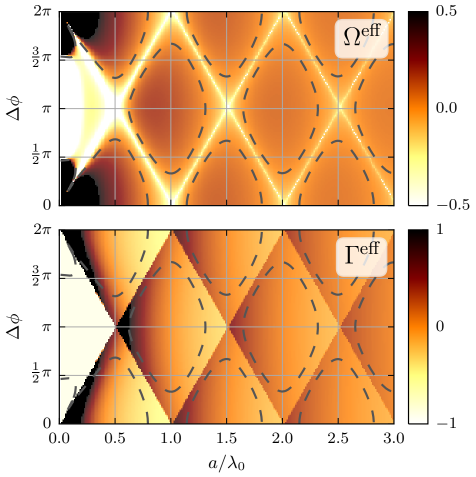

FIG. 4. (Color online) Effective interactions Ω^{eff} and Γ^{eff} for an infinite chain with spacing a where the spins are initially prepared with phase shift $\Delta\phi$ between neighboring spins. The dashed lines indicates parameters with $\Omega^{\text{eff}} = 0$ optimal for an optical clock.

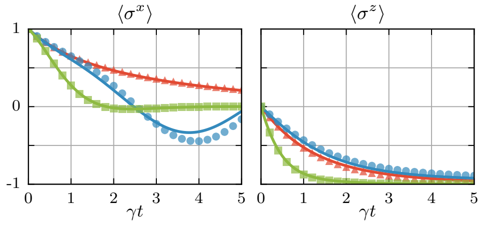

FIG. 5. (Color online) Three different examples for the time evolution of the spin expectation values for a chain with spacing d where initially all spins are prepared in a coherent superposition of ground and excited state with a phase shift of $\Delta\phi$. The parameters used are $d = 0.792\lambda_0$ with $\Delta\phi = 0$ (red triangles), where $\Omega^{\text{eff}} = 0$ and Γ^{eff} is nearly optimal, as well as $d = 0.49\lambda_0$ (green squares) and $d = 0.51\lambda_0$ (blue circles), both with $\Delta\phi = \pi$ which are close to a Γ^{eff} discontinuity. The solid lines correspond to a solution of a second order cumulant expansion model with 200 particles and demonstrate a very good agreement with the infinite mean field description.

low a single Hz and almost unlimited exciton life times. In 3D the interactions are particularly sensitive to the lattice constant and boundary effects, which dominate even for billions of particles rendering such setups very challenging.

While for most considerations we have focused on the case of clock transitions, the same physics is present in a more prominent and experimentally easier observable form for broader transitions. Optimizing geometries will also be relevant for devices such as superradiant lasers [32, 33] or lattice based optical memories.

ACKNOWLEDGMENTS

Acknowledgments – The authors acknowledge funding by the Austrian Science Fund FWF project SFB FoQus F4006-N13 (S.K., H.R.) and the DARPA QUASAR project (L.O., H.R.).

---

[1] I. Bloch, J. Dalibard, and S. Nascimbène, Nature Physics **8**, 267 (2012).
[2] M. Lewenstein, A. Sanpera, V. Ahufinger, B. Damski, A. Sen, and U. Sen, Advances in Physics **56**, 243 (2007).
[3] A. Micheli, G. Brennen, and P. Zoller, Nature Physics **2**, 341 (2006).
[4] M. Greiner, O. Mandel, T. Esslinger, T. W. Hänsch, and I. Bloch, nature **415**, 39 (2002).
[5] I. Bloch, Nature Physics **1**, 23 (2005).
[6] W. S. Bakr, J. I. Gillen, A. Peng, S. Fölling, and M. Greiner, Nature **462**, 74 (2009).
[7] C. Ospelkaus, S. Ospelkaus, L. Humbert, P. Ernst, K. Sengstock, and K. Bongs, Physical Review Letters **97**, 120402 (2006).
[8] L. D. Carr, D. DeMille, R. V. Krems, and J. Ye, New Journal of Physics **11**, 055049 (2009).
[9] J. G. Danzl, M. J. Mark, E. Haller, M. Gustavsson, R. Hart, J. Aldegunde, J. M. Hutson, and H.-C. Nägerl, Nature Physics **6**, 265 (2010).
[10] B. Yan, S. A. Moses, B. Gadway, J. P. Covey, K. R. Hazzard, A. M. Rey, D. S. Jin, and J. Ye, Nature **501**, 521 (2013).
[11] L.-M. Duan, E. Demler, and M. Lukin, Physical Review Letters **91**, 090402 (2003).
[12] M. Martin, M. Bishof, M. Swallows, X. Zhang, C. Benko, J. Von-Stecher, A. Gorshkov, A. Rey, and J. Ye, Science **341**, 632 (2013).
[13] I. Ushijima, M. Takamoto, M. Das, T. Ohkubo, and H. Katori, arXiv preprint arXiv:1405.4071 (2014).
[14] X. Zhang, M. Bishof, S. Bromley, C. Kraus, M. Safronova, P. Zoller, A. Rey, and J. Ye, science **345**, 1467 (2014).
[15] M. Takamoto, F.-L. Hong, R. Higashi, and H. Katori, Nature **435**, 321 (2005).
[16] A. D. Ludlow, T. Zelevinsky, G. Campbell, S. Blatt, M. Boyd, M. H. de Miranda, M. Martin, J. Thomsen, S. M. Foreman, J. Ye, et al., Science **319**, 1805 (2008).
[17] Z. Ficek, R. Tanas, and S. Kielich, Optica Acta **33**, 1149 (1986).
[18] H. Zoubi and H. Ritsch, Advances in Atomic, Molecular, and Optical Physics **62**, 171 (2013).
[19] L. Pollet, J. Picon, H. Büchler, and M. Troyer, Physical review letters **104**, 125302 (2010).
[20] L. Ostermann, H. Zoubi, and H. Ritsch, Optics express **20**, 29634 (2012).
[21] L. Ostermann, H. Ritsch, and C. Genes, Physical review letters **111**, 123601 (2013).
[22] V. Yudin, A. Taichenachev, C. Oates, Z. Barber, N. Lemke, A. Ludlow, U. Sterr, C. Lisdat, and F. Riehle, Physical Review A **82**, 011804 (2010).
[23] C. Gardiner and P. Zoller, *Quantum noise: a handbook of Markovian and non-Markovian quantum stochastic methods with applications to quantum optics*, vol. 56 (Springer Science & Business Media, 2004).
[24] R. Lehmberg, Physical Review A **2**, 883 (1970).
[25] D. Chang, J. Ye, and M. Lukin, Physical Review A **69**, 023810 (2004).
[26] B. Zhu, J. Restrepo, A. M. Rey, and M. Holland, in *APS Division of Atomic, Molecular and Optical Physics Meeting Abstracts* (2014), vol. 1, p. 1022.
[27] S. Krämer and H. Ritsch, arXiv preprint arXiv:1504.08279 (2015).
[28] R. J. Bettles, S. A. Gardiner, and C. S. Adams, arXiv preprint arXiv:1410.4776 (2014).
[29] S. Haroche and J. M. Raimond, *Exploring the quantum* (Oxford Univ. Press, 2006).
[30] G. K. Campbell, A. D. Ludlow, S. Blatt, J. W. Thomsen, M. J. Martin, M. H. de Miranda, T. Zelevinsky, M. M. Boyd, J. Ye, S. A. Diddams, et al., Metrologia **45**, 539 (2008).
[31] R. H. Dicke, Physical Review **93**, 99 (1954).
[32] J. G. Bohnet, Z. Chen, J. M. Weiner, D. Meiser, M. J. Holland, and J. K. Thompson, Nature **484**, 78 (2012).
[33] T. Maier, S. Kraemer, L. Ostermann, and H. Ritsch, Optics express **22**, 13269 (2014).

Appendix A: Derivation of the mean field equations

Starting from the full multiparticle density operator ρ our master equation allows to obtain the following equations for the individual spin expectation values immediately

$$\dot{\langle\sigma_k^x\rangle} = \sum_{j;j\neq k} \Omega_{kj}\langle\sigma_j^y\sigma_k^z\rangle - \frac{1}{2}\gamma\langle\sigma_k^x\rangle + \frac{1}{2}\sum_{j;j\neq k}\Gamma_{kj}\langle\sigma_j^x\sigma_k^z\rangle \tag{A1a}$$

$$\dot{\langle\sigma_k^y\rangle} = \sum_{j;j\neq k} \Omega_{kj}\langle\sigma_j^x\sigma_k^z\rangle - \frac{1}{2}\gamma\langle\sigma_k^y\rangle + \frac{1}{2}\sum_{j;j\neq k}\Gamma_{kj}\langle\sigma_j^y\sigma_k^z\rangle \tag{A1b}$$

$$\dot{\langle\sigma_k^z\rangle} = \sum_{j;j\neq k} \Omega_{kj}\Big(\langle\sigma_j^x\sigma_k^y\rangle - \langle\sigma_j^y\sigma_k^x\rangle\Big) - \gamma\big(1+\langle\sigma_k^z\rangle\big) - \frac{1}{2}\sum_{j;j\neq k}\Gamma_{kj}\Big(\langle\sigma_j^x\sigma_k^x\rangle + \langle\sigma_j^y\sigma_k^y\rangle\Big). \tag{A1c}$$

Assuming a spatially separable state $\rho = \bigotimes_k \rho_k$ leads to the lowest order mean field equations used in the letter.

Appendix B: Mean field equations with tailored excitation phase

At zero temperature the ground state $\rho = \bigotimes_k (|g\rangle(\langle g|)_k$ is separable and in an idealized standard Ramsey procedure the first pulse would create a product state of equal weighted superpositions $\rho = \bigotimes_k 1/2\,((|g\rangle + |e\rangle)(\langle e| + \langle g|))_k$. This is the generic initial state we use in our work to study dipole-dipole interaction. In fact, this state possesses the maximal collective dipole moment and therefore shows strong interactions.

Of course, in any real setup this preparation step is not perfect as interactions are present during the excitation pulse and the excitation laser carries an intensity and phase gradient. Some of the errors can be corrected in improved excitation schemes[21, 22]. However, particularly in extended systems a phase gradient is hard to avoid and will strongly influence the system dynamics. Fortunately, one can show, that a known phase gradient will not complicate the calculations too much. If we allow for the individual atomic states to bare a spatially dependent phase of $\Delta\phi$ on the excited state, i.e. $|\psi_k\rangle = \frac{1}{\sqrt{2}}\,(|g\rangle + \exp(i\phi_k)|e\rangle)$, we can absorb this into our equations efficiently. Using the abbreviations $\Omega_{kj}^{\cos} = \Omega_{kj}\cos(\phi_k - \phi_j)$ and $\Omega_{kj}^{\sin} = \Omega_{kj}\sin(\phi_k - \phi_j)$ we obtain the following modified equations of motion

$$\frac{d}{dt}\langle\tilde{\sigma}_k^x\rangle = \sum_{j;j\neq k}\Omega_{kj}^{\sin}\langle\tilde{\sigma}_j^x\sigma_k^z\rangle + \sum_{j;j\neq k}\Omega_{kj}^{\cos}\langle\tilde{\sigma}_j^y\sigma_k^z\rangle - \frac{1}{2}\gamma\langle\tilde{\sigma}_k^x\rangle + \frac{1}{2}\sum_{j;j\neq k}\Gamma_{kj}^{\cos}\langle\tilde{\sigma}_j^x\sigma_k^z\rangle - \frac{1}{2}\sum_{j;j\neq k}\Gamma_{kj}^{\sin}\langle\tilde{\sigma}_j^y\sigma_k^z\rangle \tag{B1a}$$

$$\frac{d}{dt}\langle\tilde{\sigma}_k^y\rangle = -\sum_{j;j\neq k}\Omega_{kj}^{\cos}\langle\tilde{\sigma}_j^x\sigma_k^z\rangle + \sum_{j;j\neq k}\Omega_{kj}^{\sin}\langle\tilde{\sigma}_j^y\sigma_k^z\rangle - \frac{1}{2}\gamma\langle\tilde{\sigma}_k^y\rangle + \frac{1}{2}\sum_{j;j\neq k}\Gamma_{kj}^{\sin}\langle\tilde{\sigma}_j^x\sigma_k^z\rangle + \frac{1}{2}\sum_{j;j\neq k}\Gamma_{kj}^{\cos}\langle\tilde{\sigma}_j^y\sigma_k^z\rangle \tag{B1b}$$

$$\begin{aligned}\frac{d}{dt}\langle\sigma_k^z\rangle = &-\sum_{j;j\neq k}\Omega_{kj}^{\sin}(\langle\tilde{\sigma}_j^x\tilde{\sigma}_k^x\rangle + \langle\tilde{\sigma}_j^y\tilde{\sigma}_k^y\rangle) + \sum_{j;j\neq k}\Omega_{kj}^{\cos}(\langle\tilde{\sigma}_j^x\tilde{\sigma}_k^y\rangle - \langle\tilde{\sigma}_j^y\tilde{\sigma}_k^x\rangle)\\ &-\gamma(1+\langle\sigma_k^z\rangle) - \frac{1}{2}\sum_{j;j\neq k}\Gamma_{kj}^{\cos}(\langle\tilde{\sigma}_j^x\tilde{\sigma}_k^x\rangle + \langle\tilde{\sigma}_j^y\tilde{\sigma}_k^y\rangle) - \frac{1}{2}\sum_{j;j\neq k}\Gamma_{kj}^{\sin}(\langle\tilde{\sigma}_j^x\tilde{\sigma}_k^y\rangle - \langle\tilde{\sigma}_j^y\tilde{\sigma}_k^x\rangle).\end{aligned} \tag{B1c}$$

We see that the following definitions prove to be very helpful

$$\Omega_k^{\cos} = \sum_{j;j\neq k}\Omega_{kj}\cos(\phi_k - \phi_j) \qquad \Omega_k^{\sin} = \sum_{j;j\neq k}\Omega_{kj}\sin(\phi_k - \phi_j) \tag{B2a}$$

$$\Gamma_k^{\cos} = \sum_{j;j\neq k}\Gamma_{kj}\cos(\phi_k - \phi_j) \qquad \Gamma_k^{\sin} = \sum_{j;j\neq k}\Gamma_{kj}\sin(\phi_k - \phi_j) \tag{B2b}$$

Again, if we consider highly symmetric configurations where $\Omega^{\mathrm{f}} = \Omega_k^{\mathrm{f}}$ and $\Gamma^{\mathrm{f}} = \Gamma_k^{\mathrm{f}}$ and the rotated states are initially identical we can define the effective rotated quantities

$$\tilde{\Omega}^{\mathrm{eff}} = \Omega^{\cos} - \frac{1}{2}\Gamma^{\sin} \tag{B3}$$

$$\tilde{\Gamma}^{\mathrm{eff}} = \Gamma^{\cos} + 2\Omega^{\sin} \tag{B4}$$

which lead to a closed set of simplified effective equations as well, i.e.

$$\frac{d}{dt}\langle\tilde{\sigma}^x\rangle = \tilde{\Omega}^{\text{eff}}\langle\tilde{\sigma}^y\rangle\langle\sigma^z\rangle - \frac{1}{2}\gamma\langle\tilde{\sigma}^x\rangle + \frac{1}{2}\tilde{\Gamma}^{\text{eff}}\langle\tilde{\sigma}^x\rangle\langle\sigma^z\rangle \tag{B5a}$$

$$\frac{d}{dt}\langle\tilde{\sigma}^y\rangle = -\tilde{\Omega}^{\text{eff}}\langle\tilde{\sigma}^x\rangle\langle\sigma^z\rangle - \frac{1}{2}\gamma\langle\tilde{\sigma}^y\rangle + \frac{1}{2}\tilde{\Gamma}^{\text{eff}}\langle\tilde{\sigma}^y\rangle\langle\sigma^z\rangle \tag{B5b}$$

$$\frac{d}{dt}\langle\sigma^z\rangle = -\gamma\big(1+\langle\sigma^z\rangle\big) - \frac{1}{2}\tilde{\Gamma}^{\text{eff}}\Big(\langle\tilde{\sigma}^x\rangle^2 + \langle\tilde{\sigma}^y\rangle^2\Big) \tag{B5c}$$

Note that such a phase gradient tends to mix the real and imaginary part of the interaction terms.

Appendix C: Effective quantities for cubic lattices in 3D

In a cubic 3D lattice the number of neighbors at a given distance r grows approximately as r^2. Hence, one cam expect a slower convergence with distance. This problem is increased as the number of emitters to be considered grows with the third power of the system size. In contrast to 1D and 2D, together these two scalings prevent a convergence of the effective interaction parameters in the range of tractable lattices sizes of up to $N = (10^4)^3 = 10^{12}$ sites. Anyway, this is beyond experimentally realistic atom numbers so that we have to live with finite size effects.

In order to demonstrate the very slow convergence of the infinite range mean field model, we present some typical intermediate result for a 3D cubic lattice. In Fig. 6 we depict the effective coupling strengths Ω^{eff} and Γ^{eff} for the innermost two-level system in a cubic lattice of about $8 \cdot 10^9$ particles, i.e. 2000 particles in each direction. We obtain strong and very rapid oscillations of the shifts as a function of the lattice constant. Notice, that $1/r$-contributions as discussed in the letter will show up for planar and cubic diagonal distances of $\sqrt{2} \cdot r$ and $\sqrt{3} \cdot r$ as well. Increasing the atom number further still leads to changes of this pattern, so no final conclusions about physical properties and the behavior of a 3D cubic lattice can be obtained. However, perturbations of up to an order of magnitude larger than the linewidth as well as strong finite size shifts can be expected. In this case it is difficult to suggest an optimal lattice constant for a clock setup, except for avoiding certain resonances and choosing a region of about $d \approx 3\lambda/4$.

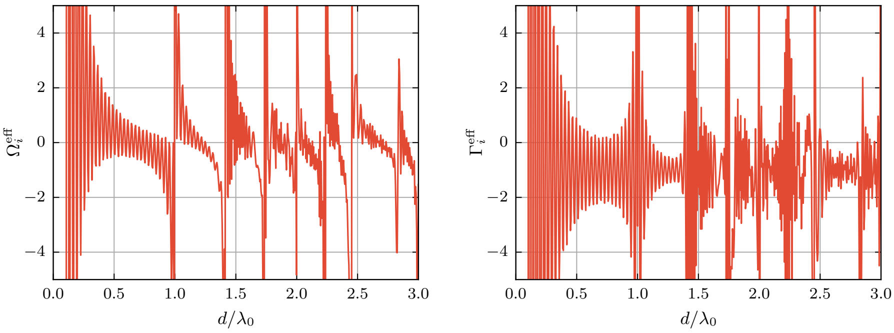

FIG. 6. Effective quantities Ω_i^{eff} and Γ_i^{eff} as experienced for the innermost spin inside a cube consisting of 2001 × 2001 × 2001 spins in a cubic lattice configuration depending on the lattice spacing d. Even for very small changes of the lattice spacing the mean net-effect of all other spins will change dramatically.

Appendix D: Ramsey spectroscopy

The effective coupling and decay parameters $\Omega^{\text{eff}}, \Gamma^{\text{eff}}$ characterize the interaction induced perturbation of the individual spin dynamics. Consequently, they will alter the Ramsey signal by introducing shifts of the fringes and modifications of the maximally obtainable contrast. As the actual connection between the magnitude of these effective couplings and their quantitative effect on the signal is nontrivial, we demonstrate the alterations of the Ramsey signal in the following examples. Using the previously derived equations of motion, it is straight forward to simulate the results of an ideal Ramsey sequence. By starting with a $\pi/2$-pulse all spins are rotated into the x-direction of the Bloch sphere. For a time γt the system evolves according to the equations

$$\langle \dot{\sigma}^x \rangle = -\Delta_a \langle \sigma_k^y \rangle + \Omega^{\text{eff}} \langle \sigma^y \rangle \langle \sigma^z \rangle - \frac{1}{2}\gamma \langle \sigma^x \rangle + \frac{1}{2}\Gamma^{\text{eff}} \langle \sigma^x \rangle \langle \sigma^z \rangle \tag{D1a}$$

$$\langle \dot{\sigma}^y \rangle = \Delta_a \langle \sigma_k^x \rangle - \Omega^{\text{eff}} \langle \sigma^x \rangle \langle \sigma^z \rangle - \frac{1}{2}\gamma \langle \sigma^y \rangle + \frac{1}{2}\Gamma^{\text{eff}} \langle \sigma^y \rangle \langle \sigma^z \rangle \tag{D1b}$$

$$\langle \dot{\sigma}^z \rangle = -\gamma\big(1 + \langle \sigma^z \rangle\big) - \frac{1}{2}\Gamma^{\text{eff}} \Big(\langle \sigma^x \rangle^2 + \langle \sigma^y \rangle^2 \Big) \tag{D1c}$$

where $\Delta_a = \omega_0 - \omega_L$ is the detuning between the probe laser and the atomic transition frequency. After this free evolution a second $\pi/2$-pulse is applied and, finally, the expectation value of σ^z is measured. For a given system characterized by the effective quantities Ω^{eff} and Γ^{eff} the result of this measurement depends on the waiting time as well as on the detuning Δ_a. In Fig. 7 the outcome of this numerical experiment is shown for three different realistic sets of effective quantities. The decisive quantity for the accuracy with regards to atomic clocks is the shift of the fringes due to the dipole-dipole interaction which can be obtained by measuring the shift of the maxima of the Ramsey fringes. The shifts for the chosen examples are shown in Fig. 8. On the other hand the slope of the fringes at their roots is the determining factor for the best achievable experimental precision. The numerical results are shown in Fig. 9. As seen in Fig. 10 the maximal shifts depend on Ω^{eff} only, while the maximal slope at zero points is governed by Γ^{eff}. For realistic values for the effective quantities this means the accuracy can be limited to γ and the achievable precision can vary by a factor of 5.

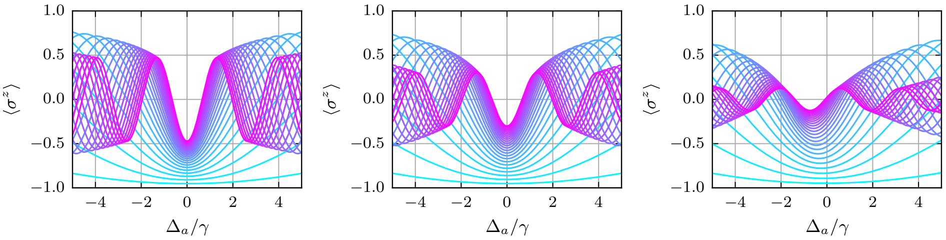

FIG. 7. Simulated idealized Ramsey spectroscopy for different sets of effective cooperative interaction strengths, from left to right: subradiant case without shift ($\Omega^{\text{eff}} = 0, \Gamma^{\text{eff}} = -0.75$), independent atom limit ($\Omega^{\text{eff}} = 0, \Gamma^{\text{eff}} = 0$) and superradiant case with shift ($\Omega^{\text{eff}} = 1, \Gamma^{\text{eff}} = 1$). The colors indicate the free evolution time with cyan representing a very short time and magenta meaning times up to $2.5\gamma^{-1}$.

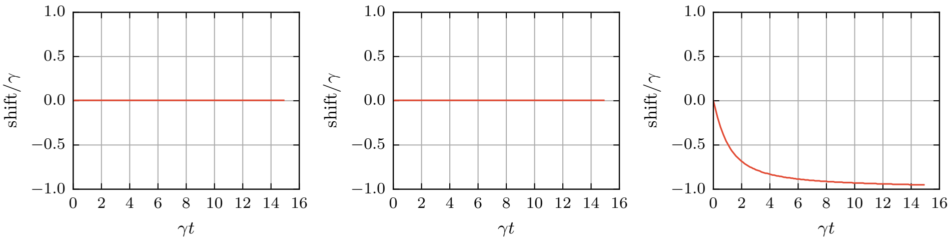

FIG. 8. Shifts of the maxima after the free evolution time γt for different sets of effective interaction strengths as above, from left to right: ($\Omega^{\text{eff}} = 0, \Gamma^{\text{eff}} = -0.75$), ($\Omega^{\text{eff}} = 0, \Gamma^{\text{eff}} = 0$) and ($\Omega^{\text{eff}} = 1, \Gamma^{\text{eff}} = 1$).

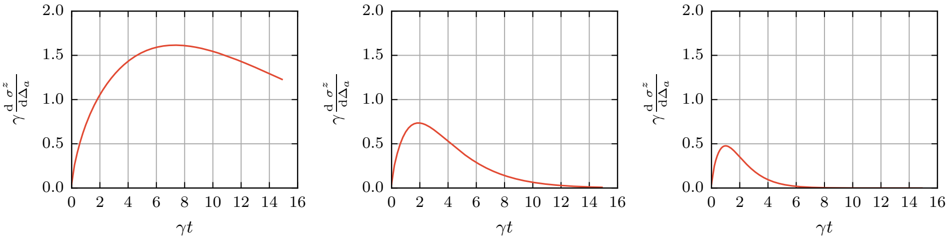

FIG. 9. Slope of the signal at the zero crossing of the first fringe after a free evolution time of γt for different sets of effective interaction strengths as above, from left to right: ($\Omega^{\mathrm{eff}} = 0, \Gamma^{\mathrm{eff}} = -0.75$), ($\Omega^{\mathrm{eff}} = 0, \Gamma^{\mathrm{eff}} = 0$) and ($\Omega^{\mathrm{eff}} = 1, \Gamma^{\mathrm{eff}} = 1$).

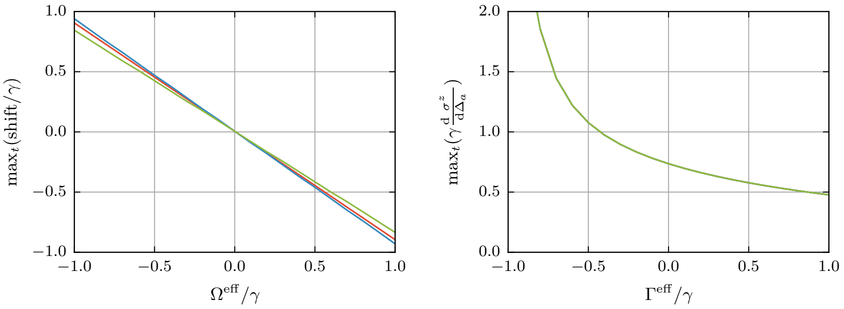

FIG. 10. (a) Shift of Ramsey fringes depending on the effective coupling Ω^{eff} after $t = 15\gamma^{-1}$. The different lines represent different choices of Γ^{eff}, which hardly influence the result. The fringe shifts follow the effective mean field dipole coupling Ω^{eff} almost linearly and thus can be read off from the figures in the main manuscript. (b) Maximally achievable slope at roots depending on Γ^{eff}. The result is independent of the choice of Ω^{eff}. Note that a negative Γ^{eff} improves the measurement precision beyond the independent atom value.

8. Outlook: Spin-squeezing

We showed that by utilizing the dipole-dipole force in a carefully distributed ensemble of atoms the system can be used to obtain frequency uncertainties that are much smaller than the classical $1/\sqrt{N}$ scaling. A successful alternative, which was already proposed in 1996, is to use entanglement [1]. For a maximally correlated state the frequency uncertainty can then be reduced to the theoretical limit of $1/N$. In a slightly modified model, taking realistic noise sources into account, it was demonstrated that moderately squeezed states yield greatly enhanced clock stability [2]. Naturally, this poses the question if combining both approaches, using dipole-dipole interaction as well as entanglement, can lead to even better results. Applying the cumulant expansion to investigate entangled systems might seem like a questionable approach. Exactly the thing that facilitates entanglement, i.e. correlations, is neglected in this approximation. In first order, all correlations are excluded and describing any kind of entanglement is impossible. However, in the second order expansion at least part of these correlations are contained and it might be enough to capture at least parts of the important effects.

In the following we will derive the framework to perform spin squeezing in the second order cumulant expansion formalism.

8.1. Spin-squeezing in second order cumulant expansion

The typical one-axis twisting, as was introduced by Kitagawa and Ueda in [3], can be generated by a unitary time evolution with Hamiltonian

$$H = \chi (S^\gamma)^2 = \chi \frac{1}{N^2} \big(\sum_i \mathbb{1} + \sum_{ij;i\neq j} \sigma_i^\gamma \sigma_j^\gamma \big). \tag{8.1.1}$$

Deriving the second order correlation equations for all possible squeezing axes is tedious work. An alternative approach is to find the equations for one specific orientation and then use spin rotations to first rotate into a suitable coordinate system, perform the squeezing and then rotate back. The advantage is that rotating is described by easier obtainable equations.

8.1.1. Spin rotation

Single spin rotation

Rotation of a single spin density operator is defined by the unitary transformation

$$\tilde{\rho} = \hat{R} \rho \hat{R}^{-1} \tag{8.1.2}$$

with rotation operator $\hat{R}_{\vec{n},\theta}$ and its inverse $\hat{R}^{-1}_{\vec{n},\theta}$,

$$\hat{R}_{\vec{n},\theta} = \mathbb{1}\cos\frac{\theta}{2} - i(\vec{n}.\vec{\sigma})\sin\frac{\theta}{2} \tag{8.1.3a}$$

$$\hat{R}^{-1}_{\vec{n},\theta} = \mathbb{1}\cos\frac{\theta}{2} + i(\vec{n}.\vec{\sigma})\sin\frac{\theta}{2}, \tag{8.1.3b}$$

describing a rotation of angle θ around axis $\vec{n}$.

Equivalently, these relations can be expressed as rotation of an operator,

$$\langle\tilde{A}\rangle = \mathrm{Tr}\left\{A\hat{R}\rho\hat{R}^{-1}\right\} = \mathrm{Tr}\left\{\hat{R}^{-1}A\hat{R}\rho\right\} = \langle\hat{R}^{-1}A\hat{R}\rangle. \tag{8.1.4}$$

Because of the diffeomorphism between the SU(2) group and the unit 3-sphere S^3 (Blochsphere), spin rotations can be written as rotations of expectation values in $\mathbb{R}^3$

$$\langle\hat{R}^{-1}\vec{\sigma}\hat{R}\rangle = R^{-1}.\vec{\langle\sigma\rangle}.R. \tag{8.1.5}$$

with rotation matrix

$$R = \begin{pmatrix} \cos\theta+n_x^2(1-\cos\theta) & n_x n_y(1-\cos\theta)+n_z\sin\theta & n_x n_z(1-\cos\theta)-n_y\sin\theta \\ n_y n_x(1-\cos\theta)-n_z\sin\theta & \cos\theta+n_y^2(1-\cos\theta) & n_y n_z(1-\cos\theta)+n_x\sin\theta \\ n_z n_x(1-\cos\theta)+n_y\sin\theta & n_z n_y(1-\cos\theta)-n_x\sin\theta & \cos\theta+n_z^2(1-\cos\theta) \end{pmatrix}. \tag{8.1.6}$$

Multi-spin rotation

Generalization to more than one spin is straight forward since the spins rotate independently,

$$\hat{R} = \bigotimes_i \hat{R}_i. \tag{8.1.7}$$

Naturally, for single spin expectation values in a multi-spin system we regain the previous relation

$$\begin{aligned} \langle\tilde{\sigma}_k\rangle &= \mathrm{Tr}\left\{\vec{\sigma}_k\hat{R}\rho\hat{R}^{-1}\right\} = \mathrm{Tr}\left\{\hat{R}^{-1}\vec{\sigma}_k\hat{R}\rho\right\} \\ &= \mathrm{Tr}\left\{\Big(\bigotimes_i \hat{R}_i^{-1}\Big)\vec{\sigma}_k\Big(\bigotimes_i \hat{R}_i\Big)\rho\right\} \\ &= \mathrm{Tr}\left\{\hat{R}_k^{-1}\vec{\sigma}_k\hat{R}_k\rho\right\} = \langle\hat{R}_k^{-1}\vec{\sigma}_k\hat{R}_k\rangle = R_k^{-1}.\vec{\langle\sigma_k\rangle}.R_k. \end{aligned} \tag{8.1.8}$$

Rotations of correlations ($k \neq l$), as are necessary for 2nd order cumulant expansion states, can be obtained by

$$\begin{aligned} \langle\sigma_k \,\tilde{\otimes}\, \sigma_l\rangle &= \mathrm{Tr}\left\{(\vec{\sigma}_k\otimes\vec{\sigma}_l)\hat{R}\rho\hat{R}^{-1}\right\} = \mathrm{Tr}\left\{\hat{R}^{-1}(\vec{\sigma}_k\otimes\vec{\sigma}_l)\hat{R}\rho\right\} \\ &= \mathrm{Tr}\left\{\hat{R}_k^{-1}\hat{R}_l^{-1}(\vec{\sigma}_k\otimes\vec{\sigma}_l)\hat{R}_k\hat{R}_l\rho\right\} = \langle\hat{R}_k^{-1}\hat{R}_l^{-1}(\vec{\sigma}_k\otimes\vec{\sigma}_l)\hat{R}_k\hat{R}_l\rangle \\ &= (R_k^{-1}\otimes R_l^{-1}).\langle\sigma_k \,\vec{\otimes}\, \sigma_l\rangle.(R_k\otimes R_l). \end{aligned} \tag{8.1.9}$$

8.1.2. Spin squeezing

The commutator used in the time evolution is for the expectation values

$$[\sigma_k^\alpha, H] = \frac{\chi}{N^2}[\sigma_k^\alpha, \sum_{ij;i\neq j} \sigma_i^\gamma \sigma_j^\gamma] = \frac{2\chi}{N^2}[\sigma_k^\alpha, \sigma_k^\gamma] \sum_{i;i\neq k} \sigma_i^\gamma, \tag{8.1.10}$$

which results in

$$\langle \dot{\sigma}_k^\alpha \rangle = -i\langle [\sigma_k^\alpha, H] \rangle = -i\frac{2\chi}{N^2} \sum_{i;i\neq k} \langle [\sigma_k^\alpha, \sigma_k^\gamma]\sigma_i^\gamma \rangle. \tag{8.1.11}$$

Accordingly the commutator used in the time evolution for the correlations is

$$\begin{aligned}
[\sigma_k^\alpha \sigma_l^\beta, H] &= \frac{\chi}{N^2}[\sigma_k^\alpha \sigma_l^\beta, \sum_{ij;i\neq j} \sigma_i^\gamma \sigma_j^\gamma] \\
&= \frac{2\chi}{N^2}\Big([\sigma_k^\alpha \sigma_l^\beta, \sigma_k^\gamma \sigma_l^\gamma] + \sum_{i;i\neq kl} [\sigma_k^\alpha, \sigma_k^\gamma]\sigma_l^\beta \sigma_i^\gamma + \sum_{i;i\neq kl} [\sigma_l^\beta, \sigma_l^\gamma]\sigma_k^\alpha \sigma_i^\gamma \Big) \\
&= \frac{2\chi}{N^2}\Big(\sigma_k^\alpha \sigma_k^\gamma [\sigma_l^\beta, \sigma_l^\gamma] + [\sigma_k^\alpha, \sigma_k^\gamma]\sigma_l^\beta \sigma_l^\gamma \\
&\qquad + \sum_{i;i\neq kl} [\sigma_k^\alpha, \sigma_k^\gamma]\sigma_l^\beta \sigma_i^\gamma + \sum_{i;i\neq kl} [\sigma_l^\beta, \sigma_l^\gamma]\sigma_k^\alpha \sigma_i^\gamma \Big).
\end{aligned} \tag{8.1.12}$$

S^x squeezing

Choosing a specific axis, in this case the x-axis, leads to the equations of motion for the expectation values,

$$\langle \dot{\sigma}_k^x \rangle = 0 \tag{8.1.13a}$$

$$\langle \dot{\sigma}_k^y \rangle = -\frac{4\chi}{N^2} \sum_{i;i\neq k} \langle \sigma_k^z \sigma_i^x \rangle \tag{8.1.13b}$$

$$\langle \dot{\sigma}_k^z \rangle = \frac{4\chi}{N^2} \sum_{i;i\neq k} \langle \sigma_k^y \sigma_i^x \rangle, \tag{8.1.13c}$$

and for the correlations,

$$\langle \dot{\sigma_k^x \sigma_l^x} \rangle = 0 \tag{8.1.14a}$$

$$\langle \dot{\sigma_k^y \sigma_l^y} \rangle = -\frac{4\chi}{N^2} \sum_{i;i\neq kl} \big(\langle \sigma_k^z \sigma_l^y \sigma_i^x \rangle + \langle \sigma_l^z \sigma_k^y \sigma_i^x \rangle \big) \tag{8.1.14b}$$

$$\langle \dot{\sigma_k^z \sigma_l^z} \rangle = \frac{4\chi}{N^2} \sum_{i;i\neq kl} \big(\langle \sigma_k^y \sigma_l^z \sigma_i^x \rangle + \langle \sigma_l^y \sigma_k^z \sigma_i^x \rangle \big) \tag{8.1.14c}$$

$$\langle \dot{\sigma_k^x \sigma_l^y} \rangle = -\frac{4\chi}{N^2} \big(\langle \sigma_l^z \rangle + \sum_{i;i\neq kl} \langle \sigma_l^z \sigma_k^x \sigma_i^x \rangle \big) \tag{8.1.14d}$$

$$\langle \dot{\sigma_k^x \sigma_l^z} \rangle = \frac{4\chi}{N^2}\big(\langle \sigma_l^y \rangle + \sum_{i;i\neq kl} \langle \sigma_l^y \sigma_k^x \sigma_i^x \rangle\big) \tag{8.1.14e}$$

$$\langle \dot{\sigma_k^y \sigma_l^z} \rangle = \frac{4\chi}{N^2} \sum_{i;i\neq kl} \big(\langle \sigma_k^z \sigma_l^z \sigma_i^x \rangle - \langle \sigma_l^y \sigma_k^y \sigma_i^x \rangle\big). \tag{8.1.14f}$$

8.2. Example

Here, in Fig. 8.1, we show only one example that indicates that the second order cumulant expansions is usable to simulate systems with moderate degree of squeezing.

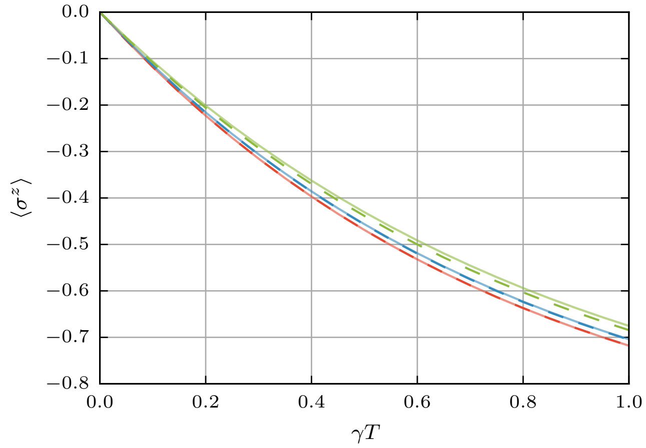

Figure 8.1.: A chain consisting of 5 particles in distance $1.1\lambda_0$ is initialized so that all spins point into the y-direction. Then a squeezing along the x-direction is performed (no squeezing - red, $\chi T = \pi/2$ - blue and $\chi T = \pi$ - green). Finally, the time evolution of $\langle \sigma_z \rangle$ of the middle spin is plotted. The solid line is the result of the second order cumulant expansion and as comparison the dashed line depicts the result of the master equation.

References

1. Bollinger, J. J. ., Itano, W. M., Wineland, D. J. & Heinzen, D. J. Optimal frequency measurements with maximally correlated states. *Physical Review A* **54,** R4649–R4652. ISSN: 1050-2947 (1996).
2. André, A., Sørensen, A. S. & Lukin, M. D. Stability of Atomic Clocks Based on Entangled Atoms. *Physical Review Letters* **92,** 230801. ISSN: 0031-9007 (2004).

3. Kitagawa, M. & Ueda, M. Squeezed spin states. *Physical Review A* **47,** 5138–5143. ISSN: 1050-2947 (1993).

Part III.

Libraries

9. Introduction

To great extent the work done in the scope of this theses was invested into creating fast, and hopefully reusable, numerical programs. As foundation, a framework similar to the quantum-optics toolbox for MATLAB [1] and the QuTiP [2] python library was written in the Julia language [3], named QuantumOptics.jl [4]. Admittedly, this work was to some extent a duplication of the efforts already invested into the afore mentioned projects. However, there are a few reasons why it still was a worthwhile accomplishment. Firstly, Julia is a great language to perform scientific numerical simulations since it is explicitly designed for it. Compared to python the syntax is more specialized to this goal and it is most of the times also faster. Contrary to MATLAB, it is free and it is open source. Secondly, additional features like automatic cumulant expansion and improved enforced correctness for combined systems were much easier to implement. Thirdly, and probably personally the most important advantage is that in rewriting and rethinking the basics, one obtains a much deeper understanding of the used algorithms and their potential problems.

Building upon this very general framework, libraries specialized to the particular physical problems were created. The first one, treating particles coupled to a multi-mode cavity is MultimodeCavity.jl [5]. Most importantly it provides an easy way to specify the concrete system and constructs the appropriate Hamiltonians and jump operators. Additionally, simulations of the semi-classical equations are implemented.

The second part of this theses, treating the dipole-dipole interaction in large spin systems, is covered by the CollectiveSpins.jl [6] library. Its core function is again to provide a painless way to define the system of interest. From there simulations, according to a master equation or to cumulant expansions up to second order, can be performed effortlessly in a few lines. All libraries, QuantumOptics.jl [4], MultimodeCavity.jl [5] and CollectiveSpins.jl [6], are open source and are hosted on github.com.

References

1. Tan, S. M. *et al.* A computational toolbox for quantum and atomic optics. *Journal of Optics B: Quantum and Semiclassical Optics* **1,** 424–432. ISSN: 1464-4266 (1999).

2. Johansson, J., Nation, P. & Nori, F. QuTiP: An open-source Python framework for the dynamics of open quantum systems. *Computer Physics Communications* **183,** 1760–1772. ISSN: 00104655 (2012).
3. Bezanson, J., Edelman, A., Karpinski, S. & Shah, V. B. Julia: A Fresh Approach to Numerical Computing. arXiv: `1411.1607`. <`http://arxiv.org/abs/1411.1607`> (2014).
4. *QuantumOptics.jl* <`https://github.com/bastikr/QuantumOptics.jl`>.
5. *MultimodeCavity.jl* <`https://github.com/bastikr/MultimodeCavity.jl`>.
6. *CollectiveSpins.jl* <`https://github.com/bastikr/CollectiveSpins.jl`>.

10. Quantumoptics.jl

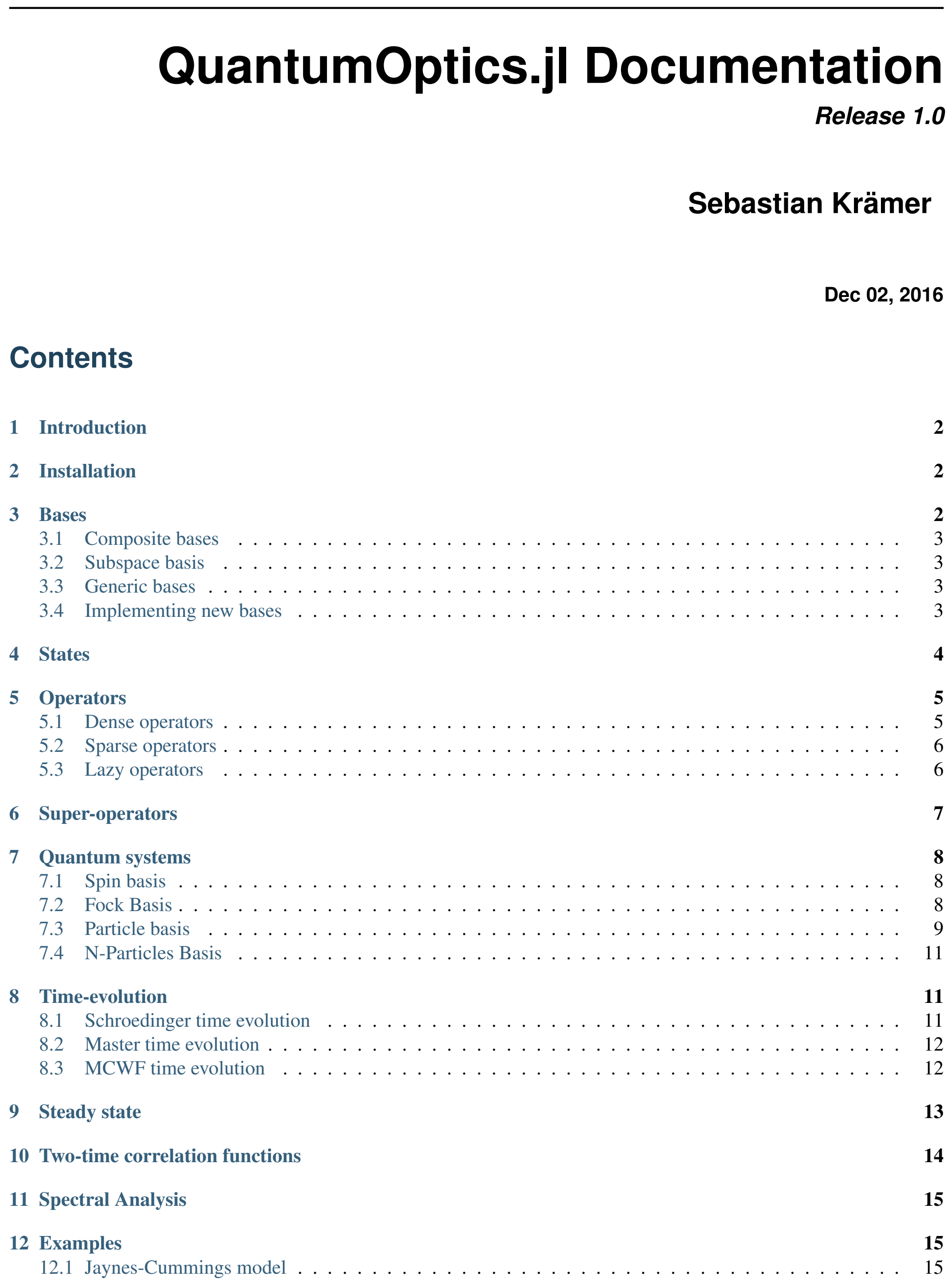

QuantumOptics.jl Documentation

Release 1.0

Sebastian Krämer

Dec 02, 2016

Contents

1 Introduction

QuantumOptics.jl is a numerical framework written in Julia that makes it easy to simulate various kinds of quantum systems. It is similar to the Quantum Optics Toolbox for MATLAB and its Python equivalent QuTiP.

One of the core concepts of **QuantumOptics.jl** is that all quantum objects, i.e. state vectors and operators have knowledge about which Hilbert space they live in. This prevents many common mistakes when working with composite systems and at the same time improves readability. The Hilbert spaces are defined implicitly by specifying appropriate bases like *fock* bases and *spin* bases. These bases can in turn be combined to describe composite systems like e.g. a particle in a cavity or a multi-spin system. Working with bases is explained in great detail in the *Bases* section.

After choosing a basis **QuantumOptics.jl** provides many useful functions to create common *Operators* and *States* which can be combined in all the expected ways. Consequently, constructing arbitrary Hamiltonians and Liouvillians and specifying initial states is straight forward. These objects can be used to perform time evolutions according to *Schroedinger*, *Master* and *Monte Carlo wave function* equations.

Although the main focus is on simulating dynamics of (open) quantum systems, there are nevertheless many additional features available to calculate *steadystates*, the *energy spectrum, eigenstates*, and *correlation functions*.

2 Installation

The source code can be found on github at https://github.com/bastikr/QuantumOptics.jl. The git repository can be obtained using the command

```
>> git clone https://github.com/bastikr/QuantumOptics.jl.git
```

To use the Julia package manager just start up the Julia interpreter and add the package via

```
julia> Pkg.clone("https://github.com/bastikr/QuantumOptics.jl.git")
```

3 Bases

The primary purpose of bases in **QuantumOptics.jl** is to specify the dimension of the Hilbert space of the system and to make sure that quantum objects associated to distinct bases can't be combined accidentally in an incorrect way. Many of the common types of bases used in quantum mechanics like

- *Spin basis*
- *Fock basis*
- *Position basis and Momentum basis*
- *N-particle basis*

are already implemented. They are treated in more detail in the section *Quantum systems*.

3.1 Composite bases

Hilbert spaces of composite systems can be handled with the `CompositeBasis` which can be created using the *tensor* function or the equivalent ⊗ operator:

```
basis_fock = FockBasis(10)
basis_particle = MomentumBasis(0., 10., 50)
basis = tensor(basis_fock, basis_particle)
basis = basis_fock ⊗ basis_particle
```

Most of the time this will happen implicitly when operators are combined using the tensor function.

3.2 Subspace basis

Restricting a Hilbert space to a subspace is done using a `SubspaceBasis`. It is defined by N, not necessarily orthogonal states $\{|u\rangle\}$ that live in the embedding Hilbert space. However, for the following operations to work correctly, the basis states have to be orthonormal. This can be achieved for any SubspaceBasis with help of the `orthonormalize` function which utilizes the numerical stable modified Gram-Schmidt algorithm. Projecting a state $|x\rangle$ into the subspace,

$$|x'\rangle = \sum_{u\in\text{subspace}} |u\rangle\langle u|x\rangle$$

results in the state $|x'\rangle$. This is done with a projection operator that can be obtained via the `projector(::SubspaceBasis,::Basis)` function:

```
b = FockBasis(5)
b_sub = SubspaceBasis(b, [fockstate(b, 1), fockstate(b, 2)])

P = projector(b_sub, b)

x = coherentstate(b, 0.5)
x_prime = P*x
```

The projection operation is irreversible if the original state was not already contained in the subspace. However, it is of course possible to represent any state contained in the subspace in the superbasis:

```
y = dagger(P)*x_prime # Not equal to x
```

3.3 Generic bases

If a needed basis type is not implemented the quick and dirty way is to use a `GenericBasis`, which just needs to know the dimension of the Hilbert space and is ready to go:

```
b = GenericBasis(5)
```

However, since operators and states represented in any generic basis can be combined as long as the bases have the same dimension it might lead to errors that otherwise could have been caught easily.

3.4 Implementing new bases

The cleaner way is to implement own special purpose bases by deriving from the abstract `Basis` type. The only mandatory property of all basis types is that they have a field *shape* which specifies the dimensionality of their Hilbert space. E.g. a spin 1/2 basis could be implemented as:

```
type SpinBasis <: Basis
    shape::Vector{Int}
    SpinBasis() = new(Int[2]) # Constructor
end
```

The default behavior for new bases is to allow operations for bases of the same type, but reject mixing with other bases. Finer control over the interaction with other bases can be achieved by overloading the == operator as well as the `bases.multiplicable` function.

4 States

State vectors in **QuantumOptics.jl** are interpreted as coefficients in respect to a certain *basis*. For example the particle state $|\Psi\rangle$ can be represented in a (discrete) real space basis $\{|x_i\rangle\}_i$ as $\Psi(x_i)$. These quantities are connected by

$$|\Psi\rangle = \sum_i \Psi(x)|x_i\rangle$$

and the conjugate equation

$$\langle\Psi| = \sum_i \Psi(x)^* \langle x_i|$$

The distinction between coefficients in respect to bra or ket states is strictly enforced which guarantees that algebraic mistakes raise an explicit error:

```
basis = FockBasis(3)
x = Ket(basis, [1,1,1]) # Not necessarily normalized
y = Bra(basis, [0,1,0])
```

Many commonly used states are already implemented for various systems, like e.g. *`fockstate`* or *`gaussianstate(::MomentumBasis,x0,p0,sigma)`*.

All expected arithmetic functions like *, /, +, - are implemented:

```
x + x
x - x
2*x
y*x # Inner product
```

The hermitian conjugate is performed by the *`dagger(::Ket)`* function which transforms a bra in a ket and vice versa:

```
dagger(x) # Bra(basis, [1,1,1])
```

Composite states can be created with the *`tensor(::T,::T)`* function or with the equivalent $\otimes$ operator:

```
tensor(x, x)
x ⊗ x
tensor(x, x, x)
```

Normalization functions:

- *`norm(::StateVector,p=2)`*
- *`normalize(::StateVector,p=2)`*
- *`normalize!(::StateVector,p=2)`*

5 Operators

Operators can be defined as linear mappings from one Hilbert space to another. However, equivalently to states, operators in **QuantumOptics.jl** are interpreted as coefficients of an abstract operator in respect to one or more generally two, possibly distinct *bases*. For a certain choice of bases $\{|u_i\rangle\}_i$ and $\{|v_j\rangle\}_j$ an abstract operator A has the coefficients A_{ij} which are connected by the relation

$$A = \sum_{ij} A_{ij} |u_i\rangle\langle v_j|$$

For this reason all operators define a left hand as well as a right hand basis:

```
type MyOperator <: Operator
    basis_l::Basis
    basis_r::Basis
    ...
end
```

For performance reasons there are several different implementations of operators in **QuantumOptics.jl**, all inheriting from the abstract `Operator` type:

- *Dense operators*
- *Sparse operators*
- *Lazy operators*

They have the same interface and can in most cases be used interchangeably, e.g. they can be combined using arithmetic functions *, /, +, -:

```
b = SpinBasis(1//2)
sx = sigmax(b)
sy = sigmay(b)
sx + sy
sx * sy
```

Additionally the following functions are implemented:

- **Hermitian conjugate:** `dagger(::DenseOperator)`
- **Normalization:** `trace(::DenseOperator)` `norm(::DenseOperator,)` `normalize(::DenseOperator)` `normalize!(::DenseOperator)`
- **Expectation values:** `expect(::Operator,::DenseOperator)`
- **Tensor product:** `tensor(::DenseOperator,::DenseOperator)` `tensor(::Ket,::Bra)` `projector(::Ket,::Bra)`
- **Partial trace:** `ptrace(::DenseOperator,indices)` `ptrace(::DenseOperator,index)` `ptrace(::Ket,indices)` `ptrace(::Bra,indices)`

For creating operators of the type $A = I \otimes I \otimes ...a_i... \otimes I$ the very useful embed function can be used:

- `embed(basis,indices,operators)`
- `embed(basis,index,op)`

5.1 Dense operators

`DenseOperator` is implemented as:

```
type DenseOperator <: Operator
    basis_l::Basis
    basis_r::Basis
    data::Matrix{Complex128}
end
```

where the data is stored as complex (dense) matrix in the `data` field.

The *`full(::Operator)`* function can be used to convert other types of operators to dense operators.

5.2 Sparse operators

`SparseOperator` is the default type used in **QuantumOptics.jl**. The reason is that in many quantum systems the Hamiltonians in respect to the commonly used bases are sparse. They are implemented as:

```
type SparseOperator <: Operator
    basis_l::Basis
    basis_r::Basis
    data::SparseMatrixCSC{Complex128}
end
```

To convert other operators to sparse operators the *`sparse(::Operator)`* function can be used.

5.3 Lazy operators

Lazy operators allow delayed evaluation of certain operations. This is useful when combining two operators is numerically expensive but separate multiplication with states is relatively cheap. A nice example is the *`FFTOperator`* operator implemented for particles. It allows using a fast fourier transformation to convert a state from real space to momentum space, applying a diagonal operator and converting it back. Doing this in operator notation is only fast if the the order of operations is $\mathrm{IFFT} * (D * (\mathrm{FFT} * \psi))$. To create a Hamiltonian that uses this calculation order, lazy evaluation is needed:

```
xmin = -5
xmax = 5
Npoints = 100
b_position = PositionBasis(xmin, xmax, Npoints)
b_momentum = MomentumBasis(b_position)

p = momentumoperator(b_momentum)
x = positionoperator(b_position)

fft = particle.FFTOperator(b_momentum, b_position);

H = LazyProduct(dagger(fft), p^2/2, fft) + x^2
```

In this case the Hamiltonian H is a lazy sum of the kinetic term $p^2/2$ and the potential term x^2 where the kinetic term is the lazy product mentioned before. In the end this results in a speed up from $O(N^2)$ to $O(N \log N)$.

All lazy operators inherit from the abstract *`LazyOperator`*. There are currently three different concrete implementations:

- *`LazyTensor`*
- *`LazySum`*
- *`LazyProduct`*

6 Super-operators

If states are defined as abstract elements of the Hilbert space $\mathcal{H}$ then operators are mappings from this Hilbert space to itself, $\mathcal{H} \to \mathcal{H}$. However, in **QuantumOptics.jl** states are specified as coefficients in respect to a specific basis and therefore operators are mappings from elements of the Hilbert space in a certain basis to a elements of the same Hilbert space but possibly in a different basis. The basis free definition is

$$|\Psi\rangle = A|\Phi\rangle$$

while for a basis specific version we have to choose two possibly different bases $\{|u\rangle\}$ and $\{|v\rangle\}$ and express the states $|\Psi\rangle$ and $|\Phi\rangle$ and the operator A in these bases

$$|\Psi\rangle = \sum_u \Psi_u \langle u|\Psi\rangle$$
$$|\Phi\rangle = \sum_v \Phi_v \langle v|\Phi\rangle$$
$$A = \sum_{uv} A_{uv} |v\rangle\langle u|$$

The coefficients are then connected by the equation

$$\Psi_u = \sum_v A_{uv} \Phi_v$$

As next level we now consider mappings from the space of mappings $\mathcal{H} \to \mathcal{H}$ to itself, i.e. $(\mathcal{H} \to \mathcal{H}) \to (\mathcal{H} \to \mathcal{H})$. In operator notation we also call these objects *super-operators*. With the operators A, B and the super-operator S the basis independent expression is denoted by

$$A = SB$$

In contrast, for the basis specific version we have to choose two possibly different bases for A which we denote as $\{|u\rangle\}$ and $\{|v\rangle\}$ and additionally two, also possibly different bases for B, $\{|m\rangle\}$ and $\{|n\rangle\}$.

$$A = \sum_{uv} A_{uv} |v\rangle\langle u|$$
$$B = \sum_{mn} B_{mn} |n\rangle\langle m|$$
$$S = \sum_{uvmn} S_{uvmn} |v\rangle\langle u| \otimes |n\rangle\langle m|$$

The coefficients are then connected by

$$A_{uv} = \sum_{mn} S_{uvmn} B_{mn}$$

The implementation of super-operators in **QuantumOptics.jl** is based on the basis specific concept, which means it has to consider 4 possibly different bases. The two basis choices for the output are stored in the `basis_l` field and the two basis choices for the input are stored in the `basis_r` field. At the moment there are two concrete super-operator types implemented, a dense version *`DenseSuperOperator`* and a sparse version *`SparseSuperOperator`*, both inheriting from the abstract *`SuperOperator`* type.

Besides the expected algebraic operations there are a few additional functions that help creating and working with super-operators:

- *`spre(::DenseOperator)`*
- *`spost(::DenseOperator)`*
- *`liouvillian(H,J)`*
- *`expm`*

7 Quantum systems

Quantum systems in **QuantumOptics.jl** primarily define one or more appropriate bases and additionally provide functions to create common associated operators and states which then can be used to implement a concrete system. At the moment the following types of systems are supported:

7.1 Spin basis

The spin basis class and all related functions are implemented for arbitrary spin numbers. Therefore, the first step is to choose a basis by specifying the appropriate spin number:

```
b = SpinBasis(3//2)
```

This basis can be used to create operators and states:

```
sx = sigmax(b)
state0 = spinup(b)
state1 = sx*state0
```

The definition of the SpinBasis is very simple and is more or less given by:

```
type SpinBasis <: Basis
    shape::Vector{Int}
    spinnumber::Rational{Int}
end
```

All expected operators are implemented:

- `sigmax`
- `sigmay`
- `sigmaz`
- `sigmap`
- `sigmam`

Also the lowest and uppermost states are defined:

- `spinup`
- `spindown`

7.2 Fock Basis

To create a basis of a Fock space **QuantumOptics.jl** provides the `FockBasis` class which has to be supplied with an upper cutoff and optionally with a lower cutoff:

```
Nmax = 10
b1 = FockBasis(Nmax)

Nmin = 2
Nmax = 12
b2 = FockBasis(Nmin, Nmax)
```

In this example even though the dimensions of the Hilbert spaces described by these bases are the same `b1` and `b2` are not and mixing operators in one bases with operators in the other basis will result in an explicit error.

The definition of *`FockBasis`* is essentially:

```
type FockBasis <: Basis
    shape::Vector{Int}
    Nmin::Int
    Nmax::Int
end
```

Many common operators are already defined:

- *`number`*
- *`destroy`*
- *`create`*

Fock states and coherent states can be created using the functions:

- *`fockstate`*
- *`coherentstate`*

Additional functions:

function `qfunc`(*rho*, *alpha*)
Husimi Q representation $\frac{1}{\pi}\langle\alpha|\rho|\alpha\rangle$.

7.3 Particle basis

For particles **QuantumOptics.jl** provides two different choices - either the calculations can be done in real space or they can be done in momentum space by using *`PositionBasis`* or *`MomentumBasis`* respectively. To create a particle basis, a left boundary x_{min}, a right boundary x_{max} and the number of discretization points have to be provided:

```
xmin = -2.
xmax = 4.
N = 10
b_position = PositionBasis(xmin, xmax, N)
```

Equivalently to create a momentum basis a minimal momentum p_{min}, a maximal momentum p_{min} and again the number of discretization points have to be specified:

```
pmin = 0.
pmax = 10.
N = 10
b_momentum = PositionBasis(pmin, pmax, N)
```

The definition of these two bases types is very simple:

```
type PositionBasis <: Basis
    shape::Vector{Int}
    xmin::Float64
    xmax::Float64
    N::Int
end

type MomentumBasis <: Basis
    shape::Vector{Int}
```

```
    pmin::Float64
    pmax::Float64
    N::Int
end
```

Since real space and momentum space are connected via a Fourier transformation the bases are connected. The numerically inevitable cutoff implies that the functions $\Psi(x)$ and $\Psi(p)$ can be interpreted to continue periodically over the whole real axis the specific choice of the cutoff points is therefor irrelevant as long as the interval length stays the same. This free choice of cutoff points allows to easily create a corresponding *MomentumBasis* from a *PositionBasis* and vice versa:

```
b_momentum = MomentumBasis(b_position)
b_position = PositionBasis(b_momentum)
```

When creating a momentum basis from a position basis the cutoff points are connected by $p_{\text{min}} = -\pi/dx$ and $p_{\text{max}} = \pi/dx$ where $dx = (x_{\text{max}} - x_{\text{min}})/N$. Similarly for the inverse procedure the cutoffs are $x_{\text{min}} = -\pi/dp$ and $x_{\text{max}} = \pi/dp$ with $dp = (p_{\text{max}} - p_{\text{min}})/N$.

For convenience a few functions make it easier to work with bases:

function `spacing`(*b*)
Distance between two adjacent points of the real space basis.

function `spacing`(*b*)
Momentum difference between two adjacent points of the momentum basis.

function `samplepoints`(*b*)
x values of the real space basis.

function `samplepoints`(*b*)
p values of the momentum basis.

All operators defined in **QuantumOptics.jl** can be created in respect to both bases, e.g.:

```
p_position = momentumoperator(b_position)
p_momentum = momentumoperator(b_momentum)
```

The following operators are implemented:

- *momentumoperator(b::PositionBasis)*
- *positionoperator(b::PositionBasis)*
- *laplace_x(b::PositionBasis)*
- *laplace_p(b::PositionBasis)*

And functions for creating states:

- *gaussianstate(b::PositionBasis,,,)*:

```
x0 = 0.
p0 = 1.
sigma = 2
Psi_x = gaussianstate(b_position, x0, p0, sigma)
Psi_p = gaussianstate(b_momentum, x0, p0, sigma)
```

Transforming a state from one basis into another can be done efficiently using the *FFTOperator* which can be used in the following way:

```
op_fft = FFTOperator(basis_momentum, basis_position)
Psi_p = op_fft*Psi_x
```

7.4 N-Particles Basis

Describing systems consisting of many identical particles in a tensor product space created out of single particle Hilbert spaces leads to the problem that not all states in this space correspond to real physical states. In this picture one would have to restrict the Hilbert space to a subspace that is invariant under permutation of particles. However, it is also possible to find a valid description that doesn't first introduce redundant states that later on have to be eliminated. The general idea is to choose an arbitrary basis $\{|u_i\rangle\}_i$ of the single particle Hilbert space and create the N-particle Hilbert space from states that count how many particles are in each of these states - which will in the following be denoted as $|\{n\}\rangle$. Of course the sum of these occupation numbers has to be identical to the number of particles. For fermionic particles an additional restriction is that there can't be more than one particle in one state.

This concept is captured in the abstract *`NParticleBasis`* type and in the concrete fermionic and bosonic implementations *`FermionicNParticleBasis`* and *`BosonicNParticleBasis`*.

Connection between additive single particle operator $\sum_i x_i$ and its corresponding N-particle operator:

$$X = \sum_{ij} a_i^\dagger a_j \langle u_i| x |u_j\rangle$$

Connection between additive two particle operator $\sum_{i \neq j} V_{ij}$ and its corresponding N-particle operator:

$$X = \sum_{ijkl} a_i^\dagger a_j^\dagger a_k a_l \langle u_i| \langle u_j| x |u_k\rangle |u_l\rangle$$

The creation of the N-particle operators is implemented in *`nparticleoperator_1(,::DenseOperator)`* and *`nparticleoperator_2(,::DenseOperator)`*.

8 Time-evolution

QuantumOptics.jl implements solver for dynamics of closed and open quantum systems:

- *Schroedinger equation*
- *Master equation*
- *Monte Carlo wave function method (MCWF)*

The interfaces are designed to be as consistent as possible to make it easy to switch between different methods.

8.1 Schroedinger time evolution

The Schroedinger equation as one of the basic postulates of quantum mechanics describes the dynamics of a quantum state in a closed quantum system. In Dirac notation the Schroedinger equation and its adjoint equation read

$$i\hbar \frac{\mathrm{d}}{\mathrm{d}t}|\Psi(t)\rangle = H|\Psi(t)\rangle$$
$$-i\hbar \frac{\mathrm{d}}{\mathrm{d}t}\langle\Psi(t)| = \langle\Psi(t)|H$$

Both versions are implemented and are chosen automatically depending on the type of the provided initial state (Bra or Ket):

- *`schroedinger`*

8.2 Master time evolution

The dynamics of open quantum systems are governed by a master equation in Lindblad form:

$$\dot{\rho} = -\frac{i}{\hbar}\big[H, \rho\big] + \sum_i \big(J_i \rho J_i^\dagger - \frac{1}{2} J_i^\dagger J_i \rho - \frac{1}{2} \rho J_i^\dagger J_i\big)$$

For performance reasons the solver internally first creates the non-hermitian Hamiltonian $H_{\mathrm{nh}} = H - \frac{i\hbar}{2}\sum_i J_i^\dagger J_i$ and solves the equation

$$\dot{\rho} = -\frac{i}{\hbar}\big[H_{\mathrm{nh}}, \rho\big] + \sum_i J_i \rho J_i^\dagger$$

If for any reason this behavior is unwanted, e.g. special operators are used that don't support addition, the function master_h (h for hermitian) can be used.

- *`master(tspan,rho0::DenseOperator,H::Operator,J::Vector)`*
- *`master_h(tspan,rho0::DenseOperator,H::Operator,J::Vector)`*
- *`master_nh(tspan,rho0::DenseOperator,Hnh::Operator,J::Vector)`*

8.3 MCWF time evolution

Instead of solving the Master equation

$$\dot{\rho} = -\frac{i}{\hbar}\big[H, \rho\big] + \sum_i \big(J_i \rho J_i^\dagger - \frac{1}{2} J_i^\dagger J_i \rho - \frac{1}{2} \rho J_i^\dagger J_i\big)$$

directly, one can use the quantum jump formalism to evaluate single stochastic quantum trajectories using the Monte Carlo wave function method. For large numbers of trajectories the statistical average then approximates the result of the Master equation. The huge advantage is that instead of describing the state of the quantum system by a density matrix of size N^2 these trajectories work in terms of state vectors of size N. This is somewhat negated by the stochastic nature of the formalism which makes it necessary to repeat the simulation until the wanted accuracy is reached. It turns out, however, that for many cases, especially for high dimensional quantum systems, the necessary number of repetitions is much smaller than the system size N and therefore using the MCWF method is advantageous.

Additionally this quantum jump formalism also has a very intuitive physical interpretation. It basically describes the situation where every quantum jump, e.g. the emission of a photon, is detected by a detector and therefore the time evolution can be completely reconstructed by an outside observer. Depending on the efficiency of the used detectors this might be a much better description for an actual experiment.

This physical picture can be used to easily understand the actual MCWF algorithm:

1. Calculate coherent time evolution according to a Schroedinger equation with non-hermitian Hamiltonian $H_{\mathrm{nh}} = H - \frac{i\hbar}{2}\sum_i J_i^\dagger J_i$

   $$i\hbar \frac{\mathrm{d}}{\mathrm{d}t}|\Psi(t)\rangle = H_{\mathrm{nh}}|\Psi(t)\rangle$$

2. Since the Hamiltonian is non-hermitian the norm of the quantum state is not conserved and actually decreases with time. This can be interpreted in the way that the smaller the norm of the state gets the more probable it is that a quantum jump occurs. Quantitatively this means that the coherent time evolution stops when $\langle\Psi(t)|\Psi(t)\rangle < p$ where p is a randomly generated number between 0 and 1.

3. At these randomly determined times a quantum jump according to

$$|\Psi(t)\rangle \rightarrow \frac{J_i|\Psi(t)\rangle}{||J_i|\Psi(t)\rangle||}$$

is performed.

4. Continue with coherent time evolution.

The stochastic average of these trajectories is then equal to the solution of the master equation $\rho(t)$

$$\lim_{N\to\infty} \frac{1}{N} \sum_{k=1}^{N} |\Psi^k(t)\rangle\langle\Psi^k(t)| = \rho(t)$$

and also the stochastic average of the single trajectory expectation values is equal to the expectation value according to the master equation

$$\lim_{N\to\infty} \frac{1}{N} \sum_{k=1}^{N} \langle\Psi^k(t)|A|\Psi^k(t)\rangle = \mathrm{Tr}\{A\rho(t)\}$$

avoiding explicit calculations of density matrices.

- *`master(tspan,psi0::Ket,H::Operator,J::Vector)`*

9 Steady state

QuantumOptics.jl implements two different ways to calculate steady states. The first one is to perform a time evolution according to a master equation until a adequate accuracy is reached:

function `master` (*H*, *J*; *rho0*, *eps*, *hmin*, *Gamma*, *Jdagger*, *fout*, *tmp*)

Calculate steady state using long time master equation evolution.

Parameters

- **`H`** – Operator specifying the Hamiltonian.
- **`J`** – Vector of jump operators.

Keyword Arguments

- **rho0** – Initial density operator. If not given the $|0\rangle\langle 0|$ state in respect to the choosen basis is used.
- **eps** – Tracedistance used as termination criterion.
- **hmin** – Minimal time step used in the time evolution.
- **Gamma** – Vector or matrix specifying the coefficients for the jump operators.
- **Jdagger (optional)** – Vector containing the hermitian conjugates of the jump operators. If they are not given they are calculated automatically.
- **fout (optional)** – If given this function fout(t, rho) is called every time an output should be displayed. To limit copying to a minimum the given density operator rho is further used and therefore must not be changed.
- **kwargs** – Further arguments are passed on to the ode solver.

For smaller system sizes finding eigenvectors of super-operators is the prefered method:

function `eigenvector` (*L*)

Find steady state by calculating the eigenstate of the Liouvillian matrix.

Parameters `L` – Dense or sparse super-operator.

function `eigenvector` (*H*, *J*)

Find steady state by calculating the eigenstate of the Liouvillian matrix.

Parameters

- `H` – Operator specifying the Hamiltonian.
- `J` – Vector of jump operators.

10 Two-time correlation functions

function `correlation` (*tspan*, *rho0*, *H*, *J*, *op1*, *op2*; *Gamma*, *Jdagger*, *tmp*)

Calculate two time correlation values $\langle A(t)B(0)\rangle$

The calculation is done by multiplying the initial density operator with B performing a time evolution according to a master equation and then calculating the expectation value $\mathrm{Tr}\{A\rho\}$

Parameters

- `tspan` – Points of time at which the correlation should be calculated.
- `rho0` – Initial density operator.
- `H` – Operator specifying the Hamiltonian.
- `J` – Vector of jump operators.
- `op1` – Operator at time t.
- `op2` – Operator at time t=0.

Keyword Arguments

- **Gamma** – Vector or matrix specifying the coefficients for the jump operators.
- **Jdagger (optional)** – Vector containing the hermitian conjugates of the jump operators. If they are not given they are calculated automatically.
- **kwargs** – Further arguments are passed on to the ode solver.

function `correlation` (*rho0*, *H*, *J*, *op1*, *op2*; *eps*, *h0*, *Gamma*, *Jdagger*, *tmp*)

Calculate two time correlation values $\langle A(t)B(0)\rangle$

The calculation is done by multiplying the initial density operator with B performing a time evolution according to a master equation and then calculating the expectation value $\mathrm{Tr}\{A\rho\}$. The points of time are chosen automatically from the ode solver and the final time is determined by the steady state termination criterion specified in `steadystate.master`.

Parameters

- `rho0` – Initial density operator.
- `H` – Operator specifying the Hamiltonian.
- `J` – Vector of jump operators.
- `op1` – Operator at time t.
- `op2` – Operator at time t=0.

Keyword Arguments

- **eps** – Tracedistance used as termination criterion.

- **h0** – Initial time step used in the time evolution.
- **Gamma** – Vector or matrix specifying the coefficients for the jump operators.
- **Jdagger (optional)** – Vector containing the hermitian conjugates of the jump operators. If they are not given they are calculated automatically.
- **kwargs** – Further arguments are passed on to the ode solver.

11 Spectral Analysis

- `operatorspectrum(::DenseOperator)`
- `operatorspectrum_hermitian(::DenseOperator)`
- `eigenstates(::DenseOperator)`
- `eigenstates_hermitian(::DenseOperator)`
- `groundstate`

12 Examples

This notebook can be found on github

12.1 Jaynes-Cummings model

The Jaynes Cummings model is a famous theoretical model in the field of quantum optics. It describes a two level atom coupled to a quantized mode of a cavity.

$H = \omega_c a^\dagger a + \frac{\omega_a}{2}\sigma_z + \Omega(a\sigma_+ + a^\dagger\sigma_-)$

The first step is always to import the library

```julia
using QuantumOptics
using PyPlot
```

Then we can define all the necessary parameters

```julia
# Parameters
N_cutoff = 10

ωc = 0.1
ωa = 0.1
Ω = 1.;
```

Describe the Fock Hilbert space and the Spin Hilbert space by choosing the appropriate bases

```julia
# Bases
b_fock = FockBasis(N_cutoff)
b_spin = SpinBasis(1//2)
b = b_fock ⊗ b_spin;
```

With the help of these bases build up the Jaynes-Cummings Hamiltonian

```
# Fundamental operators
a = destroy(b_fock)
at = create(b_fock)
n = number(b_fock)

sm = sigmam(b_spin)
sp = sigmap(b_spin)
sz = sigmaz(b_spin)

# Hamiltonian
Hatom = ωa*sz/2
Hfield = ωc*n
Hint = Ω*(at⊗sm + a⊗sp)
H = identityoperator(b_fock)⊗Hatom + Hfield⊗identityoperator(b_spin) + Hint;
```

The time evolution of the system is governed by a Schroedinger equation.

```
# Initial state
α = 1.
Ψ0 = coherentstate(b_fock, α) ⊗ spindown(b_spin)

# Integration time
T = [0:0.1:20;]

# Schroedinger time evolution
tout, Ψt = timeevolution.schroedinger(T, Ψ0, H);
```

The integration routine returns two objects - a vector containing points of time where output was generated (which will in most cases be the same as the given input time vector) and a vector containing the state of the quantum system at these points in time. These can further on be used to calculate expectation values.

```
exp_n = expect(n ⊗ identityoperator(b_spin), Ψt)
exp_sz = expect(identityoperator(b_fock) ⊗ sz, Ψt);
```

Finally we can us matplotlib to visualize the the time evolution of the calculated expectation values

```
figure(figsize=(9,3))
subplot(1,2,1)
ylim([0, 2])
plot(T, exp_n);
xlabel(L"T")
ylabel(L"\langle n \rangle")

subplot(1,2,2)
ylim([-1, 1])
plot(T, exp_sz);
xlabel(L"T")
ylabel(L"\langle \sigma_z \rangle")

tight_layout();
```

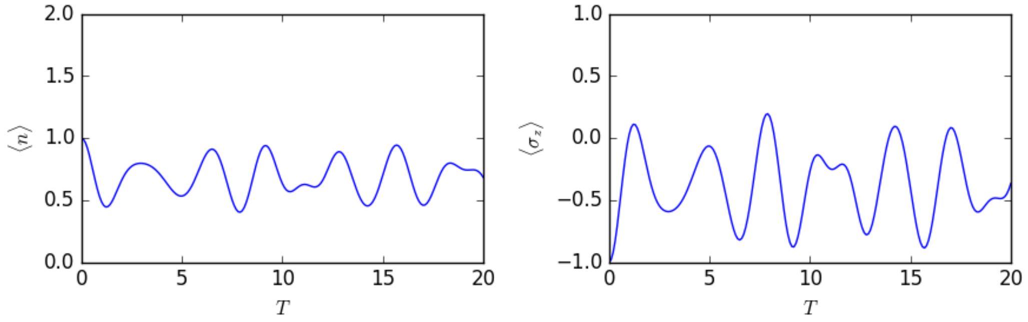

Lossy Jaynes-Cummings model

The Jaynes-Cummings model can be expanded by giving the 2 level atom a finite spontenous decay rate γ. The system is then a open quantum system which is described by a master equation of the form

$$\dot{\rho} = -\frac{i}{\hbar}[H, \rho] + \sum_i \left(J_i \rho J_i^\dagger - \frac{1}{2} J_i^\dagger J_i \rho - \frac{1}{2} \rho J_i^\dagger J_i\right)$$

where in this case there is only one jump operator $J = \sqrt{\gamma}\sigma_-$.

```
γ = 0.5
J = [sqrt(γ)*identityoperator(b_fock) ⊗ sm];
```

```
# Master
tout, ρt = timeevolution.master(T, Ψ0, H, J)
exp_n_master = expect(n ⊗ identityoperator(b_spin), ρt)
exp_sz_master = expect(identityoperator(b_fock) ⊗ sz, ρt)

figure(figsize=(9,3))
subplot(1,2,1)
ylim([0, 2])
plot(T, exp_n_master);
xlabel(L"T")
ylabel(L"\langle n \rangle")

subplot(1,2,2)
ylim([-1, 1])
plot(T, exp_sz_master);
xlabel(L"T")
ylabel(L"\langle \sigma_z \rangle");

tight_layout();
```

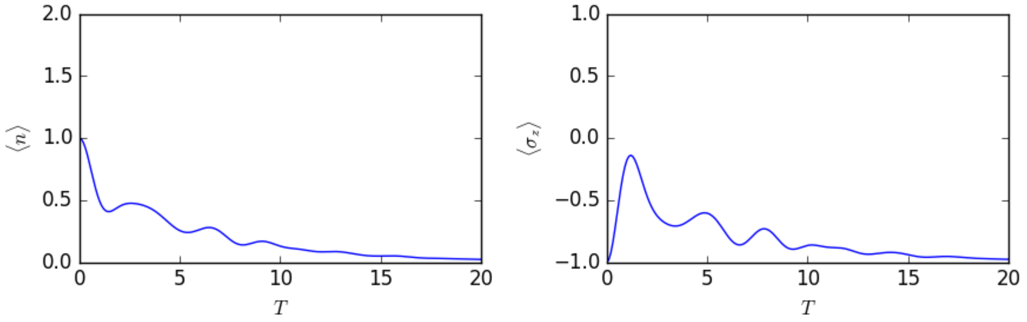

Alternatively we can solve the system using the Monte Carlo wave function formalism. A single trajectory shows characteristic jumps in the expectation values.

```
# Monte Carlo wave function
tout, Ψt = timeevolution.mcwf(T, Ψ0, H, J; seed=2,
                                display_beforeevent=true,
                                display_afterevent=true)
exp_n_mcwf = expect(n ⊗ identityoperator(b_spin), Ψt)
exp_sz_mcwf = expect(identityoperator(b_fock) ⊗ sz, Ψt)

figure(figsize=(9,3))
subplot(1,2,1)
ylim([0, 2])
plot(tout, exp_n_mcwf)
xlabel(L"T")
ylabel(L"\langle n \rangle")

subplot(1,2,2)
ylim([-1, 1])
plot(tout, exp_sz_mcwf)
xlabel(L"T")
ylabel(L"\langle \sigma_z \rangle");

tight_layout();
```

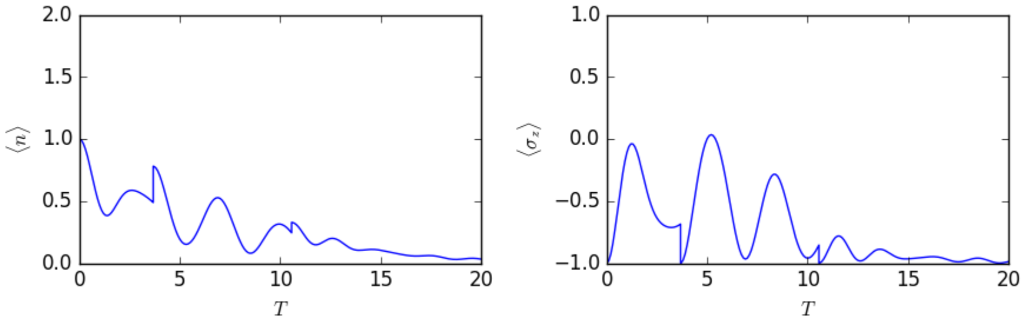

For large number of trajectories the statistical average of the MCWF trajectories approaches the solution of the master equation.

```
Ntrajectories = 10
exp_n_average = zeros(Float64, length(T))
exp_sz_average = zeros(Float64, length(T))

for i = 1:Ntrajectories
    tout, Ψt = timeevolution.mcwf(T, Ψ0, H, J; seed=i)
    exp_n_average += expect(n ⊗ identityoperator(b_spin), Ψt)
    exp_sz_average += expect(identityoperator(b_fock) ⊗ sz, Ψt)
end

exp_n_average /= Ntrajectories
exp_sz_average /= Ntrajectories

figure(figsize=(9,3))
subplot(1,2,1)
ylim([0, 2])
plot(T, exp_n_master)
plot(T, exp_n_average)
xlabel(L"T")
ylabel(L"\langle n \rangle")

subplot(1,2,2)
ylim([-1, 1])
plot(T, exp_sz_master)
plot(T, exp_sz_average)
xlabel(L"T")
ylabel(L"\langle \sigma_z \rangle");

tight_layout();
```

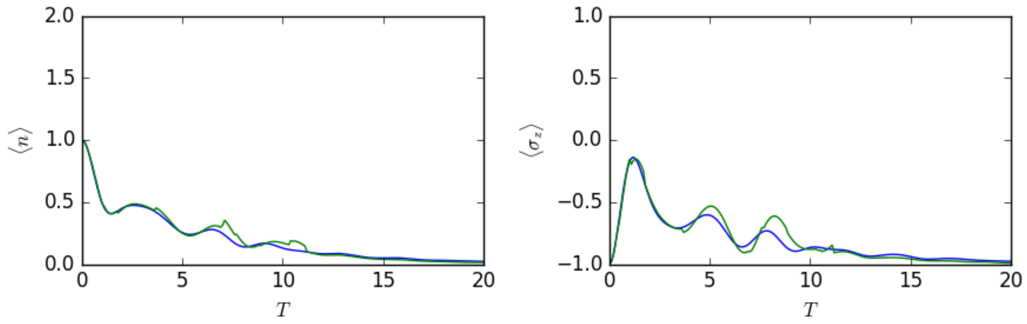

This notebook can be found on github

12.2 Particle in harmonic trap potential

A particle in a harmonic trap is described by a Hamiltonian of the form

$$H = \frac{\hat{p}^2}{2m} + \frac{1}{2}m\omega^2\hat{x}^2$$

For numerical simulations we are forced to work in a basis. For particles there are two common choices. We can either work in real space or alternatively in momentum space.

```
using QuantumOptics
using PyPlot
```

```
# System Parameters
m = 1.
ω = 0.5 # Strength of trapping potential;
```

```
# Position Basis
xmin = -5
xmax = 5
Npoints = 100
b_position = PositionBasis(xmin, xmax, Npoints)

# Hamiltonian in real space basis
p = momentumoperator(b_position)
x = positionoperator(b_position)

H = p^2/2m + 1/2*m*ω^2*x^2;
```

Of course we could also choose to work in momentum space:

From a PositionBasis **QuantumOptics.jl** can automatically infere the corresponding MomentumBasis by calculating $p_{\text{min}} = -\pi/dx$ and $p_{\text{max}} = \pi/dx$ where $dx = (x_{\text{max}} - x_{\text{min}})/N$

```
b_momentum = MomentumBasis(b_position);

# Hamiltonian
p = momentumoperator(b_momentum)
x = positionoperator(b_momentum)

H = p^2/2m + 1/2*m*ω^2*x^2;
```

However, both choices are not optimal since in real space the position operator is diagonal while the momentum operator is a completely dense matrix and vice versa for the momentum space. Therefore, the calculation will scale with N^2 where N is the dimension of the Hilbert space. A commonly used trick is to utilize fast Fourier transformation to convert the state of the system between real and momentum space. This allows us to always use the diagonal form of the operators which all in all speeds up the calculations to $N \log N$.

This idea is implemented by the FFTOperator which performs a fast Fourier transformation on the multiplied state.

```
# Transforms a state multiplied from the right side from real space
# to momentum space.
op_fft = particle.FFTOperator(b_momentum, b_position);
```

To use this operator in a Hamiltonian we additionally need the concept of lazy operators which allow us to delay certain operations to a later point in the simulation. E.g. the LazyProduct allows us to do $A * (B * x)$ instead of $(A * B) * x$ which means for our case that the matrix-matrix product never has to be calculated directly but only two matrix-vector multiplications instead.

```
op_inversefft = dagger(op_fft)

x = positionoperator(b_position)
p = momentumoperator(b_momentum)

H = LazyProduct(op_inversefft, p^2/2m, op_fft) + ω*x^2;
```

Finally we can simulate the time evolution according to a Schroedinger equation.

```
# Initial state
x0 = 1.5
p0 = 0
sigma0 = 0.6
Ψ0 = gaussianstate(b_position, x0, p0, sigma0);

# Time evolution
T = [0:0.5:20;]
tout, Ψt = timeevolution.schroedinger(T, Ψ0, H);

# Plot dynamics of particle density
x_points = particle.samplepoints(b_position)

n = abs(Ψ0.data).^2
V = ω*x_points.^2
C = maximum(V)/maximum(n)

figure(figsize=(7,3.5))
xlabel(L"x")
ylabel(L"| \Psi(t) |^2")
plot(x_points, V/C, "k")

for Ψ=Ψt
    n = abs(Ψ.data).^2
    plot(x_points, n, "r")
end;
```

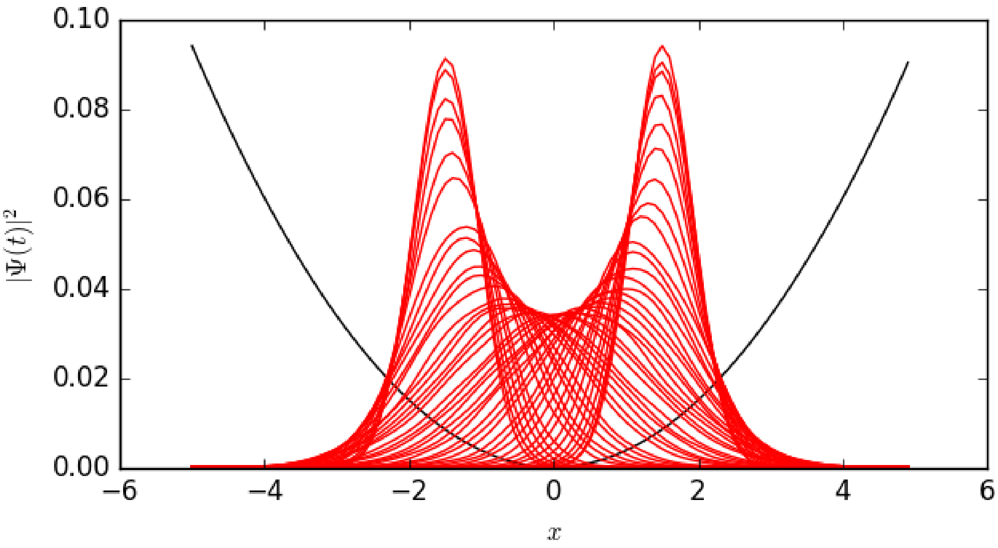

11. DipoleInteraction.jl

DipoleInteraction.jl Documentation

Release 0.1

Sebastian Krämer

Dec 02, 2016

Contents

---

1 Introduction

CollectiveSpins.jl is a numerical framework written in Julia that can be used to simulate quantum systems consisting of spatially distributed spins interacting via *Dipole-Dipole interaction*, optionally coupled to a cavity.

The *Geometry* module allows rapid creation of arbitrary placed spins to build up very general systems as explained in the *System* documentation. These in turn can then be investigated using either a complete quantum description or cumulant expansions up to second order. The details are presented in *Theoretical descriptions*.

2 Installation

The source code can be found on github at https://github.com/bastikr/CollectiveSpins.jl. The git repository can be obtained using the command

```
>> git clone https://github.com/bastikr/CollectiveSpins.jl.git
```

To use the Julia package manager just start up the Julia interpreter and add the package via

```
julia> Pkg.clone("https://github.com/bastikr/CollectiveSpins.jl.git")
```

3 System

The basic building blocks used in **CollectiveSpins.jl** are, not surprisingly, spins. They are defined by their position and a frequency Δ describing a shift relative to the frequency of the rotating frame in use:

```
type Spin <: System
    position::Vector{Float64}
    delta::Float64
end
```

Defining the frequency is optional and is set to zero by default:

```
>>> Spin([0,0,0]; delta=1)
>>> Spin([0,0,0])
```

Combining many spins into one big system can be done by using the `system.SpinCollection` type. All contained spins must have the same polarization axis and decay rate γ:

```
type SpinCollection <: System
    spins::Vector{Spin}
    polarization::Vector{Float64}
    gamma::Float64
end
```

For convenience one can create a `system.SpinCollection` without explicitly constructing the single spins first:

```
>>> SpinCollection([[0,0,0], [1,0,0]], [0,0,1]; gamma=2, delta=1)
```

Adding a cavity can be done with the `system.CavityMode` type:

```
type CavityMode <: System
    cutoff::Int
    delta::Float64
    eta::Float64
    kappa::Float64
end
```

which can be coupled to a spin collection with coupling strength g via the `system.CavitySpinCollection` type:

```
type CavitySpinCollection <: System
    cavity::CavityMode
    spincollection::SpinCollection
```

```
    g::Vector{Float64}
end
```

4 Geometry

In order to simplify creation of various particle distributions, a few helper functions with self-explanatory names are provided:

- *geometry.chain*
- *geometry.triangle*
- *geometry.rectangle*
- *geometry.square*
- *geometry.hexagonal*
- *geometry.box*
- *geometry.cube*

They can be used directly to create a *system.SpinCollection*:

```
>>> SpinCollection(geometry.chain(0.5, 6), [0,0,1])
```

5 Dipole-Dipole interaction

Of course the core of this library are the equations describing the dipole-dipole interaction and the collective decay

$$\Gamma_{ij} = \frac{3}{2}\Gamma F_{ij}(k_a r_{ij})$$
$$\delta\omega_{ij} = \frac{3}{4}\Gamma G_{ij}(k_a r_{ij})$$

with

$$F_{ij}(\xi) = \big(1 - (\vec{e}^{(r)}.\vec{e}^{(d_{eg})})^2\big)\frac{\sin\xi}{\xi} + \big(1 - 3(\vec{e}^{(r)}.\vec{e}^{(d_{eg})})^2\big)\big(\frac{\cos\xi}{\xi^2} - \frac{\sin\xi}{\xi^3}\big),$$
$$G_{ij}(\xi) = -\big(1 - (\vec{e}^{(r)}.\vec{e}^{(d_{eg})})^2\big)\frac{\cos\xi}{\xi} + \big(1 - 3(\vec{e}^{(r)}.\vec{e}^{(d_{eg})})^2\big)\big(\frac{\sin\xi}{\xi^2} - \frac{\cos\xi}{\xi^3}\big).$$

They are implemented in the functions:

- *interaction.Omega(a,θ,γ)*
- *interaction.Gamma(a,θ,γ)*

To create the interaction matrices the following two shortcuts are provided:

- *interaction.GammaMatrix*
- *interaction.OmegaMatrix*

6 Effective Interactions

Effective interactions occur in the equations of motion of large spin systems that have certain symmetries so that the dynamics of every single spin is identical:

$$\begin{aligned}
\langle \dot{\sigma^x} \rangle &= \Omega^{\text{eff}} \langle \sigma^y \rangle \langle \sigma^z \rangle - \frac{1}{2}\Big(\gamma - \Gamma^{\text{eff}} \langle \sigma^z \rangle\Big) \langle \sigma^x \rangle, \\
\langle \dot{\sigma^y} \rangle &= -\Omega^{\text{eff}} \langle \sigma^x \rangle \langle \sigma^z \rangle - \frac{1}{2}\Big(\gamma - \Gamma^{\text{eff}} \langle \sigma^z \rangle\Big) \langle \sigma^y \rangle, \\
\langle \dot{\sigma^z} \rangle &= -\gamma\big(1 + \langle \sigma^z \rangle\big) - \frac{1}{2}\Gamma^{\text{eff}}\Big(\langle \sigma^x \rangle^2 + \langle \sigma^y \rangle^2\Big).
\end{aligned}$$

These quantities encapsulate the influence of all spins onto one single spin:

$$\Omega^{\text{eff}} = \sum_{j=2}^{N} \Omega_{1j}$$

$$\Gamma^{\text{eff}} = \sum_{j=2}^{N} \Gamma_{1j}.$$

The following functions can be used to easily calculate them for common examples:

- `effective_interaction.triangle_orthogonal`
- `effective_interaction.square_orthogonal`
- `effective_interaction.rectangle_orthogonal`
- `effective_interaction.cube_orthogonal`
- `effective_interaction.box_orthogonal`
- `effective_interaction.chain`
- `effective_interaction.chain_orthogonal`
- `effective_interaction.squarelattice_orthogonal`
- `effective_interaction.hexagonallattice_orthogonal`
- `effective_interaction.cubiclattice_orthogonal`
- `effective_interaction.tetragonallattice_orthogonal`
- `effective_interaction.hexagonallattice3d_orthogonal`

6.1 Rotated effective interactions

If we allow for the individual atomic states to bare a spatially dependent phase of $\Delta\phi$ on the excited state, i.e. $|\psi_k\rangle = \frac{1}{\sqrt{2}}\left(|g\rangle + \exp(i\phi_k)|e\rangle\right)$, we can absorb this into our equations efficiently. Using the abbreviations

$\Omega_{kj}^{\cos} = \Omega_{kj}\cos(\phi_k - \phi_j)$ and $\Omega_{kj}^{\sin} = \Omega_{kj}\sin(\phi_k - \phi_j)$ we obtain the following modified equations of motion

$$\begin{aligned}
\frac{d}{dt}\langle\tilde{\sigma}_k^x\rangle &= \sum_{j;j\neq k}\Omega_{kj}^{\sin}\langle\tilde{\sigma}_j^x\sigma_k^z\rangle + \sum_{j;j\neq k}\Omega_{kj}^{\cos}\langle\tilde{\sigma}_j^y\sigma_k^z\rangle - \frac{1}{2}\gamma\langle\tilde{\sigma}_k^x\rangle + \frac{1}{2}\sum_{j;j\neq k}\Gamma_{kj}^{\cos}\langle\tilde{\sigma}_j^x\sigma_k^z\rangle - \frac{1}{2}\sum_{j;j\neq k}\Gamma_{kj}^{\sin}\langle\tilde{\sigma}_j^y\sigma_k^z\rangle\\
\frac{d}{dt}\langle\tilde{\sigma}_k^y\rangle &= -\sum_{j;j\neq k}\Omega_{kj}^{\cos}\langle\tilde{\sigma}_j^x\sigma_k^z\rangle + \sum_{j;j\neq k}\Omega_{kj}^{\sin}\langle\tilde{\sigma}_j^y\sigma_k^z\rangle - \frac{1}{2}\gamma\langle\tilde{\sigma}_k^y\rangle + \frac{1}{2}\sum_{j;j\neq k}\Gamma_{kj}^{\sin}\langle\tilde{\sigma}_j^x\sigma_k^z\rangle + \frac{1}{2}\sum_{j;j\neq k}\Gamma_{kj}^{\cos}\langle\tilde{\sigma}_j^y\sigma_k^z\rangle\\
\frac{d}{dt}\langle\sigma_k^z\rangle &= -\sum_{j;j\neq k}\Omega_{kj}^{\sin}(\langle\tilde{\sigma}_j^x\tilde{\sigma}_k^x\rangle + \langle\tilde{\sigma}_j^y\tilde{\sigma}_k^y\rangle) + \sum_{j;j\neq k}\Omega_{kj}^{\cos}(\langle\tilde{\sigma}_j^x\tilde{\sigma}_k^y\rangle - \langle\tilde{\sigma}_j^y\tilde{\sigma}_k^x\rangle)\\
&\qquad - \gamma(1+\langle\sigma_k^z\rangle) - \frac{1}{2}\sum_{j;j\neq k}\Gamma_{kj}^{\cos}(\langle\tilde{\sigma}_j^x\tilde{\sigma}_k^x\rangle + \langle\tilde{\sigma}_j^y\tilde{\sigma}_k^y\rangle) - \frac{1}{2}\sum_{j;j\neq k}\Gamma_{kj}^{\sin}(\langle\tilde{\sigma}_j^x\tilde{\sigma}_k^y\rangle - \langle\tilde{\sigma}_j^y\tilde{\sigma}_k^x\rangle).
\end{aligned}$$

We see that the following definitions prove to be very helpful

$$\begin{aligned}
\Omega_k^{\cos} &= \sum_{j;j\neq k}\Omega_{kj}\cos(\phi_k - \phi_j) \qquad & \Omega_k^{\sin} &= \sum_{j;j\neq k}\Omega_{kj}\sin(\phi_k - \phi_j)\\
\Gamma_k^{\cos} &= \sum_{j;j\neq k}\Gamma_{kj}\cos(\phi_k - \phi_j) \qquad & \Gamma_k^{\sin} &= \sum_{j;j\neq k}\Gamma_{kj}\sin(\phi_k - \phi_j)
\end{aligned}$$

Again, if we consider highly symmetric configurations where $\Omega^{\mathrm{f}} = \Omega_k^{\mathrm{f}}$ and $\Gamma^{\mathrm{f}} = \Gamma_k^{\mathrm{f}}$ and the rotated states are initially identical we can define the effective rotated quantities

$$\begin{aligned}
\tilde{\Omega}^{\mathrm{eff}} &= \Omega^{\cos} - \frac{1}{2}\Gamma^{\sin}\\
\tilde{\Gamma}^{\mathrm{eff}} &= \Gamma^{\cos} + 2\Omega^{\sin}
\end{aligned}$$

which lead to a closed set of simplified effective equations as well, i.e.

$$\begin{aligned}
\frac{d}{dt}\langle\tilde{\sigma}^x\rangle &= \tilde{\Omega}^{\mathrm{eff}}\langle\tilde{\sigma}^y\rangle\langle\sigma^z\rangle - \frac{1}{2}\gamma\langle\tilde{\sigma}^x\rangle + \frac{1}{2}\tilde{\Gamma}^{\mathrm{eff}}\langle\tilde{\sigma}^x\rangle\langle\sigma^z\rangle\\
\frac{d}{dt}\langle\tilde{\sigma}^y\rangle &= -\tilde{\Omega}^{\mathrm{eff}}\langle\tilde{\sigma}^x\rangle\langle\sigma^z\rangle - \frac{1}{2}\gamma\langle\tilde{\sigma}^y\rangle + \frac{1}{2}\tilde{\Gamma}^{\mathrm{eff}}\langle\tilde{\sigma}^y\rangle\langle\sigma^z\rangle\\
\frac{d}{dt}\langle\sigma^z\rangle &= -\gamma\big(1+\langle\sigma^z\rangle\big) - \frac{1}{2}\tilde{\Gamma}^{\mathrm{eff}}\Big(\langle\tilde{\sigma}^x\rangle^2 + \langle\tilde{\sigma}^y\rangle^2\Big)
\end{aligned}$$

The calculation of these quantities for a few systems is implemented by:

- `effective_interaction_rotated.square_orthogonal`
- `effective_interaction_rotated.cube_orthogonal`
- `effective_interaction_rotated.chain_orthogonal`

7 Theoretical descriptions

CollectiveSpins.jl provides several different possibilities to simulate multi-spin systems. A full quantum description is available but only possible for small numbers of spins. Additionally, approximations of different orders are implemented using a cumulant expansion approach:

- `quantum` - *Quantum*
- `independent` - *0th order: Independent spins*
- `meanfield` - *1st order: Meanfield*
- `mpc` - *2nd order: Meanfield plus Correlations (MPC)*

All variants provide a unified interface wherever possible:

- `blochstate(phi,theta)`
- `densityoperator(state)`
- `sx(state)`
- `sy(state)`
- `sz(state)`
- `timeevolution(T,system,state0; fout=nothing)`
- `rotate(axis,angles,state)`
- `squeeze(axis,χT,state)`
- `squeezingparameter(state)`

The following example should give a first idea how these implementations are used:

```
using QuantumOptics, CollectiveSpins
const cs = CollectiveSpins

# System parameters
const a = 0.18
const γ = 1.
const e_dipole = [0,0,1.]
const T = [0:0.05:5;]
const N = 5
const Ncenter = 3

const system = SpinCollection(cs.geometry.chain(a, N), e_dipole; gamma=γ)


# Define Spin 1/2 operators
spinbasis = SpinBasis(1//2)
sigmax = spin.sigmax(spinbasis)
sigmay = spin.sigmay(spinbasis)
sigmaz = spin.sigmaz(spinbasis)
sigmap = spin.sigmap(spinbasis)
sigmam = spin.sigmam(spinbasis)
I_spin = identityoperator(spinbasis)

# Initial state (Bloch state)
const phi = 0.
const theta = pi/2.

# Time evolution

# Independent
state0 = cs.independent.blochstate(phi, theta, N)
tout, state_ind_t = cs.independent.timeevolution(T, system, state0)

# Meanfield
state0 = cs.meanfield.blochstate(phi, theta, N)
tout, state_mf_t = cs.meanfield.timeevolution(T, system, state0)

# Meanfield + Correlations
state0 = cs.mpc.blochstate(phi, theta, N)
tout, state_mpc_t = cs.mpc.timeevolution(T, system, state0)
```

```
# Quantum: master equation
sx_master = Float64[]
sy_master = Float64[]
sz_master = Float64[]

td_ind = Float64[]
td_mf  = Float64[]
td_mpc = Float64[]

embed(op::Operator) = QuantumOptics.embed(cs.quantum.basis(system), Ncenter, op)

function fout(t, rho::Operator)
    i = findfirst(T, t)
    rho_ind = cs.independent.densityoperator(state_ind_t[i])
    rho_mf  = cs.meanfield.densityoperator(state_mf_t[i])
    rho_mpc = cs.mpc.densityoperator(state_mpc_t[i])
    push!(td_ind, tracedistance(rho, rho_ind))
    push!(td_mf,  tracedistance(rho, rho_mf))
    push!(td_mpc, tracedistance(rho, rho_mpc))
    push!(sx_master, real(expect(embed(sigmax), rho)))
    push!(sy_master, real(expect(embed(sigmay), rho)))
    push!(sz_master, real(expect(embed(sigmaz), rho)))
end

Ψ$_0$ = cs.quantum.blochstate(phi,theta,N)
ρ$_0$ = Ψ$_0$⊗dagger(Ψ$_0$)
cs.quantum.timeevolution(T, system, ρ$_0$, fout=fout)

# Expectation values
mapexpect(op, states) = map(s->(op(s)[Ncenter]), states)

sx_ind = mapexpect(cs.independent.sx, state_ind_t)
sy_ind = mapexpect(cs.independent.sy, state_ind_t)
sz_ind = mapexpect(cs.independent.sz, state_ind_t)

sx_mf = mapexpect(cs.meanfield.sx, state_mf_t)
sy_mf = mapexpect(cs.meanfield.sy, state_mf_t)
sz_mf = mapexpect(cs.meanfield.sz, state_mf_t)

sx_mpc = mapexpect(cs.mpc.sx, state_mpc_t)
sy_mpc = mapexpect(cs.mpc.sy, state_mpc_t)
sz_mpc = mapexpect(cs.mpc.sz, state_mpc_t)
```

7.1 Quantum

The time evolution of the N spins in a rotating frame corresponding to $\sum_i \omega_0 \sigma_i^z$ is then governed by a master equation

$$\dot{\rho} = -\frac{i}{\hbar}[H, \rho] + \mathcal{L}[\rho]$$

with the Hamiltonian

$$H = \sum_{ij;i\neq j} \hbar\Omega_{ij}\sigma_i^+\sigma_j^-$$

and Lindblad-term

$$\mathcal{L}[\rho] = \frac{1}{2}\sum_{i,j}\Gamma_{ij}(2\sigma_i^-\rho\sigma_j^+ - \sigma_i^+\sigma_j^-\rho - \rho\sigma_i^+\sigma_j^-).$$

The dipole-dipole interaction $\Omega_{ij} = \frac{3}{4}\gamma G(k_0 r_{ij})$ and the collective decay $\Gamma_{ij} = \frac{3}{2}\gamma F(k_0 r_{ij})$ can be obtained analytically with

$$\begin{aligned}
F(\xi) &= \alpha\frac{\sin\xi}{\xi} + \beta\left(\frac{\cos\xi}{\xi^2} - \frac{\sin\xi}{\xi^3}\right)\\
G(\xi) &= -\alpha\frac{\cos\xi}{\xi} + \beta\left(\frac{\sin\xi}{\xi^2} + \frac{\cos\xi}{\xi^3}\right)
\end{aligned}$$

with $\alpha = 1 - \cos^2\theta$ and $\beta = 1 - 3\cos^2\theta$, where θ represents the angle between the line connecting atoms i and j and the common atomic dipole orientation.

7.2 0th order: Independent spins

Each spin evolves independently according to

$$\begin{aligned}
\langle\dot{\sigma_k^x}\rangle &= -\frac{1}{2}\gamma\langle\sigma_k^x\rangle\\
\langle\dot{\sigma_k^y}\rangle &= -\frac{1}{2}\gamma\langle\sigma_k^y\rangle\\
\langle\dot{\sigma_k^z}\rangle &= \gamma\big(1 - \langle\sigma_k^z\rangle\big)\\
&.
\end{aligned}$$

7.3 1st order: Meanfield

$$\begin{aligned}
\langle\dot{\sigma_k^x}\rangle &= \sum_{i;i\neq k}\Omega_{ki}\langle\sigma_i^y\sigma_k^z\rangle - \frac{1}{2}\gamma\langle\sigma_k^x\rangle - \frac{1}{2}\sum_{i;i\neq k}\Gamma_{ki}\langle\sigma_i^x\sigma_k^z\rangle\\
\langle\dot{\sigma_k^y}\rangle &= -\sum_{i;i\neq k}\Omega_{ki}\langle\sigma_i^x\sigma_k^z\rangle - \frac{1}{2}\gamma\langle\sigma_k^y\rangle - \frac{1}{2}\sum_{i;i\neq k}\Gamma_{ki}\langle\sigma_i^y\sigma_k^z\rangle\\
\langle\dot{\sigma_k^z}\rangle &= -i\sum_{i;i\neq k}\Omega_{ki}\Big(\langle\sigma_k^x\sigma_i^y\rangle - \langle\sigma_i^x\sigma_k^y\rangle\Big) + \gamma\big(1 - \langle\sigma_k^z\rangle\big)\\
&\quad + \frac{1}{2}\sum_{i;i\neq k}\Gamma_{ki}\Big(\langle\sigma_k^x\sigma_i^x\rangle + \langle\sigma_i^y\sigma_k^y\rangle\Big)
\end{aligned}$$

7.4 2nd order: Meanfield plus Correlations (MPC)

$$
\begin{aligned}
\dot{\langle\sigma_k^x\sigma_l^x\rangle} = &\sum_{j;j\neq k,l}\Omega_{kj}\langle\sigma_k^z\sigma_l^x\sigma_j^y\rangle + \sum_{j;j\neq k,l}\Omega_{lj}\langle\sigma_k^x\sigma_l^z\sigma_j^y\rangle \\
&- \gamma\langle\sigma_k^x\sigma_l^x\rangle + \Gamma_{kl}\Big(\langle\sigma_k^z\sigma_l^z\rangle - \frac{1}{2}\langle\sigma_k^z\rangle - \frac{1}{2}\langle\sigma_l^z\rangle\Big) \\
&- \frac{1}{2}\sum_{j;j\neq k,l}\Gamma_{kj}\langle\sigma_k^z\sigma_l^x\sigma_j^x\rangle - \frac{1}{2}\sum_{j;j\neq k,l}\Gamma_{lj}\langle\sigma_k^x\sigma_l^z\sigma_j^x\rangle \\
\dot{\langle\sigma_k^y\sigma_l^y\rangle} = &-\sum_{j;j\neq k,l}\Omega_{kj}\langle\sigma_k^z\sigma_l^y\sigma_j^x\rangle - \sum_{j;j\neq k,l}\Omega_{lj}\langle\sigma_k^y\sigma_l^z\sigma_j^x\rangle \\
&- \gamma\langle\sigma_k^y\sigma_l^y\rangle + \Gamma_{kl}\Big(\langle\sigma_k^z\sigma_l^z\rangle - \frac{1}{2}\langle\sigma_k^z\rangle - \frac{1}{2}\langle\sigma_l^z\rangle\Big) \\
&- \frac{1}{2}\sum_{j;j\neq k,l}\Gamma_{kj}\langle\sigma_k^z\sigma_l^y\sigma_j^y\rangle - \frac{1}{2}\sum_{j;j\neq k,l}\Gamma_{lj}\langle\sigma_k^y\sigma_l^z\sigma_j^y\rangle \\
\dot{\langle\sigma_k^z\sigma_l^z\rangle} = &\sum_{j;j\neq k,l}\Omega_{kj}\Big(\langle\sigma_k^y\sigma_l^z\sigma_j^x\rangle - \langle\sigma_k^x\sigma_l^z\sigma_j^y\rangle\Big) \\
&+ \sum_{j;j\neq k,l}\Omega_{lj}\Big(\langle\sigma_k^z\sigma_l^y\sigma_j^x\rangle - \langle\sigma_k^z\sigma_l^x\sigma_j^y\rangle\Big) \\
&- 2\gamma\langle\sigma_k^z\sigma_l^z\rangle + \gamma\big(\langle\sigma_l^z\rangle + \langle\sigma_k^z\rangle\big) \\
&+ \Gamma_{kl}\Big(\langle\sigma_k^y\sigma_l^y\rangle + \langle\sigma_k^x\sigma_l^x\rangle\Big) \\
&+ \frac{1}{2}\sum_{j;j\neq k,l}\Gamma_{kj}\Big(\langle\sigma_k^x\sigma_l^z\sigma_j^x\rangle + \langle\sigma_k^y\sigma_l^z\sigma_j^y\rangle\Big) \\
&+ \frac{1}{2}\sum_{j;j\neq k,l}\Gamma_{lj}\Big(\langle\sigma_k^z\sigma_l^x\sigma_j^x\rangle + \langle\sigma_k^z\sigma_l^y\sigma_j^y\rangle\Big) \\
\dot{\langle\sigma_k^x\sigma_l^y\rangle} = &\,\Omega_{kl}\Big(\langle\sigma_k^z\rangle - \langle\sigma_l^z\rangle\Big) + \sum_{j;j\neq k,l}\Omega_{kj}\langle\sigma_k^z\sigma_l^y\sigma_j^y\rangle \\
&- \sum_{j;j\neq k,l}\Omega_{lj}\langle\sigma_k^x\sigma_l^z\sigma_j^x\rangle - \gamma\langle\sigma_k^x\sigma_l^y\rangle \\
&- \frac{1}{2}\sum_{j;j\neq k,l}\Gamma_{kj}\langle\sigma_k^z\sigma_l^y\sigma_j^x\rangle - \frac{1}{2}\sum_{j;j\neq k,l}\Gamma_{lj}\langle\sigma_k^x\sigma_l^z\sigma_j^y\rangle \\
\dot{\langle\sigma_k^x\sigma_l^z\rangle} = &\,\Omega_{kl}\langle\sigma_l^y\rangle + \sum_{j;j\neq k,l}\Omega_{kj}\langle\sigma_k^z\sigma_l^z\sigma_j^y\rangle \\
&+ \sum_{j;j\neq k,l}\Omega_{lj}\Big(\langle\sigma_k^x\sigma_l^y\sigma_j^x\rangle - \langle\sigma_k^x\sigma_l^x\sigma_j^y\rangle\Big) \\
&- \frac{3}{2}\gamma\langle\sigma_k^x\sigma_l^z\rangle + \gamma\langle\sigma_k^x\rangle - \Gamma_{kl}\Big(\langle\sigma_k^z\sigma_l^x\rangle - \frac{1}{2}\langle\sigma_l^x\rangle\Big) \\
&- \frac{1}{2}\sum_{j;j\neq k,l}\Gamma_{kj}\langle\sigma_k^z\sigma_l^z\sigma_j^x\rangle \\
&+ \frac{1}{2}\sum_{j;j\neq k,l}\Gamma_{lj}\Big(\langle\sigma_k^x\sigma_l^x\sigma_j^x\rangle + \langle\sigma_k^x\sigma_l^y\sigma_j^y\rangle\Big)
\end{aligned}
$$

$$
\begin{aligned}
\langle \dot{\sigma_k^y \sigma_l^z} \rangle = &-\Omega_{kl} \langle \sigma_l^x \rangle - \sum_{j;j\neq k,l} \Omega_{kj} \langle \sigma_k^z \sigma_l^z \sigma_j^x \rangle \\
&+ \sum_{j;j\neq k,l} \Omega_{lj} \Big(\langle \sigma_k^y \sigma_l^y \sigma_j^x \rangle - \langle \sigma_k^y \sigma_l^x \sigma_j^y \rangle \Big) \\
&- \frac{3}{2} \gamma \langle \sigma_k^y \sigma_l^z \rangle + \gamma \langle \sigma_k^y \rangle - \Gamma_{kl} \Big(\langle \sigma_k^z \sigma_l^y \rangle - \frac{1}{2} \langle \sigma_l^y \rangle \Big) \\
&- \frac{1}{2} \sum_{j;j\neq k,l} \Gamma_{kj} \langle \sigma_k^z \sigma_l^z \sigma_j^y \rangle \\
&+ \frac{1}{2} \sum_{j;j\neq k,l} \Gamma_{lj} \Big(\langle \sigma_k^y \sigma_l^x \sigma_j^x \rangle + \langle \sigma_k^y \sigma_l^y \sigma_j^y \rangle \Big)
\end{aligned}
$$